Potential of Ionic Liquids as Protein Drug Delivery Systems
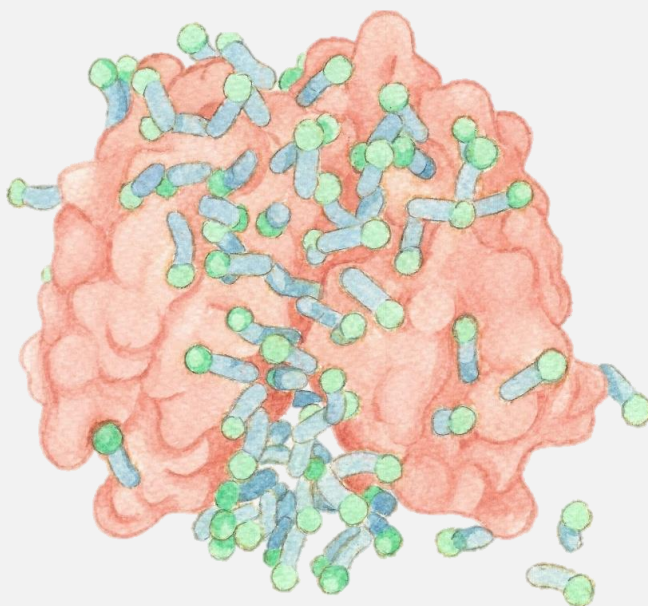
Márcia Maria da Silva Alves

Dissertation presented to obtain the **Ph.D degree in**

Molecular Biosciences

Oeiras, July, 2022

Oeiras, July, 2022

Potential of Ionic Liquids as Protein Drug Delivery Systems

Márcia M. S. Alves

ITQB nova

Potential of Ionic Liquids as Protein Drug Delivery Systems

Márcia Maria da Silva Alves

Dissertation presented to obtain the Ph.D degree in Molecular Biosciences

Instituto de Tecnologia Química e Biológica António Xavier | Universidade Nova de Lisboa

Oeiras, July, 2022

Supervisors:

Dr Margarida Archer, Principal Researcher and Head of the Membrane Protein Crystallography Laboratory of ITQB-NOVA (supervisor)

Dr Ana B Pereiro, Principal Researcher at the Bio(chemical) Process Engineering Group of LAQV-Requimte, NOVA School of Science and Technology (co-supervisor)

Work performed at:

Membrane Protein Crystallography Laboratory

Instituto de Tecnologia Química e Biológica António Xavier

Av. da República (EAN) 2780-157 Oeiras – Portugal

Tel: +351-214469548

Fax: +351-214469549

Acknowledgements

Obtaining a PhD is not an easy process and would have been nearly impossible to accomplish without a support network. This success is not just my own, and I would like to thank everyone who played a part, either directly or indirectly.

To my supervisors, Dr Margarida Archer and Dr Ana B. Pereiro, I thank for always guiding me while giving me the freedom to make this project my own, and never doubting my abilities. Your supervision has turned me into a more confident and independent scientist (and person), and for that, I will always be grateful.

To all the collaborators and co-authors, thank you for your patience, for the training and the discussions. This project is undoubtedly richer because of you: Dr Ivo Martins, Dr João Araújo, Dr João Vicente, Dr Haydyn Mertens, Prof Paula Leandro and Dr Manuel Melo.

To my colleagues at the Membrane Protein Crystallography Lab, thank you for the comradery over all these years, for being there through the good and not-so-good times, and for listening to my rants.

Thank you to my friends who have always been there for me. I can't believe how much we've all grown and can't wait to see the next stages in our lives.

The biggest thanks go to my family, without whom I would not be here today, and especially to my mum, who always pushes me to do my best and always makes sure I have everything I need to do so.

Pedro, thank you for being my biggest supporter, my person, and my home. Words can't describe how grateful I am for everything you do for me and our little family – we are the luckiest to have you. And finally, to my babies. Francisco – you are the sweetest boy I could have hoped for, and every day is brighter because of you. Little One – you made the last few months of my PhD more interesting. We can't wait to welcome you home.

Summary

Although therapeutic proteins hold the promise to revolutionize the pharmaceutical industry due to their high specificity and potency, associated with fewer side effects and reduced intrinsic toxicity, their development faces several hurdles. Proteins are intrinsically unstable and highly sensitive to changes in the environment, which lead to short circulation half-lives and hampered the development of stable formulations. To bypass these issues, Drug Delivery Systems (DDS) are being developed to stabilize and deliver these biologics to the human body at therapeutic levels, with improved safety and efficacy.

After being researched for a broad spectrum of applications over the last couple of decades, ionic liquids (ILs) have been garnering attention in the drug delivery field, due to their unique physicochemical characteristics. Ionic liquids are salts comprising organic cations and organic or inorganic anions, which are liquid at temperatures close to or lower than 373.15 K. These solvents present several desirable physicochemical properties and are highly tuneable.

Surface-active ionic liquids (SAILs) present an amphiphilic character that allows them to behave as surfactants and self-assemble into aggregates such as micelles in aqueous solutions. The fine-tuning of SAILs allows the manipulation of the structure and dynamics of micellar aggregates, which can, in turn, impact their ability to enhance the solubility and permeability of drugs across biological membranes. Within the SAILs family, fluorinated ionic liquids (FILs) are defined as ionic liquids with fluorinated alkyl chain lengths equal to or greater than four carbon atoms, which are capable of forming distinct aggregated structures.

The amphiphilicity of SAILs allows for unique properties when formulated with hydrophilic molecules like soluble proteins, leading to their encapsulation into the micelle's core. Furthermore, using micelles as drug carriers is advantageous due to their small size and narrow size distribution, and increased drug bioavailability and stability. However, the structural diversity of both ILs and proteins means that a wide range of solvent-protein interactions is possible. This thesis aimed to study the interaction of FILs with model and therapeutic proteins to assess their potential as drug delivery systems.

Initially, as described in Chapter II, a battery of six FILs were tested against model protein lysozyme (Lys). Through a series of biophysical assays, we concluded that despite protein encapsulation by the surfactant FILs, neither the stability nor activity of Lys were significantly affected. We were also able to select the most promising FILs family, taking into account their effect on the protein.

Chapter III details a similar experimental design applied to study the interaction between FILs and bovine serum albumin (BSA), a larger and more complex model protein. Although we were unable to perform the exact same assays to both proteins, the approach used in this section demonstrated that BSA was stabilized upon encapsulation by FILs.

In order to better understand the interaction between these model proteins and FILs, techniques such as small angle X-ray scattering (SAXS), coarse-grained molecular dynamics (CG-MD) and fluorescence microscopy were applied, as described in Chapter IV. These techniques showed that the proteins maintained their globular structure, and that Lys was encapsulated by the FIL, and the size of FIL-protein micelle depends on the protein and the interactions on its surface.

In Chapter V, similar methodologies were applied to human phenylalanine hydroxylase (hPAH), a potential therapeutic enzyme. hPAH is a highly complex and environmentally sensitive protein and needs to be stabilized to ensure its successful delivery. Although at first glance the addition of FIL revealed a detrimental effect on protein thermostability, this destabilization seemed to lead to an increase in hPAH activity rate. The work presented in this chapter demonstrates that the FIL is still able to encapsulate a larger and more complex protein such as hPAH, while retaining its structure and function.

The work described in this PhD thesis has made significant contributions to the understanding of interactions between different proteins and FILs. The methodologies and knowledge can now be applied not only to study similar systems, but also to hopefully develop novel drug delivery systems for the topical or transdermal delivery of therapeutic proteins.

Resumo

Apesar da revolução prometida pelas proteínas terapêuticas na indústria farmacêutica devido à sua elevada especificidade e potência associadas a menores efeitos secundários e toxicidade intrínseca, o seu desenvolvimento ainda enfrenta vários obstáculos. As proteínas são inerentemente instáveis e sensíveis a alterações no seu ambiente, o que leva a um curto tempo de semi-vida na circulação e dificulta o desenvolvimento de formulações estáveis. Para ultrapassar estes problemas, têm vindo a a ser desenvolvidos sistemas de administração de fármacos para estabilizar e administrar biofármacos ao corpo humano a níveis terapêuticos, com melhores níveis de segurança e eficácias.

Ao longo das últimas décadas, os líquidos iónicos (LI) têm vindo a ser investigados numa ampla gama de aplicações, mas só recentemente começaram a ganhar atenção como emulsões no campo da administração de fármacos, devido às suas características físico-químicas. Os LI são sais compostos por catiões orgânicos e aniões orgânicos ou inorgânicos, que se encontram no estado líquido a temperaturas abaixo dos 100 ºC. Estes solventes apresentam várias propriedades físico-químicas desejáveis e são facilmente customizáveis. Os líquidos iónicos tensioactivos (LIT) contém substituintes longos na cadeia alquílica e apresentam um caráter anfipático que lhes confere propriedades surfactantes, como a associação em micelas em soluções aquosas. A customização dos LIT permite a manipulação da estrutura e dinâmica dos agregados micelares, que, por sua vez, impactam a sua capacidade para aumentar a solubilidade e permeabilidade de fármacos através de membranas biológicas. Dentro da família dos LIT, líquidos iónicos fluorados (LIF) são definidos como líquidos iónicos com cadeias alquílicas fluoradas com comprimentos iguais ou superiores a quatro átomos de carbono, e que são capazes de formar agregados distintos.

O caráter anfipático dos LIT confere-lhes propriedades únicas quando formulados com moléculas hidrofílicas como proteínas, permitindo o seu encapsulamento no núcleo da micela. Além do mais, a utilização de micelas como transportadores de fármacos é vantajosa devido ao seu reduzido tamanho e estreita distribuição do mesmo, e permite melhorar a biodisponibilidade e estabilidade dos fármacos. No entanto, a diversidade estrutural quer dos LI quer das proteínas implica vastas interações solvente-proteína.

Assim, o objetivo desta tese é estudar a interação entre LIF e proteínas para avaliar o seu potencial como sistemas de administração de fármacos.

Inicialmente, como descrito no Capítulo II, um conjunto de seis LIF foram testados com lisozima (Lis), uma proteína modelo. Através de ensaios biofísicos, concluímos que apesar de a proteína estar encapsulada por um LIF surfactante, nem a estabilidade nem a atividade foram significativamente afetadas. Conseguimos também selecionar a família mais promissora de LIF, tendo em conta os seus efeitos na proteína.

O Capítulo III detalha um desenho experimental semelhante aplicado ao estudo da interação entre o LIF e a albumina de soro bovino (ASB), uma proteína modelo de maior dimensão e complexidade. Apesar de não ter sido possível aplicar os mesmos ensaios a ambas as proteínas, a abordagem utilizada nesta secção demonstrou que a ASB é estabilizada e encapsulada pelo LIF.

De modo a compreender melhor a interação entre estas proteínas modelo e os LIF, foram utilizadas técnicas como dispersão de raios-X a pequenos ângulos, dinâmica molecular e microscopia de fluorescência, conforme descrito no Capítulo IV. Estas técnicas permitiram-nos investigar a interação entre as proteínas modelo (Lis e ASB) e os LIF, mostrando que as suas estruturas globulares são mantidas, e que a Lis é encapsulada pelo LIF, onde o tamanho da micela LIF-proteína é limitado pela proteína e pelas interações na sua superfície.

No Capítulo V, metodologias semelhantes foram aplicadas ao estudo da fenilalanina hidroxilase humana (FAH), uma potencial enzima terapêutica, cuja estrutura é complexa e muito sensível ao ambiente, e que necessita de ser estabilizada para garantir uma administração bem-sucedida. Os dados mostram que a adição de LIF tem um efeito negativo na termoestabilidade da proteína, enquanto aumenta a taxa de atividade enzimática da FAH. O trabalho apresentado neste capítulo demonstra que o LIF é capaz de encapsular proteínas maiores e mais complexas como a FAH, mantendo a sua estrutura e função.

O trabalho descrito nesta Tese de Doutoramento contribuiu significativamente para uma melhor compreensão das interações entre diferentes proteínas e LIF. As metodologias e protocolos aqui descritos e o conhecimento podem de futuro ser aplicados não só no estudo de sistemas semelhantes, mas também para desenvolver novos sistemas de administração tópica ou transdérmica de proteínas terapêuticas.

List of Publications

<u>Alves, M.M.S.</u>; Leandro, P.; Mertens, H.D.T.; Pereiro, A.B.; Archer, M. Impact of Fluorinated Ionic Liquids on Human Phenylalanine Hydroxylase — A Potential Drug Delivery System. *Nanomaterials.* **2022**, *12*, 893. doi:10.3390/ nano12060893.

<u>Alves, M.M.S.</u>; Araújo, J.M.M.; Martins, I.C.; Pereiro, A.B.; Archer, M. Insights into the interaction of Bovine Serum Albumin with Surface-Active Ionic Liquids in aqueous solution. *J. Mol. Liq.* **2021**, *322*, 114537, doi:10.1016/j.molliq.2020.114537.

<u>Alves, M.</u>; Vieira, N.S.M.; Rebelo, L.P.N.; Araújo, J.M.M.; Pereiro, A.B.; Archer, M. Fluorinated ionic liquids for protein drug delivery systems: Investigating their impact on the structure and function of lysozyme. *Int. J. Pharm.* **2017**, *526*, 309–320, doi:10.1016/j.ijpharm.2017.05.002.

In preparation:

<u>*Alves, M.M.S.*</u>*; Melo, M.N.; Mertens, H.D.T.; Pereiro, A.B.; Archer, M. Studies on the interaction between model proteins and Fluorinated Ionic Liquids.*

Abbreviations

API	active pharmaceutical ingredient
BH$_4$	tetrahydrobiopterin
BN-PAGE	blue native-polyacrylamide gel electrophoresis
BSA	bovine serum albumin
CAC	critical aggregation concentration
CAGE	choline geranate
CD	circular dichroism
CG	coarse grained
CMC	critical micellar concentration
Cp	heat capacity
DDS	drug delivery system
DES	deep eutectic solvent
DLS	dynamic light scattering
***D*$_{max}$**	maximum particle dimensions
DMSO	dimethyl sulfoxide
DNA	deoxyribonucleic acid
DSC	differential scanning calorimetry
DSF	differential scanning fluorimetry
EC$_{50}$	cytotoxic effective concentration
FC	fluorocarbon compound
FDA	US Food and Drug Administration
FIL	fluorinated ionic liquid
Fluo	NHS-Fluorescein
hPAH	human phenylalanine hydroxylase
HPLC	high performance liquid chromatography
Humulin	human insulin
IC$_{50}$	half-maximum inhibitory constant
IL	ionic liquid
ITC	isothermal titration calorimetry
K$_D$	binding or affinity constant

L-Phe	phenylalanine
L-Tyr	tyrosine
Lys	lysozyme
MD	molecular dynamics
ME	microemulsion
MIC	minimal inhibitory concentration
MM	molecular mass
NHS	N-hydroxysuccinimide
NMR	nuclear magnetic resonance
NR	Nile Red
OD_{600}	optical density at 600 nm
OVA	ovalbumin
PCR	polymerase chain reaction
PEG-PAL	phenylalanine ammonia-lyase
PKU	phenylketonuria
PI	propidium iodide
R_g	radius of gyration
Rho	NHS-Rhodamine
RHE	reconstructed human epidermis
RNA	ribonucleic acid
SAIL	surface-active ionic liquid
SAXS	small-angle X-ray scattering
SC	stratum corneum
SD	standard deviation
SDS-PAGE	sodium dodecyl sulfate-polyacrylamide gel electrophoresis
SEC	size exclusion chromatography
SEM	scanning electron microscopy
T	temperature
TEM	transmission electron microscopy
T_m	melting temperature
TTAB	tetradecyltrimethylammonium bromide
$-T\Delta S^0_{agg}$	standard entropy of aggregation
v/v	volume per volume
V_P	Porod volume

α	degree of ionization
β	degree of counterion binding
ΔG^0_{agg}	Gibbs free energy of aggregation
ΔH^0_{agg}	enthalpy of aggregation
λ	wavelength

Ionic Liquid Nomenclature

Chemical Formula	Designation
$[N_{1112(OH)}][Asp]$	Cholinium aspartate
$[N_{1112(OH)}][C_4F_9CO_2]$	Cholinium perfluorobutanepentanoate
$[N_{1112(OH)}][C_4F_9SO_3]$	Cholinium perfluorobutanesulfonate
$[N_{1112(OH)}][Cl]$	Cholinium chloride
$[N_{1112(OH)}][CF_3SO_3]$	Cholinium trifluoromethanesulfonate
$[N_{1112(OH)}][Glu]$	Cholinium glutamate
$[N_{1112(OH)}][H_2PO_4]$	Cholinium dihydrogenphosphate
$[C_2C_1Im][C_4F_9CO_2]$	1-ethyl-3-methylimidazolium perfluorobutanepentanoate
$[C_2C_1Im][C_4F_9SO_3]$	1-ethyl-3-methylimidazolium perfluorobutanesulfonate
$[C_2C_1py][C_4F_9CO_2]$	1-ethyl-3-methylpyridinium perfluorobutanepentanoate
$[C_2C_1py][C_4F_9SO_3]$	1-ethyl-3-methylpyridinium perfluorobutanesulfonate
$[C_4C_1Im][Br]$	1-butyl-3-methylimidazolium bromide
$[C_4C_1Im][C_8OSO_3]$	1-butyl-3-methylimidazolium octylsulfate
$[C_4C_1Im][Cl]$	1-butyl-3-methylimidazolium chloride
$[C_4C_1Im][I]$	1-butyl-3-methylimidazolium iodide
$[C_4C_1Im][NO_3]$	1-butyl-3-methylimidazolium nitrate
$[C_4C_1Im][PF_6]$	1-butyl-3-methylimidazolium hexafluorophosphate
$[C_4C_1Im][SCN]$	1-butyl-3-methylimidazolium thiocyanate
$[C_4C_4Im][Cl]$	1,3-butylimidazolium chloride
$[C_6C_1Im][Cl]$	1-hexyl-3-methylimidazolium chloride
$[C_8C_1Im][Cl]$	1-octyl-3-methylimidazolium chloride
$[C_{12}C_1Im][Br]$	1-dodecyl-3-methylimidazolium bromide
$[C_{12}C_1Im][Cl]$	1-dodecyl-3-methylimidazolium chloride
$[C_{12}C_1Im][NTf_2]$	1-dodecyl-3-methylimidazolium bis(trifluoromethanesulfonyl)imide
$[C_{14}C_1Im][Br]$	1-tetradecyl-3-methylimidazolium bromide
$[C_{14}C_1Im][Cl]$	1-tetradecyl-3-methylimidazolium chloride
$[C_{16}C_1Im][Br]$	1-hexadecyl-3-methylimidazolium bromide
$[C_{16}C_1Im][Cl]$	1-hexadecyl-3-methylimidazolium chloride

Table of Contents

List of Figures

List of Tables

CHAPTER I

General Introduction

1. Therapeutic Proteins and Drug Delivery Systems

The growing understanding of the molecular mechanisms behind diseases has resulted in the identification of key proteins responsible for their severity or progression, which may be related to protein mutations or other abnormalities, or their presence in exceedingly high or low concentrations [1]. This knowledge presents an opportunity to harness the therapeutic potential of these proteins to alleviate disease. The advantages of using protein therapeutics are related to their high specificity with less potential for interference with other physiological processes and side effects, high potency, and reduced intrinsic toxicity [1,2]. Furthermore, they can provide effective replacement therapy for diseases in which a gene is mutated or deleted.

Proteins as biotherapeutics are one of the biggest successes in the field of modern health science, which started 100 years ago with the development of insulin. Insulin was first purified in 1922, from bovine and porcine pancreases, and revolutionized the lives of patients with diabetes mellitus type I, becoming the first therapeutic protein used in a clinical setting [1,3]. However, its widespread use was hindered by issues such as the availability of animal pancreases, production cost and immunological reaction from patients to an animal protein [1]. It wasn't until the 1970s that these problems were overcome by using DNA technology to express the first recombinant protein therapeutic, Humulin (human insulin) [4]. This breakthrough meant that insulin was now available in great quantities, at lower cost and free from animal pancreatic substances [1].

Protein pharmaceuticals are described as one of the fastest growing class of molecules, with more than 250 proteins already being used clinically and global sales exceeding US $125 billion per year [5,6]. In the period from 2016 to 2021, a total of 278 new drugs were approved by the US Food and Drug Administration (FDA), of which 87 were protein therapeutics, including enzymes, peptides and monoclonal antibodies [7]. The profile of products in clinical trials suggests that most biopharmaceuticals approved in the foreseeable future will also be predominantly protein-based [8].

Therapeutic proteins can be classified into four categories, according to their mechanism of action (Figure 1.1). These categories are: Group I) enzymatic or regulatory activity, where the therapeutic replaces a protein that is either absent or defective; Group II) targeting activity, either by interfering with a specific pathway of delivering other compounds; Group III) vaccines, and Group IV) diagnostics [1]. Examples of therapeutic proteins

currently used in the clinic include enzymes and hormones for the treatment of genetic and/or metabolic disorders, monoclonal antibodies as chemotherapeutics and clotting factors [1,3].

Group I: Enzymes and Regulatory Proteins	Group II: Targeted Proteins
- Replace deficient or abnormal protein - Increase of existing pathway - Provide novel function or ability *Examples: insulin, clotting factors, human follicle-stimulating enzyme, botulinum toxin*	- Interfere with molecule or organism - Deliver other compounds or proteins *Examples: monoclonal antibodies for immunoregulation or chemotherapy*
Group III: Protein Vaccines	**Group IV: Protein Diagnostics**
- Protect against deleterious foreign agents - Treat autoimmune diseases *Examples: human papiloma virus vaccine, anti-rhesus immunoglobulin G*	- Used for *in vivo* and *in vitro* diagnostics *Examples: imaging agents, antigens for* in vitro *diagnostics*

Figure 1.1. Functional classification of therapeutic proteins. Adapted from Leader, 2008 [1].

However, despite the great promise that therapeutic proteins hold to revolutionize the pharmaceutical industry, their development faces several hurdles. In order for the protein to remain active, its three-dimensional conformation must be maintained throughout the processing and storage steps [9]. This can be challenging as proteins are conformationally unstable and highly sensitive to changes in environment, presenting short circulation half-lives and hampering the development of stable formulations [2,10,11]. The potential immunogenicity and limited permeability through biological membranes due to high molecular weight also hinder their use as biopharmaceuticals [2]. Furthermore, protein drugs cannot be administered orally due to poor absorption and degradation in the gastrointestinal environment, and are instead administered by frequent intravenous injections in high doses to maintain therapeutic effect, which not only increases the risk of side effects and toxicity, but are also poorly tolerated by the recipient [12]. To bypass these issues, strategies have been developed to stabilize and deliver these protein therapeutics, such as modification of

protein structure, conjugation with polymers or macromolecules, and drug delivery systems (DDS).

DDS are formulations that enable the introduction of a drug substance into the human body at therapeutic levels, with improved safety and efficacy [12,13]. The delivery of the therapeutic protein may be controlled, preventing its premature degradation, and targeting the pharmaceutic to the disease site and cells reduces side effects [14], while improving drug bioavailability, permeability, pharmacokinetics and biodistribution [15–17]. Thus, the therapeutic can be administered at an effective dose through a route that allows easier patient compliance, such as orally or topically, and the potential for immunological reactions is greatly diminished (Figure 1.2). Nanotechnology has played an important part in the design of different DDS for the encapsulation and delivery of different drugs, and some can already be found in the market [2,16].
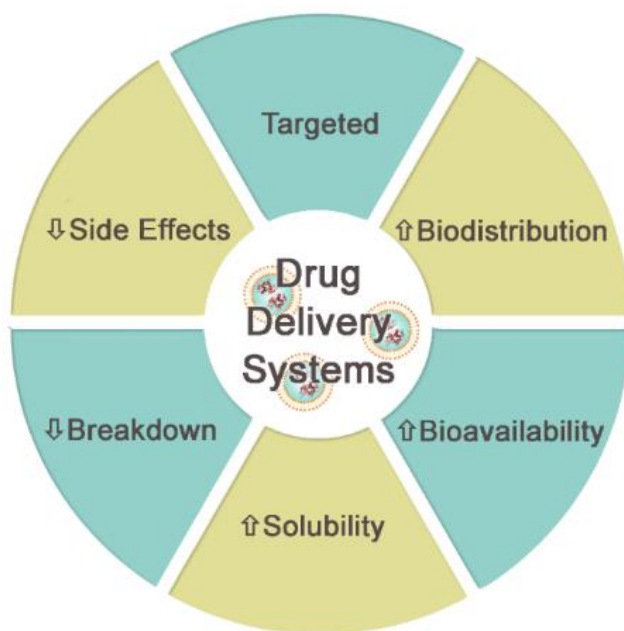
Figure 1.2. Advantages of drug delivery systems.

Liposomes (see Figure 1.3), which consist of phospholipid vesicles, were the first nanosized DDS to translate from bench to clinic. They can be used to deliver hydrophobic compounds inserted into the lipid membrane, or hydrophilic molecules entrapped in the aqueous core, in a wide range of molecular weights. Liposomes display ideal

biocompatibility and biodegradability, and their surface can be functionalized for targeted delivery. Possible routes of administration include not only the more traditional parenteral, but also oral, pulmonary, ocular, topical and nasal. Therapeutic proteins entrapped in liposomes may have increased stability since the lipid bilayer provides protection from degradation, but the liposome preparative process is associated with instability issues and low encapsulation efficiencies [2].

Another type of phospholipid vesicle are exosomes (Figure 1.3). Exosomes are neutral extracellular vesicles, with native membrane composition. They also present high and specific organotropism and immunocompatibility. However, their widespread use is hindered by the complex preparative and purification processes, and very low isolation yields [2].

Emulsions (see Figure 1.3), on the other hand, demonstrate high encapsulation efficiencies, increased drug solubility and stability, have cheap manufacturing processes, and can be easily scaled up. Emulsions are colloidal dispersions composed of oil, water and surfactants, that are small in size (nano or microemulsions), and have been employed for the delivery of proteins by non-parenteral routes [2]. Microemulsions (MEs), specifically, are defined not only by their small size (droplets below 100 nm), but more importantly by forming spontaneously without need for mechanical energy and being thermodynamically stable [18]. Since these systems are comprised of two immiscible liquids stabilized by surfactants, the choice of components is critical and stability is highly dependent on interfacial tension between the dispersed and continuous phases [19]. Instability between components can lead to the dissolution of the small droplets into larger droplets, with leakage of the incorporated drug and phase inversion. Although the development of the complex systems required for MEs may be time consuming, this DDS has been successfully applied for topical

Liposome   Exosome   Micro/nano emulsion
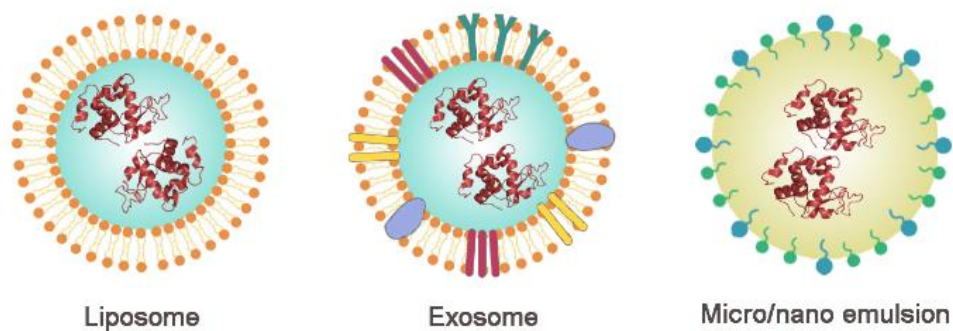
Figure 1.3. Examples of DDS for the delivery of therapeutic proteins.

and transdermal delivery of drugs, as well as protein and peptide delivery to the gastrointestinal tract [18–20].

After being researched for a broad spectrum of applications over the last couple of decades, ionic liquids (ILs) have been garnering attention as emulsions in the drug delivery field, due to their unique physicochemical characteristics.

2. Ionic Liquids

Ionic liquids are salts comprising organic cations and organic or inorganic anions, which are liquid at temperatures close to or lower than 373.15 K. The lower melting temperature is a consequence of the inability of ILs to pack into a well-defined crystalline structure, due to ion asymmetry, weak intermolecular forces and ion conformational degrees of freedom [21]. These greener solvents present several desirable physicochemical properties, namely low vapor pressure, nonflammability, high thermal and chemical stability, good solubility and high ionic conductivities [22–24]. The big selling point of ILs, however, lies in their highly tunable nature: by changing the cations and anions as well as substituents, it is possible to tailor properties like melting point, surface tension, toxicity and biodegradability, turning them into desirable task specific designer compounds [25,26]. For example, manipulating ion size and charge will impact conductivity, while poorer water miscibility can be achieved by incorporating long hydrocarbon chains or aromatic rings, and higher hydrophilicity can be tuned with carboxyl or alcohol groups and nitrogen atoms [21]. The easy synthesis (direct acid-base neutralization and metathesis) and tailoring of ILs makes them useful in various fields and applications, such as reaction media for organic and enzyme stabilization reactions, separations and extractions; electrolytes for electrochemistry; lubricants; nanotechnology; organic synthesis and catalysis [23,24].

Since their discovery in the first half of the 20th century, three generations of ILs have been described, which are characterized by chemical structure and properties (see Figure 1.4). First generation ILs were sensitive to air and water, and combined dialkylimidazolium ($[C_nC_nIm]^+$) and alkylpyridinium ($[C_npy]^+$) cations with metal halides. The second generation became air- and water-stable, and the most common cations included dialkylimidazolium, alkylpyridinium, ammonium and phosphonium, and anions were usually bis(trifluoromethylsulfonyl)imide ($[NTf_2]$), tetrafluoroborate ($[BF_4]^-$) or hexafluorophosphate ($[PF_6]^-$). Third generation ILs now employ biodegradable and natural ions, such as choline and amino acids, and ions with known biological activities [27].

Although ILs are considered "green solvents" and are evolving towards more biocompatible structures, in some cases there are still concerns on their environmental impact. Regarding ecological safety, chemical compounds should be easily degradable and decompose into harmless substances that do not accumulate in the environment [27]. This can occur through the biodegradation process, which is performed by bacterial or fungal

enzymes, and that leads to the destruction of their chemical structure and, consequently, loss of properties. As with most IL properties, the potential for biodegradation can also be tuned, as it is known that the presence of long unsubstituted alkyl chains, oxygen atoms and sites for enzymatic hydrolysis and aromatic rings promote biodegradability, and it can be hindered by the presence of branched alkyl chains, and halogen containing and fluoroorganic anions [27].
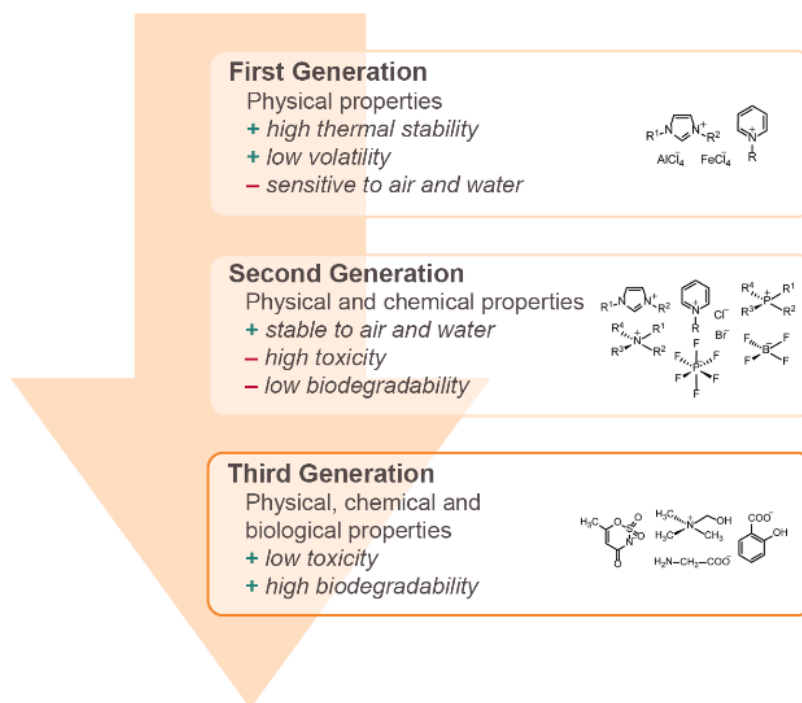
Figure 1.4. Evolution of IL generations, main properties and advantages and disadvantages. Adapted from Egorova *et al*, 2017 [27].

Toxicity is also determined by the molecular structure, including: (i) cation alkyl chain length; (ii) presence and nature of functional groups in the cation; (iii) nature of the cation and anion; and (iv) interactions between the cation and anion [22,27]. For instance, the relative toxicity of the cationic head groups follows the trend: cholinium < piperidinium < pyrrolidinium < pyridinium = imidazolium < ammonium < phosphonium [22].

The impact of IL toxicity has been investigated in model organisms, such as plants, fish, rodents, mollusca, worms and crustaceans. It has been reported that imidazolium-based ILs provoked developmental damage on mice and rats, and caused oxidative stress and growth inhibition in aquatic algae and terrestrial plants [27]. Interestingly, cholinium ILs,

which are considered to be relatively safe due to their natural origin, exhibited toxicity against *Daphnia magna* (crustacean) and *Lemna minor* (aquatic plant), demonstrating a potential environmental hazard [28]. This enlightens the issue that although the cation may be biocompatible, toxicity may still be driven by the anion. It is therefore imperative that researchers keep investigating the interaction between organisms and ILs, although high toxicities may also be interesting for some biomedical applications, as will be discussed further ahead.

3. Surface Active Ionic Liquids

ILs that contain long alkyl chain substituents present an amphiphilic character due to the charged hydrophilic head group and the non-polar hydrophobic tail (see Figure 1.5). This structure allows them to behave as surfactants, which can self-assemble into aggregates such as micelles in aqueous solutions. These ILs are categorized as surface active ionic liquids (SAILs) [26,29].

Figure 1.5. Amphiphilic structure of SAILs. Adapted from Buettner *et al*, 2022 [29].

Biocompatible SAILs are usually choline or amino acid based, presenting low toxicity and high biodegradability, and decrease interfacial tension between polar and nonpolar solvents in water, being considered environmentally friendly surfactants [26]. The fine tuning of SAILs allows for the manipulation of the structure and dynamics of micellar aggregates, which can in turn impact their ability to enhance the solubility and permeability of drugs across biological membranes [30]. One of the most important parameters to take into account, is the critical micellar concentration (*CMC*), which corresponds to the threshold concentration above which the SAIL starts assembling into larger aggregates (see Figure 1.6) [29].
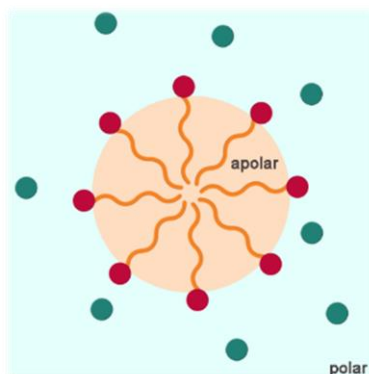
Figure 1.6. Micelle formed by amphiphilic SAILs. Adapted from Buettner *et al*, 2022.[29]

The improved surface-activity of SAILs, as well as their structural tunability and micellization properties, make them very versatile for different fields, and potential applications include pharmaceuticals, cosmetics, paints, detergents, and biochemical reactions [31]. SAILs have been used as substituents for conventional surfactants in chemical separation processes, being able to efficiently solubilize and extract environmental contaminants such as benzene, toluene and xylene [32], and to separate metal ions from wastewater streams, including gold(III), thorium(IV) and cadmium(II) [33–35]. SAILs can also be successfully employed as mobile or stationary phase modifiers in high performance liquid chromatography (HPLC) [36]. Organic synthesis and catalysis can be greatly improved by the use of surface-active additives, as they have the ability to improve the solubility of organic compounds or to catalyze reactions through the micellar catalysis principle: substrates that are stabilized within micelles experience a higher local concentration that in bulk solution [29].

Amphiphilicity of biocompatible ILs allows for unique properties when formulated with hydrophilic molecules like soluble proteins, allowing for their encapsulation into the micelle's core. Furthermore, advantages of using micelles as drug carriers include their small size and narrow size distribution, and increased drug bioavailability and stability [37]. The use of SAILs can elicit longer protein shelf lives and overcome some of the formulation hurdles faced by the traditional aqueous buffered solutions [21], as will be explored further ahead.

4. Fluorinated Ionic Liquids

Within the SAILs family, there are the fluorinated ionic liquids (FILs), which were used throughout this work, that combine the best properties of fluorocarbon compounds (FCs) with those of ILs [38].

FCs are fluorosurfactants that have a polar head and a hydrophobic tail comprised of strong C-F bonds that induce high rigidity and low polarity. Their low surface tension allows for the formation of distinct self-assemblies (tubules, vesicles, ribbons, helices), and their high capacity for dissolving gases makes them desirable for *in vivo* oxygen delivery and drug delivery to the lungs [39]. FCs also display low intensity interactions with standard organic compounds and chemical and biological inertness. However, these compounds can have a negative impact on the environment, as they present a potential for high bioaccumulation and resistance to biodegradation. Therefore, the association of FCs with ILs shows great promise, since ILs are easier to recover and recycle, and their toxicity can be tuned [38,40].

FILs are defined as ionic liquids with fluorinated alkyl chain lengths equal to or greater than four carbon atoms, which are able to form three nanoseggregated domains (polar, non-polar and fluorinated) that enable self-assembly and high solubilization power [38,41]. Depending on the total concentration in aqueous solution, FILs are capable of forming distinct aggregated structures. The FILs used throughout this work are mostly comprised of two anions, perfluorobutanesulfonate ($[C_4F_9SO_3]^-$) and perfluoropentanoate ($[C_4F_9CO_2]^-$), conjugated with three cations: cholinium ($[N_{1112(OH)}]^+$), imidazolium ($[C_2C_1Im]^+$), and pyridinium ($[C_2C_1py]^+$) (see Figure 1.7), whose aggregation and toxicity properties have been previously characterized [40–42].

The aggregation behavior of $[C_4F_9SO_3]^-$-based FILs was first reported by Pereiro *et al.* [38] where the critical aggregation concentrations (*CAC*) were determined using complementary techniques. This study concluded that the fluorosurfactants are completely miscible in water and that, although all compounds had low *CAC*s in the same order of magnitude, $[N_{1112(OH)}]^+$ cation was associated to the highest *CAC* and consequently has the least surfactant power. The aggregation profile of $[C_2C_1Im][C_4F_9SO_3]$ revealed that above the *CAC*, the FIL ions assemble to form aggregates with the fluorinated alkyl chains oriented towards the aggregates' interior, and that three phase transitions occur, with a proposed mechanism of monomer – spherical micelles – globular micelles – cylindrical or lamellar

13
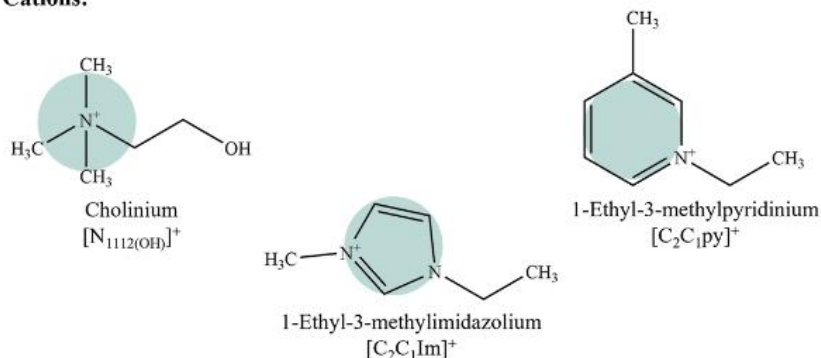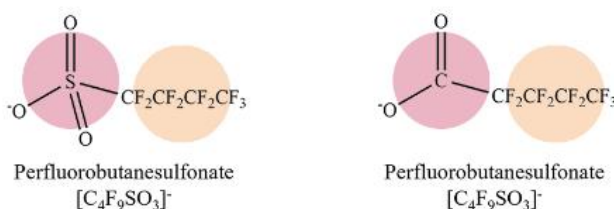
Figure 1.7. Chemical structure of FILs used in this work, comprising two anions, $[C_4F_9SO_3]^-$) and $[C_4F_9CO_2]^-$, conjugated with three cations: $[N_{1112(OH)}]^+$, $[C_2C_1Im]^+$ and $[C_2C_1py]^+$.

micelles, with increasing FIL concentrations. A different study reported that increasing the hydrogenated alkyl chain length of the imidazolium cation, as well as the fluorinated chain length, resulted in lower *CAC*s and, therefore, higher surfactant power [43].

The cytotoxicity of FILs based on the $[C_4F_9SO_3]^-$ anion was studied using four different human cell lines – Caco-2, HepG2, HaCaT and EA.hy926 – which correspond to intestinal, hepatic, skin and endothelial models, respectively [42]. Cell viability for Caco-2, HepG2 and EA.hy926 cell lines was not affected by FILs at concentrations up to 10 mM. $[N_{1112(OH)}]^+$ was found to induce the lowest cytotoxicity, since this cation is non-aromatic, symmetric, and choline is an essential nutrient. $[C_2C_1Im]^+$ and $[C_2C_1py]^+$ induced a clear dose-response relationship in HaCaT cells ($[N_{1112(OH)}]^+$ was not studied), but since the cytotoxic effective concentration (EC_{50}) was ~ 7 mM, the toxicities could be considered negligible, as the authors postulate that these concentrations would not be reached in biomedical applications. The effect of perfluorobutansulfonate- and pentanoate-based FILs on hemolysis was also evaluated through the release of hemoglobin in the plasma after red blood cell lysis [41]. Although significant cytotoxicity towards red blood cells was only achieved at FIL concentrations > 17 mM, $[N_{1112(OH)}]^+$ was found to have the highest hemolytic

14

activity, despite being the least cytotoxic cation. This behavior might be associated to the type of structures formed by these choline-based FILs above their *CAC*, that may cause cell membrane disruption [41].

Other studies evaluated the environmental impact of FILs based on $[C_4F_9SO_3]^-$ and $[C_4F_9CO_2]^-$ anions [40,41]. Acute aquatic toxicity was screened using different species – *Vibrio fischeri*, *Daphnia magna* and *Lemna minor* [40]. Although FILs could not be considered toxic under the tested conditions (long term effects were not evaluated), carboxylate anions were found to be less toxic than perfluorobutansulfonates, and among the cations choliniums were generally less toxic. Furthermore, imidazolium-based FILs were shown to not be biodegradable, while cholinium and pyridinium-based ones are biodegradable to a significant extent. However, the biodegradation seems to be limited only to the cations and seems unlikely for fluorinated anions. The ecotoxicity and antimicrobial activity of FILs against *Pseudomonas stuteri*, an ubiquitous and opportunistic pathogen, was also studied [41]. The results obtained demonstrated that only very high FIL concentrations inhibit bacterial growth – minimal inhibitory concentrations (MIC) > 100 mM – and that $[N_{1112(OH)}]^+$ was the least toxic cation, followed by $[C_2C_1Im]^+$, and $[C_2C_1py]^+$. Pentanoate-based FILs followed the same trend, but with higher MICs, and are therefore less toxic.

5. Ionic Liquid Applications

The pharmaceutical industry is currently facing challenges related to low productivity, increasing research and development costs, expiring proprietary products and more strict regulatory requirements [22]. The need for new approaches to boost the efficiency of drug development is therefore of the utmost importance and ILs, with their tunability and ease of synthesis, show great potential and versatility. Biocompatible ILs are being studied for several applications, from formulation of pharmaceuticals (as solvents or co-solvents), to protein stabilization and delivery of macromolecules, and even as antimicrobial agents [21,22].

The synthesis of pharmaceutical compounds, for example, can benefit greatly. ILs provide fast microwave heating, which leads to faster and more effective reactions, and when combined with ultrasound irradiation can also be used to accelerate organic reactions [30]. The use of ILs can also reduce the volume of solvents needed, with the further advantage of possibly recycling and re-using the IL [30]. In general, the presence of ILs leads to superior reaction yields, and simplifies separation and purification steps of target products. However, the remaining IL in the final product must be limited in order to ensure safety of use, as is the case with organic solvents [30].

One of the most studied applications for ILs is drug solubilization. Drug efficiency depends on its bioavailability, which is, in turn, directly related to drug permeability and solubility. If a compound presents low solubility, then its dissolution and absorption rates in the body will also be low, and higher doses will be required in order to reach therapeutic efficacy [27]. This is a common issue of modern drug development, especially for drugs delivered orally.

Active pharmaceutical ingredients (APIs) used in drug formulations are usually obtained in crystal form, to maximize purity and thermal stability [22,27]. However, crystalline chemicals can exist as polymorphs that can undergo unpredictable changes, and whose different physicochemical properties can limit solubility, absorption and bioavailability [22,27]. Although volatile organic solvents can be employed to improve API solubility in drug formulation and administration, their use brings up major health and environmental pollution concerns [25].

The greener characteristics of ILs in comparison to traditional organic solvents and their good solvation ability has allowed for the increase in aqueous solubility of APIs, and the selection of anion/cation combinations can significantly impact the mechanism of solubilization [30]. The use of ILs as novel solvents for poorly soluble APIs has been described as enhancing the solubility for antifungal (itraconazole), analgesic (paracetamol), non-steroidal anti-inflammatory (ibuprofen) and anti-cancer drugs (5-fluoracil) [22].

Another strategy for solubilization consists in developing novel liquid forms of solid APIs, where the API is paired with a counterion (API-ILs), thus overcoming not only solubility but also polymorphism drawbacks, and consequently API-ILs exhibit improved bioavailability and therapeutic response when compared to the original solid API [25]. The range of possible combinations between API and counterion can lead to obtaining new drugs with specific physicochemical properties [30]. The development of liquid aspirin with ammonium salt has been reported to show improve characteristics such as poor solubility, bitter taste and tablet size [44].

While growth inhibition of pathogenic and non-pathogenic bacteria and fungi by ILs can hinder some applications in biotechnology, it can be seen as a valuable property in medicine: as drug resistance in microorganisms becomes an ever more pressing issue, the possibility of using ILs as a new class of antimicrobial agents is very timely [27]. ILs have been studied as antibacterial and antifungal agents and demonstrated inhibitory results against resistant and biofilm forming microorganisms, such as *Staphylococcus aureus*, *Salmonella typhi* and *Vibrio cholera*, against which hydroxylammonium ILs were found to be highly active [45].

The potential of ILs as anticancer agents is also being investigated. It has been postulated that ILs may disturb the lipid bilayer of the cell membrane, inducing oxidative stress, DNA damage and apoptosis [27,46]. IL cytotoxicity, which can vary from micro to millimolar ranges, also depends on external factors such as cell type, but is mostly modulated by IL structure. Cation hydrophobicity and lipophilicity correlate with the cytotoxic action, with cholinium ILs demonstrating lower cytotoxicity than ILs based on imidazolium and pyridinium cations [27,46]. Studies concerning the conversion of chemotherapeutic drugs into ILs have been reported. For instance, the conjugation of methotrexate with 1-ethyl-3-methylimidazolium substantially improved its solubility in water and body fluids, while lowering the half-maximum inhibitory constant (IC_{50}) ten times [47]. Hence, the possibility of

developing a therapeutic agent with tailored anticancer activity and reduced toxicity towards the human organism is very desirable.

6. Ionic Liquids and Proteins

Proteins are extremely sensitive to environmental changes induced by temperature, pH, humidity, and salt concentration, and any gradual changes that may occur during manufacturing can lead to protein aggregation over time [11]. This inherent instability limits the use of proteins and enzymes in biological processes and as biopharmaceuticals due to likely negative effects in their function.

The tunable physicochemical properties of ILs (hydrophobicity, hydrogen bonding ability, toxicity) make them suitable solvents for macromolecules, and studies that focused on the prevention and reversal of protein aggregation quickly evolved into the design of ILs for the stabilization of native proteins [21]. As will be discussed in this section, ILs have been shown to enhance the stability and catalytic activity of enzymes and proteins, while demonstrating low toxicity [11,21].

IL impact on protein surface seems to be related to interactions between the ILs and the protein's aqueous environment and surface [27]. These interactions are defined by IL chemical structure and specific cation/anion effects, and protein surface composition, charge, and pH [24]. A critical factor that determines the nature of IL-protein interactions is IL concentration. The amount of IL present in solution will modulate the spatial arrangement of water molecules around protein structure, affecting its stability [11]. IL additives are known to provide stabilization and enhance the activity of enzymes, allowing controlled, reversible folding/unfolding of proteins, and reducing protein aggregation [27]. However, the structural diversity of both ILs and proteins means that a wide range of solvent-protein interactions is possible [24].

Reports concerning the interaction between proteins and ILs have mostly been focused on cholinium- and imizadolium-based cations. Choline ILs, due to their nitrogen core, are seen as unique compounds to solve stabilization issues for both enzymes and therapeutic proteins, while being apparently biocompatible [11,21]. In the presence of cholinium dihydrogenphosphate, $[N_{1112(OH)}][H_2PO_4]$, lysozyme was found to be soluble and interactions with charged residues on the protein surface hindered protein denaturation, while also increasing thermal stability without significant changes to the tertiary structure [48]. Cholinium chloride, $[N_{1112(OH)}][Cl]$, also acted as an appropriate stabilizer against pH induced thermal denaturation of lysozyme [49]. The anion effect on cytochrome c revealed that $[H_2PO_4]^-$ was able to increase enzymatic activity by 25-fold, while $[Glu]^-$ was responsible

for a 50-fold increase. Both conformational and long-term stabilities were achieved with these ILs, among others [50]. Cholinium glutamate and cholinium aspartate ($[N_{1112(OH)}][Glu]$ and $[N_{1112(OH)}][Asp]$, respectively) demonstrated good results for insulin structural stability [51], and cholinium chloride:urea improved the thermal stability of bovine serum albumin (BSA) by 16 K [52].

Imidazolium-based ILs have been reported to function as protein denaturants, refolding enhancers, and suppressors of insoluble aggregates. However, imidazolium-based cations with short alkyl side chains mostly stabilize the protein structure and preserve its activity [27]. For instance, increasing concentration of 1-dodecyl-3-methylimidazolium bromide, $[C_{12}C_1Im][Br]$, significantly affected BSA secondary structure, but impacted lysozyme to a lesser degree [53]. $[C_8C_1Im][Cl]$, 1-octyl-3-methylimidazolium chloride, has been reported to influence lysozyme conformation via hydrophobic interactions and increase activity [54], and prolong cytochrome c stabilization at room temperature [55]. Complete cytochrome c denaturation was verified in the presence of surface-active 1-butyl-3-methylimidazolium octylsulfate ($[C_4C_1Im][C_8OSO_3]$) at concentrations higher than 25 mM, mostly due to electrostatic interactions between the protein and the anion [56]. $[C_4C_1Im][Cl]$, along with $[C_4C_1Im][Br]$ and $[C_4C_1Im][I]$, also denatured stem bromelain at concentrations above 10 mM, but showed no stabilizing effect at lower concentrations [57]. $[I]^-$ was found to be the most destabilizing anion, while $[Cl]^-$ was the least [57]. The use of 1-butyl-3-methylimidazolium thiocyanate ($[C_4C_1Im][SCN]$) as cryoprotectant resulted in denaturation of lysozyme and cytochrome c. However, this effect is predominantly reversible and 90% structural changes were recovered after dialysis [58,59].

The interactions between BSA and SAILs have been investigated by many groups. BSA was shown to be destabilized by 1,3-butylimidazolium chloride ($[C_4C_4Im][Cl]$), $[C_4C_1Im][Cl]$ and $[C_4C_1Im][NO_3]$, since the long alkyl side chain hydrophobic moieties strongly interact with hydrophobic patches of the protein structure [60]. Furthermore, Panda *et al.* [61] verified that cholinium laureate and cholinium palmitate have a strong anion effect, as protein stabilization/destabilization was governed by anion hydrophilicity, and the more hydrophilic (and less surfactant) [Lau] anion had a higher impact on BSA secondary structure destabilization. Modifications on BSA structure were found by Singh and co-workers [62] to depend both on SAIL concentration and type of side chain. While $[C_{12}C_1Im][Cl]$ yielded unordered aggregates, ester and amide functionalized surfactants, $[C_{12}EC_1Im][Cl]$ and $[C_{12}AC_1Im][Cl]$, induced the formation of self-assembled ordered

structures such as long rods and right-handed helical amyloid fibers [62]. Changes in pH also strongly influence the interaction between BSA and 1-hexadecyl-3-methylimidazolium bromide ($[C_{16}C_1Im][Br]$), as the electrostatic interaction between the components is affected [63]. In another study, $[C_{12}C_1Im][Cl]$, and $[C_{16}C_1Im][Cl]$, were found to be capable of destroying BSA fibrillar aggregates [64]. Kundu *et al.* [65] reported that the use of proline-based SAIL was found to encapsulate BSA, increasing its secondary structure content.

The promise of new formulations based on IL-protein interactions to create shelf stable biologics with enhanced treatment efficacy is both very attractive and still in its infancy. The effects on ILs on protein stability, structure and activity are diverse and multifaceted, and depend on the protein being investigated, the IL itself, the concentration used, and other experiment conditions. SAILs, especially, are excellent additives for proteins, with the ability to enhance structural and chemical stability [29]. Therefore, a variety of techniques must be employed when studying these systems, to provide insights into the mechanisms involved.

7. Ionic Liquids and Drug Delivery Systems

The excellent solvent behavior of ILs associated to their ability to navigate through biological barriers make them very desirable as formulation components for the development of drug delivery vehicles, such as ionogels, nanofibers, permeation enhancers and nanocarriers [13,21]. SAILs in particular, due to their surface-active properties which can be tuned through the modification of the structure and dynamics of micellar aggregates, are especially promising for the delivery of drug molecules and have been known to enhance both solubility and permeability of large molecules across cell membranes as well as skin [21,30].

The ability for API encapsulation has been studied using different ILs. Pal *et al.* [66] reported that $[C_{12}C_1im][Cl]$ and $[C_{14}C_1im][Cl]$ form aggregates with lidocaine hydrochloride, improving its dissolution. In comparison to conventional cationic surfactant tetradecyltrimethylammonium bromide (TTAB), $[C_{14}C_1im][Br]$ was found to have superior surface activity and be a better drug carrier of dopamine hydrochloride and acetylcholine hydrochloride [37]. The authors also proposed that these hydrophilic molecules were adsorbed on the surface of the micelle. The delivery of model hydrophilic molecule dextran to the dermis was enhanced two-fold in the presence of choline maleate, with minimal cytotoxicity to human epidermal cells [67]. Choline-based ILs and deep eutectic solvents (DES) have also been reported to deliver molecules with therapeutic efficacy through different routes of administration, such as topically (small interfering RNA for the treatment of psoriasis) [68]; orally (therapeutic antibodies with gastrointestinal absorption) [69]; and transdermally (antigen peptide delivery) [70].

ILs have also been reportedly used in combination with other molecules to form emulsions. Pyne *et al.* [71] developed a cholesterol based SAIL for IL-in-oil microemulsions, that was able to spontaneously form vesicles, while Kandasamy *et al*. [72] demonstrated superior loading capacity for ammonium acetate IL-in-oil microemulsions. A choline chloride/citric acid micelle system was able to encapsulate chemotherapeutic camptothecin with prolonged release [73].

The use of ILs for drug delivery, either as part of a formulation or independently, seems therefore quite promising. One of the main advantages of ILs in this context is the new possibilities regarding route of administration, such as intravenous, oral, transdermal and buccal delivery [21].

8. Transdermal delivery

Skin is the largest barrier in the human body, and its highly organized structure is responsible for protecting the body against injuries and hazardous substances, as well as against excessive loss of water and other essential elements [22]. It is also considered a promising gateway for drug entry, as transdermal drug delivery aims to reach systemic circulation in a safe and non-invasive alternative to parenteral and oral drug administration, while avoiding first-pass elimination and enhancing patient amenability [22,30]. Since the stratum corneum (SC), the outermost layer of skin comprised of corneocytes and lipid layers, is responsible for the hydrophobic barrier function and poses a formidable obstacle to the delivery of hydrophilic molecules, its barrier properties must be reduced either by physical or chemical penetration enhancement techniques [22,74]. Iontophoresis/electroporation, sonophoresis, microneedles and laser ablation are examples of physical penetration enhancement techniques, although these have been associated with the occurrence of burns and scars [74]. ILs, which have demonstrated less toxicity than traditional chemical penetration enhancers thus mitigating possible skin irritation, are currently being studied for facilitating the transdermal delivery of poorly water-soluble drugs [74].

Through the disruption of cellular integrity and fluidization, ILs are able to alter the regular and compact arrangement of corneocytes, leading to a more permeable SC [75]. This destabilization correlates with IL concentration, length of alkyl chain, and anion and cation hydrophobicity [76]. For instance, while hydrophilic ILs are able to open tight junctions within the SC and enhance fluidization (paracellular transport), hydrophobic ILs partition into the epithelial membrane and extract lipid components (transcellular transport) – see Figure 1.8 [25]. Taking into account the composition and highly tunable nature of the ILs, as well
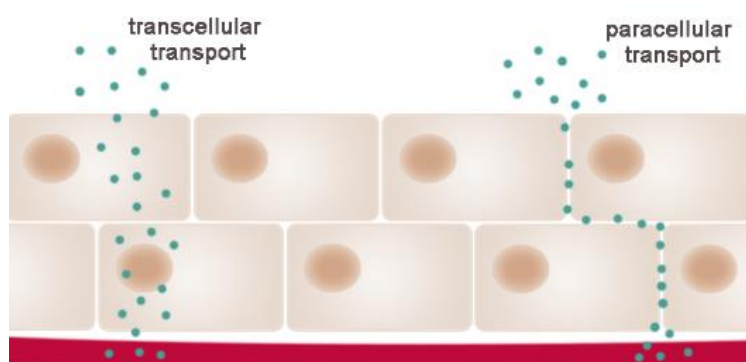
Figure 1.8. Types of transport across cells.

as the therapeutic target, ILs can be designed to present the desirable lipophilicity/hydrophilicity in order to improve the transdermal delivery of hydrophilic drugs as permeation enhancers for drug delivery [30]. A study using a stable formulation comprising hydrophilic 1-hexyl-3-methylimidazolium chloride ($[C_6C_1Im][Cl]$) and hydrophobic $[C_4C_1Im][PF_6]$, noted enhanced skin permeation of a fluorescent probe due to the disruption of the lipidic bilayer [77]. Another report shows that choline geranate (CAGE) was capable of enhanced penetration of antibiotic cefadroxil into the deep tissue layers of the skin without irritation, demonstrating minimal toxicity towards human cell lines [78]. Araki *et al.* [79] found that introducing $[C_{12}mim][NTf_2]$ as permeation enhancer resulted in a significant increase in the skin penetration ability of ovalbumin (OVA), proving the effectiveness of IL-mediated transcutaneous administrations for high molecular weight protein or dug molecules.

Over the years, insulin has been the target of several attempts to improve delivery to patients, since the subcutaneous methods currently available are associated with injection pain, peripheral hyperinsulinemia and noncompliance [80]. Thus, in the search for non-invasive delivery methods for insulin, reports on the use of ILs have been published. Most significantly, Banerjee *et al.* [74] found that CAGE enhanced skin permeation of BSA, OVA and insulin in *ex vivo* porcine skin, allowing for the proteins to penetrate deep into the epidermis and dermis, through lipid extraction from the SC. Furthermore, CAGE did not impact insulin secondary structure, and topical application of insulin-CAGE led to a 40% drop in blood glucose levels in rats. Vaidya *et al.* [81] also successfully delivered insulin to rats using CAGE as the transport facilitator in a biodegradable polymeric patch for buccal delivery. A 7-fold increase in insulin transport across *ex vivo* porcine buccal tissue, and patches placed *in vivo* lowered blood glucose levels with no obvious tissue damage to application site. These CAGE patches allowed for systemic delivery of insulin in a safe, non-invasive and dose-controlled delivery.

9. Scope of Thesis

ILs are a very large family of compounds, with a wide range of interesting and tuneable properties. This versatility, along with rather simple and affordable synthesis and recovery processes, make them very desirable for different applications in the pharmaceutical industry, from catalysts of chemical reactions to stabilizers of drugs.

The use of ILs as DDS is already being widely studied with promising results, including the successful delivery of well folded and active proteins through biological barriers. However, there have been no reports on fluorinated surface-active ILs. The ability of these non-toxic and biocompatible compounds to self-assemble into nanostructures provides an excellent starting point for the study of protein drug encapsulation.

This thesis aims to study the interaction between FILs and three different proteins to assess their potential as drug delivery systems. Initially, interactions with lysozyme, a very stable and well characterized model protein, were studied using biophysical methods to evaluate its activity, stability, and structure (Chapter II). The studies then proceeded with BSA, a larger and more complex protein (Chapter III). Moreover, fluorescence imaging, molecular dynamics, and small angle X-ray scattering (SAXS) were also performed to further characterize the interaction between these two proteins and FILs (Chapter IV). Once the feasibility of the FIL-based DDS was proven, the most promising FIL was used to evaluate the encapsulation of therapeutic protein human phenylalanine hydroxylase (Chapter V).

10. References

1. Leader, B.; Baca, Q.J.; Golan, D.E. Protein therapeutics: a summary and pharmacological classification. *Nat. Rev. Drug Discov.* **2008**, *7*, 21–39, doi:10.1038/nrd2399.

2. Moncalvo, F.; Martinez Espinoza, M.I.; Cellesi, F. Nanosized Delivery Systems for Therapeutic Proteins: Clinically Validated Technologies and Advanced Development Strategies. *Front. Bioeng. Biotechnol.* **2020**, *8*, doi:10.3389/fbioe.2020.00089.

3. Zaman, R.; Islam, R.A.; Ibnat, N.; Othman, I.; Zaini, A.; Lee, C.Y.; Chowdhury, E.H. Current strategies in extending half-lives of therapeutic proteins. *J. Control. Release* **2019**, *301*, 176–189, doi:10.1016/j.jconrel.2019.02.016.

4. Dimitrov, D.S. Therapeutic proteins. *Methods Mol. Biol.* **2012**, *899*, 1–26, doi:10.1007/978-1-61779-921-1_1.

5. Dingman, R.; Balu-Iyer, S. V. Immunogenicity of Protein Pharmaceuticals. *J. Pharm. Sci.* **2019**, *108*, 1637–1654, doi:10.1016/j.xphs.2018.12.014.

6. Lagassé, H.A.D.; McCormick, Q.; Sauna, Z.E. Secondary failure: immune responses to approved protein therapeutics. *Trends Mol. Med.* **2021**, *27*, 1074–1083, doi:10.1016/j.molmed.2021.08.003.

7. Musaimi, O. Al; Shaer, D. Al; Albericio, F.; de la Torre, B.G. 2020 FDA TIDES (peptides and oligonucleotides) harvest. *Pharmaceuticals* **2021**, *14*, 1–14, doi:10.3390/ph14020145.

8. Walsh, G. Biopharmaceutical benchmarks 2018. *Nat. Biotechnol.* **2018**, *36*, 1136–1145, doi:10.1038/nbt.4305.

9. Harada, L.; Pereira, J.; Campos, W.; Silva, E.; Moutinho, C.; Vila, M.; Oliveira Jr., J.; Teixeira, J.; Balcão, V.; Tubino, M.; et al. Insights into Protein-Ionic Liquid Interactions Aiming at Macromolecule Delivery Systems. *J. Braz. Chem. Soc.* **2018**, *29*, 1983–1998, doi:10.21577/0103-5053.20180141.

10. Lino, P.R.; Leandro, J.; Amaro, M.; Gonçalves, L.M.D.; Leandro, P.; Almeida, A.J. In silico and in vitro tailoring of a chitosan nanoformulation of a human metabolic enzyme. *Pharmaceutics* **2021**, *13*, 1–17, doi:10.3390/pharmaceutics13030329.

11. Reslan, M.; Kayser, V. Ionic liquids as biocompatible stabilizers of proteins. *Biophys. Rev.* **2018**, *10*, 781–793, doi:10.1007/s12551-018-0407-6.

12. Dai, C.; Wang, B.; Zhao, H. Microencapsulation peptide and protein drugs delivery system. *Colloids Surfaces B Biointerfaces* **2005**, *41*, 117–120, doi:10.1016/j.colsurfb.2004.10.032.

13. Pedro, S.N.; Freire, C.S.R.; Silvestre, A.J.D.; Freire, M.G. Ionic Liquids in Drug Delivery. *Encyclopedia* **2021**, *1*, 324–339, doi:10.3390/encyclopedia1020027.

14. Banerjee, A.; Ibsen, K.; Brown, T.; Chen, R.; Agatemor, C.; Mitragotri, S. Ionic liquids for oral insulin delivery. *Proc. Natl. Acad. Sci. U. S. A.* **2018**, *115*, 7296–7301, doi:10.1073/pnas.1722338115.

15. Allen, T.M.; Cullis, P.R. Drug Delivery Systems: Entering the Mainstream. *Science (80-.).* **2004**, *303*, 1818–1822, doi:10.1126/science.1095833.

16. Amaral, M.; Pereiro, A.B.; Gaspar, M.M.; Reis, C.P. Recent advances in ionic liquids and nanotechnology for drug delivery. *Nanomedicine* **2020**, *16*, 63–80, doi:10.2217/nnm-2020-0340.

17. De Almeida, T.S.; Júlio, A.; Mota, J.P.; Rijo, P.; Reis, C.P. An emerging integration between ionic liquids and nanotechnology: General uses and future prospects in drug delivery. *Ther. Deliv.* **2017**, *8*, 461–473, doi:10.4155/tde-2017-0002.

18. Ita, K. Microemulsions. *Transdermal Drug Deliv.* **2020**, 97–122, doi:10.1016/B978-0-12-822550-9.00006-5.

19. Simonazzi, A.; Cid, A.G.; Villegas, M.; Romero, A.I.; Palma, S.D.; Bermúdez, J.M. Nanotechnology applications in drug controlled release. *Drug Target. Stimuli Sensitive Drug Deliv. Syst.* **2018**, 81–116, doi:10.1016/B978-0-12-813689-8.00003-3.

20. Patel, G.; Misra, A. Oral Delivery of Proteins and Peptides: Concepts and Applications. *Challenges Deliv. Ther. Genomics Proteomics* **2011**, 481–529, doi:10.1016/B978-0-12-384964-9.00010-4.

21. Curreri, A.M.; Mitragotri, S.; Tanner, E.E.L. Recent Advances in Ionic Liquids in Biomedicine. *Adv. Sci.* **2021**, *8*, 1–18, doi:10.1002/advs.202004819.

22. Adawiyah, N.; Moniruzzaman, M.; Hawatulaila, S.; Goto, M. Ionic liquids as a potential tool for drug delivery systems. *Medchemcomm* **2016**, *7*, 1881–1897, doi:10.1039/c6md00358c.

23. Santos de Almeida, T.; Júlio, A.; Saraiva, N.; Fernandes, A.S.; Araújo, M.E.M.; Baby, A.R.; Rosado, C.; Mota, J.P. Choline- versus imidazole-based ionic liquids as functional ingredients in topical delivery systems: cytotoxicity, solubility, and skin permeation studies. *Drug Dev. Ind. Pharm.* **2017**, *43*, 1858–1865, doi:10.1080/03639045.2017.1349788.

24. Bui-Le, L.; Clarke, C.J.; Bröhl, A.; Brogan, A.P.S.; Arpino, J.A.J.; Polizzi, K.M.; Hallett, J.P. Revealing the complexity of ionic liquid–protein interactions through a multi-technique investigation. *Commun. Chem.* **2020**, *3*, 1–9, doi:10.1038/s42004-020-0302-5.

25. Huang, W.; Wu, X.; Qi, J.; Zhu, Q.; Wu, W.; Lu, Y.; Chen, Z. Ionic liquids: green and tailor-made solvents in drug delivery. *Drug Discov. Today* 2020, *25*, 901–908.

26. Ali, M.K.; Moshikur, R.M.; Wakabayashi, R.; Tahara, Y.; Moniruzzaman, M.; Kamiya, N.; Goto, M. Synthesis and characterization of choline–fatty-acid-based ionic liquids:

A new biocompatible surfactant. *J. Colloid Interface Sci.* **2019**, *551*, 72–80, doi:10.1016/j.jcis.2019.04.095.

27. Egorova, K.S.; Gordeev, E.G.; Ananikov, V.P. Biological Activity of Ionic Liquids and Their Application in Pharmaceutics and Medicine. *Chem. Rev.* 2017, *117*, 7132–7189.

28. Santos, J.I.; Gonçalves, A.M.M.; Pereira, J.L.; Figueiredo, B.F.H.T.; Silva, F.A.E.; Coutinho, J.A.P.; Ventura, S.P.M.; Gonçalves, F. Environmental safety of cholinium-based ionic liquids: assessing structure-ecotoxicity relationships. *Green Chem.* **2015**, *17*, 4657–4668, doi:10.1039/c5gc01129a.

29. Buettner, C.S.; Cognigni, A.; Schröder, C.; Bica-Schröder, K. Surface-active ionic liquids: A review. *J. Mol. Liq.* **2022**, *347*, 118160, doi:10.1016/j.molliq.2021.118160.

30. Pedro, S.N.; Freire, C.S.R.; Silvestre, A.J.D.; Freire, M.G. The role of ionic liquids in the pharmaceutical field: An overview of relevant applications. *Int. J. Mol. Sci.* **2020**, *21*, 1–50, doi:10.3390/ijms21218298.

31. Thoppil, A.A.; Chennuri, B.K.; Gardas, R.L. Insights into the structural changes of bovine serum albumin in ethanolammonium laurate based surface active ionic liquids. *J. Mol. Liq.* **2019**, *290*, 111229, doi:10.1016/J.MOLLIQ.2019.111229.

32. Łuczak, J.; Jungnickel, C.; Markiewicz, M.; Hupka, J. Solubilization of Benzene, Toluene, and Xylene (BTX) in Aqueous Micellar Solutions of Amphiphilic Imidazolium Ionic Liquids. *J. Phys. Chem. B* **2013**, *117*, 5653–5658, doi:10.1021/jp3112205.

33. Tong, Y.; Han, L.; Yang, Y. Microemulsion Extraction of Gold(III) from Hydrochloric Acid Medium Using Ionic Liquid as Surfactant and Extractant. *Ind. Eng. Chem. Res.* **2012**, *51*, 16438–16443, doi:10.1021/ie301644t.

34. Akl, Z.F.; Hegazy, M.A. Selective cloud point extraction of thorium (IV) using tetraazonium based ionic liquid. *J. Environ. Chem. Eng.* **2020**, *8*, 104185, doi:https://doi.org/10.1016/j.jece.2020.104185.

35. Bamdad, F.; Raziani, A. Application of surface-active ionic liquids in micelle-mediated extraction methods: pre-concentration of cadmium ions by surface-active ionic liquid-assisted cloud point extraction. *J. Iran. Chem. Soc.* **2020**, *17*, 327–332, doi:10.1007/s13738-019-01770-8.

36. Pino, V.; Germán-Hernández, M.; Martín-Pérez, A.; Anderson, J.L. Ionic Liquid-Based Surfactants in Separation Science. *Sep. Sci. Technol.* **2012**, *47*, 264–276, doi:10.1080/01496395.2011.620589.

37. Mahajan, S.; Sharma, R.; Mahajan, R.K. An Investigation of Drug Binding Ability of a Surface Active Ionic Liquid: Micellization, Electrochemical, and Spectroscopic Studies. *Langmuir* **2012**, *28*, 17238–17246, doi:10.1021/la303193n.

38. Pereiro, A.B.; Araújo, J.M.M.; Teixeira, F.S.; Marrucho, I.M.; Piñeiro, M.M.; Rebelo, L.P.N. Aggregation behavior and total miscibility of fluorinated ionic liquids in water.

Langmuir **2015**, *31*, 1283–1295, doi:10.1021/la503961h.

39.   Krafft, M.P. Fluorocarbons and fluorinated amphiphiles in drug delivery and biomedical research. *Adv. Drug Deliv. Rev.* **2001**, *47*, 209–228, doi:10.1016/S0169-409X(01)00107-7.

40.   Vieira, N.S.M.; Stolte, S.; Araújo, J.M.M.; Rebelo, L.P.N.; Pereiro, A.B.; Markiewicz, M. Acute Aquatic Toxicity and Biodegradability of Fluorinated Ionic Liquids. *ACS Sustain. Chem. Eng.* **2019**, *7*, 3733–3741, doi:10.1021/acssuschemeng.8b03653.

41.   Vieira, N.S.M.; Oliveira, A.L.S.; Araújo, J.M.M.; Gaspar, M.M.; Pereiro, A.B. Ecotoxicity and Hemolytic Activity of Fluorinated Ionic Liquids. *Sustain. Chem.* **2021**, *2*, 115–126, doi:10.3390/suschem2010008.

42.   Vieira, N.S.M.; Bastos, J.C.; Rebelo, L.P.N.; Matias, A.; Araújo, J.M.M.; Pereiro, A.B. Human cytotoxicity and octanol/water partition coefficients of fluorinated ionic liquids. *Chemosphere* **2019**, *216*, 576–586, doi:10.1016/j.chemosphere.2018.10.159.

43.   Vieira, N.S.M.; Bastos, J.C.; Hermida-Merino, C.; Pastoriza-Gallego, M.J.; Rebelo, L.P.N.; Piñeiro, M.M.; Araújo, J.M.M.; Pereiro, A.B. Aggregation and phase equilibria of fluorinated ionic liquids. *J. Mol. Liq.* **2019**, *285*, 386–396, doi:10.1016/J.MOLLIQ.2019.04.086.

44.   Egorova, K.S.; Seitkalieva, M.M.; Posvyatenko, A. V; Khrustalev, V.N.; Ananikov, V.P. Cytotoxic Activity of Salicylic Acid-Containing Drug Models with Ionic and Covalent Binding. *ACS Med. Chem. Lett.* **2015**, *6*, 1099–1104, doi:10.1021/acsmedchemlett.5b00258.

45.   Ismail Hossain, M.; El-Harbawi, M.; Noaman, Y.A.; Bustam, M.A.B.; Alitheen, N.B.M.; Affandi, N.A.; Hefter, G.; Yin, C.Y. Synthesis and anti-microbial activity of hydroxylammonium ionic liquids. *Chemosphere* **2011**, *84*, 101–104, doi:10.1016/J.CHEMOSPHERE.2011.02.048.

46.   Guncheva, M. Ionic Liquids for Anticancer Application. *Encycl. Ion. Liq.* **2019**, 1–6, doi:10.1007/978-981-10-6739-6_6-1.

47.   Moshikur, R.M.; Chowdhury, M.R.; Wakabayashi, R.; Tahara, Y.; Moniruzzaman, M.; Goto, M. Ionic liquids with methotrexate moieties as a potential anticancer prodrug: Synthesis, characterization and solubility evaluation. *J. Mol. Liq.* **2019**, *278*, 226–233, doi:10.1016/J.MOLLIQ.2019.01.063.

48.   Weaver, K.D.; Vrikkis, R.M.; Van Vorst, M.P.; Trullinger, J.; Vijayaraghavan, R.; Foureau, D.M.; McKillop, I.H.; MacFarlane, D.R.; Krueger, J.K.; Elliott, G.D. Structure and function of proteins in hydrated choline dihydrogen phosphate ionic liquid. *Phys. Chem. Chem. Phys.* **2012**, *14*, 790–801, doi:10.1039/C1CP22965F.

49.   Jha, I.; Rani, A.; Venkatesu, P. Sustained Stability and Activity of Lysozyme in Choline Chloride against pH Induced Denaturation. *ACS Sustain. Chem. Eng.* **2017**, *5*, 8344–8355, doi:10.1021/acssuschemeng.7b02126.

50. Bisht, M.; Mondal, D.; Pereira, M.M.; Freire, M.G.; Venkatesu, P.; Coutinho, J.A.P. Long-term protein packaging in cholinium-based ionic liquids: improved catalytic activity and enhanced stability of cytochrome c against multiple stresses. *Green Chem.* **2017**, *19*, 4900–4911, doi:10.1039/C7GC02011B.

51. Guncheva, M.; Ossowicz, P.; Janus, E.; Todinova, S.; Yancheva, D. Elucidation of the effect of some cholinium amino acid ionic liquids on the thermal and the conformational stability of insulin. *J. Mol. Liq.* **2019**, *283*, 257–262, doi:10.1016/J.MOLLIQ.2019.03.074.

52. Bhakuni, K.; Yadav, N.; Venkatesu, P. A novel amalgamation of deep eutectic solvents and crowders as biocompatible solvent media for enhanced structural and thermal stability of bovine serum albumin. *Phys. Chem. Chem. Phys.* **2020**, *22*, 24410–24422, doi:10.1039/D0CP04397D.

53. Cao, C.; Zhou, Z.-L.; Zheng, L.; Huang, Q.-L.; Du, F.-P. Dilational rheology of different globular protein with imidazolium-based ionic liquid surfactant adsorption layer at the decane/water interface. *J. Mol. Liq.* **2017**, *233*, 344–351, doi:https://doi.org/10.1016/j.molliq.2017.02.121.

54. Kumari, M.; Dohare, N.; Maurya, N.; Dohare, R.; Patel, R. Effect of 1-methyl-3-octyleimmidazolium chloride on the stability and activity of lysozyme: a spectroscopic and molecular dynamics studies. *J. Biomol. Struct. Dyn.* **2017**, *35*, 2016–2030, doi:10.1080/07391102.2016.1204946.

55. Singh, U.K.; Kumari, M.; Khan, S.H.; Bohidar, H.B.; Patel, R. Mechanism and Dynamics of Long-Term Stability of Cytochrome c Conferred by Long-Chain Imidazolium Ionic Liquids at Low Concentration. *ACS Sustain. Chem. Eng.* **2018**, *6*, 803–815, doi:10.1021/acssuschemeng.7b03168.

56. Singh, U.K.; Kumari, M.; Patel, R. Dynamics of cytochrome c in surface active ionic liquid: A study of preferential interactions towards denaturation. *J. Mol. Liq.* **2018**, *268*, 840–848, doi:https://doi.org/10.1016/j.molliq.2018.07.116.

57. Kumar, P.K.; Jha, I.; Venkatesu, P.; Bahadur, I.; Ebenso, E.E. A comparative study of the stability of stem bromelain based on the variation of anions of imidazolium-based ionic liquids. *J. Mol. Liq.* **2017**, *246*, 178–186, doi:https://doi.org/10.1016/j.molliq.2017.09.037.

58. Takekiyo, T.; Yamazaki, K.; Yamaguchi, E.; Abe, H.; Yoshimura, Y. High Ionic Liquid Concentration-Induced Structural Change of Protein in Aqueous Solution: A Case Study of Lysozyme. *J. Phys. Chem. B* **2012**, *116*, 11092–11097, doi:10.1021/jp3057064.

59. Takekiyo, T.; Ishikawa, Y.; Yoshimura, Y. Cryopreservation of Proteins Using Ionic Liquids: A Case Study of Cytochrome c. *J. Phys. Chem. B* **2017**, *121*, 7614–7620, doi:10.1021/acs.jpcb.7b05158.

60. Shu, Y.; Liu, M.; Chen, S.; Chen, X.; Wang, J. New insight into molecular interactions

of imidazolium ionic liquids with bovine serum albumin. *J. Phys. Chem. B* **2011**, *115*, 12306–12314, doi:10.1021/jp2071925.

61.   Panda, S.; Kundu, K.; Basaiahgari, A.; Singh, A.P.; Senapati, S.; Gardas, R.L. Aggregation behaviour of biocompatible choline carboxylate ionic liquids and their interactions with biomolecules through experimental and theoretical investigations. *New J. Chem.* **2018**, *42*, 7105–7118, doi:10.1039/c8nj00336j.

62.   Singh, G.; Singh Kang, T. Ionic Liquid Surfactant Mediated Structural Transitions and Self-Assembly of Bovine Serum Albumin in Aqueous Media: Effect of Functionalization of Ionic Liquid Surfactants. *J. Phys. Chem. B* **2015**, *119*, 10573–10585, doi:10.1021/acs.jpcb.5b04854.

63.   Cao, C.; Lei, J.; Huang, T.; Du, F.-P. Impact of ionic liquid-type imidazolium surfactant addition on dynamic properties of BSA adsorption layers at different pH. *Soft Matter* **2014**, *10*, 8896–8904, doi:10.1039/C4SM01666A.

64.   Kundu, S.; Banerjee, C.; Sarkar, N. Inhibiting the Fibrillation of Serum Albumin Proteins in the Presence of Surface Active Ionic Liquids (SAILs) at Low pH: Spectroscopic and Microscopic Study. *J. Phys. Chem. B* **2017**, *121*, 7550–7560, doi:10.1021/acs.jpcb.7b03457.

65.   Kundu, K.; Singh, A.P.; Panda, S.; Singh, V.; Gardas, R.L.; Senapati, S. Study on the Conformation of Entrapped Protein inside the Reverse Micellar Confinement Based on the Amino Acid Derived Ionic Liquid. *ChemistrySelect* **2018**, *3*, 4768–4776, doi:10.1002/slct.201800918.

66.   Pal, A.; Yadav, A. Binding interactions of anesthetic drug with surface active ionic liquid. *J. Mol. Liq.* **2016**, *222*, 471–479, doi:10.1016/J.MOLLIQ.2016.07.076.

67.   Wu, X.; Chen, Z.; Li, Y.; Yu, Q.; Lu, Y.; Zhu, Q.; Li, Y.; An, D.; Qi, J.; Wu, W. Improving dermal delivery of hydrophilic macromolecules by biocompatible ionic liquid based on choline and malic acid. *Int. J. Pharm.* **2019**, *558*, 380–387, doi:10.1016/j.ijpharm.2019.01.021.

68.   Abhirup, M.; Ninad, K.; Charles, R.; Vimisha, D.; Anvay, U.; E., I.D.; Samir, M.; Mandal, A.; Kumbhojkar, N.; Reilly, C.; et al. Treatment of psoriasis with NFKBIZ siRNA using topical ionic liquid formulations. *Sci. Adv.* **2020**, *6*, eabb6049, doi:10.1126/sciadv.abb6049.

69.   Angsantikul, P.; Peng, K.; Curreri, A.M.; Chua, Y.; Chen, K.Z.; Ehondor, J.; Mitragotri, S. Ionic Liquids and Deep Eutectic Solvents for Enhanced Delivery of Antibodies in the Gastrointestinal Tract. *Adv. Funct. Mater.* **2021**, *31*, 2002912, doi:https://doi.org/10.1002/adfm.202002912.

70.   Tahara, Y.; Morita, K.; Wakabayashi, R.; Kamiya, N.; Goto, M. Biocompatible ionic liquid enhances transdermal antigen peptide delivery and preventive vaccination effect. *Mol. Pharm.* **2020**, *17*, 3845–3856, doi:10.1021/acs.molpharmaceut.0c00598.

71. Pyne, A.; Kuchlyan, J.; Maiti, C.; Dhara, D.; Sarkar, N. Cholesterol Based Surface Active Ionic Liquid That Can Form Microemulsions and Spontaneous Vesicles. *Langmuir* **2017**, *33*, 5891–5899, doi:10.1021/acs.langmuir.7b01158.

72. Kandasamy, S.; Moniruzzaman, M.; Sivapragasam, M.; Shamsuddin, M.R.; Mutalib, M.I.A. Formulation and characterization of acetate based ionic liquid in oil microemulsion as a carrier for acyclovir and methotrexate. *Sep. Purif. Technol.* **2018**, *196*, 149–156, doi:https://doi.org/10.1016/j.seppur.2017.08.044.

73. Pradeepkumar, P.; Elgorban, A.M.; Bahkali, A.H.; Rajan, M. Natural solvent-assisted synthesis of amphiphilic co-polymeric nanomicelles for prolonged release of camptothecin delivery. *New J. Chem.* **2018**, *42*, 10366–10375, doi:10.1039/C8NJ00901E.

74. Banerjee, A.; Ibsen, K.; Iwao, Y.; Zakrewsky, M.; Mitragotri, S. Transdermal Protein Delivery Using Choline and Geranate (CAGE) Deep Eutectic Solvent. *Adv. Healthc. Mater.* **2017**, *6*, doi:10.1002/adhm.201601411.

75. Zhang, D.; Wang, H.-J.; Cui, X.-M.; Wang, C.-X. Evaluations of imidazolium ionic liquids as novel skin permeation enhancers for drug transdermal delivery. *Pharm. Dev. Technol.* **2017**, *22*, 511–520, doi:10.3109/10837450.2015.1131718.

76. Jing, B.; Lan, N.; Qiu, J.; Zhu, Y. Interaction of Ionic Liquids with a Lipid Bilayer: A Biophysical Study of Ionic Liquid Cytotoxicity. *J. Phys. Chem. B* **2016**, *120*, 2781–2789, doi:10.1021/acs.jpcb.6b00362.

77. Dobler, D.; Schmidts, T.; Klingenhöfer, I.; Runkel, F. Ionic liquids as ingredients in topical drug delivery systems. *Int. J. Pharm.* **2013**, *441*, 620–627, doi:https://doi.org/10.1016/j.ijpharm.2012.10.035.

78. Zakrewsky, M.; Lovejoy, K.S.; Kern, T.L.; Miller, T.E.; Le, V.; Nagy, A.; Goumas, A.M.; Iyer, R.S.; Del Sesto, R.E.; Koppisch, A.T.; et al. Ionic liquids as a class of materials for transdermal delivery and pathogen neutralization. *Proc. Natl. Acad. Sci. U. S. A.* **2014**, *111*, 13313–13318, doi:10.1073/pnas.1403995111.

79. Araki, S.; Wakabayashi, R.; Moniruzzaman, M.; Kamiya, N.; Goto, M. Ionic liquid-mediated transcutaneous protein delivery with solid-in-oil nanodispersions. *Med. Chem. Commun.* **2015**, *6*, 2124–2128, doi:10.1039/C5MD00378D.

80. Shah, R.B.; Patel, M.; Maahs, D.M.; Shah, V.N. Insulin delivery methods: Past, present and future. *Int. J. Pharm. Investig.* **2016**, *6*, 1–9, doi:10.4103/2230-973X.176456.

81. Vaidya, A.; Mitragotri, S. Ionic liquid-mediated delivery of insulin to buccal mucosa. *J. Control. Release* **2020**, *327*, 26–34, doi:10.1016/j.jconrel.2020.07.037.

CHAPTER II

Investigating the impact of Fluorinated Ionic Liquids on the structure and function of Lysozyme

MMS Alves contribution to the work described in this chapter: MMS Alves optimized and performed differential scanning fluorimetry, enzymatic activity and dynamic light scattering assays. The author also analysed the corresponding data and contributed to the manuscript preparation.

This chapter contains published data:

Alves, M.; Vieira, N.S.M.; Rebelo, L.P.N.; Araújo, J.M.M.; Pereiro, A.B.; Archer, M. Fluorinated ionic liquids for protein drug delivery systems: Investigating their impact on the structure and function of lysozyme. *Int. J. Pharm.* **2017**, *526*, 309–320, doi:10.1016/j.ijpharm.2017.05.002.

1. Abstract

Since the approval of recombinant human insulin by FDA in 1982, over 200 proteins are currently available for pharmaceutical use to treat a wide range of diseases. However, innovation is still required to develop effective approaches for drug delivery. Our aim is to investigate the potential use of fluorinated ionic liquids (FILs) as drug delivery systems (DDS) for therapeutic proteins. Some initial parameters need to be assessed before further studies can proceed. This work evaluates the impact of FILs on the stability, function, structure, and aggregation state of lysozyme. Different techniques were used for this purpose, which included differential scanning fluorimetry (DSF), spectrophotometric, circular dichroism (CD), and dynamic light scattering (DLS) assays, along with scanning and transmission electron microscopy (SEM/TEM). Ionic liquids composed of cholinium-, imidazolium- or pyridinium- derivatives were combined with different anions and analysed at different concentrations in aqueous solutions (below and above the critical aggregation concentration, *CAC*). The results herein presented show that the addition of ionic liquids had no significant effect on the stability and hydrolytic activity of lysozyme. Moreover, a distinct behaviour was observed in DLS experiments for non-surfactant and surfactant ionic liquids, with the latter encapsulating the protein at concentrations above the *CAC*. These results encourage us to further study ionic liquids as promising tools for DDS of protein drugs.

2. Introduction

The pharmaceutical market is undergoing increasing economic pressure due to the reduction of healthcare investment, increased competition from generic medications and high rates of drug development failure in clinical trials [1]. This situation, together with the demand of society and authorities for safer and more efficient drugs, has contributed to the revived interest in protein drug candidates. Therapeutic proteins, which are natural biological products, emerged in the early 1980s and promise to become a kind of panacea for all known diseases [2]. More than 200 natural and modified therapeutic proteins have been approved for clinical use in the European Union and the USA [1]. Therapeutic proteins are undergoing clinical trials for the treatment of cancers, Alzheimer's, immune disorders, infectious diseases, Parkinson's, autoimmune diseases and AIDS/HIV, among others [3,4]. However, therapeutic proteins have their downsides: i) they are very sensitive to environmental conditions (e.g. they cannot be delivered orally due to the risk of degradation in the acidic environment of the gastrointestinal tract); ii) their three-dimensional structure, spatial occupation and hydrophilic/hydrophobic nature can hinder *in vivo* delivery; iii) they have poor bioavailability due to their short half-lives in the bloodstream resulting from their degradation by enzymes such as proteases; iv) high doses are needed to obtain therapeutic efficacy, which may lead to side effects and toxicity; and v) they are most commonly administered by intravenous injections, which are not always well tolerated by the recipient [5]. Drug delivery systems (DDS) can be the solution to these various obstacles because they can minimize adverse side effects, improve the action of a drug through faster onset, time-controlled or site-specific delivery, or reduce the drug dosage needed [3].

In recent years, ionic liquids (ILs) have attracted considerable attention because of their biological and pharmaceutical potential. Specifically, their ability to solubilize and stabilize proteins *in vitro* for extended times has been studied [6,7]. Previous investigations have emphasized the potential of ILs to dissolve poorly soluble active pharmaceutical ingredients as well as biochemical compounds, such as nucleic acid bases [8,9]. The first work using ILs as drug delivery devices was reported in 2010 [10]. Since then, these compounds have been studied as additives in several formulations as well as drug solubility enhancers [11–14].

Although the number of publications dealing with ILs has grown exponentially, there are still numerous quasi-unexplored topics, such as the fluorinated ionic liquids (FILs) family,

herein defined as ILs with fluorous tags equal to or longer than four carbon atoms. The interest in these novel FILs resides in their ability to combine the best properties of highly fluorinated materials (outstanding chemical and biological inertness, low surface tension and unique components and tools for the engineering of stable, self-assembled supramolecular and colloidal systems) with those of many ionic liquids in general (vanishing vapour pressure, tuneable solvent quality, high thermal stability, high electrical conductivity, non-flammability and greener potential). Inert fluorinated compounds have been widely used in relevant biomedical applications, e.g. as imaging agents [15–17], and as fluorocarbon gels, nano compartmented supramolecular assemblies and colloids [18,19]. Similarly, they have been employed in the control and stabilization of emulsions, microbubbles and other colloids [20,21] as well as in the pulmonary delivery of drugs and genes [22] and oxygen therapeutics [23–25] where these compounds are used as gas carriers in liquid ventilation and intravenous formulations.

Several studies report the development of DDS for therapeutic proteins using liposomes, microparticles, nanoparticles, fluorocarbons surfactants and microencapsulation [5,26,27]. Additionally, an area referred to as protein engineering has discussed and reviewed the general effects on the essential properties of peptides and proteins arising from the incorporation of fluorinated amino acids [28]. Nevertheless, more than a decade of research in protein DDS has still failed to produce efficient systems. Studies tackling FIL surfactants as drug delivery systems for therapeutic proteins are not yet available.

Novel surfactants based on FILs might increase the safety and effectiveness of therapeutic proteins, increasing the pre-intake protection until reaching the target receptor, while decreasing their immunogenicity. Furthermore, playing with the van der Waals, coulombic and hydrogen bonding interactions, the size of fluorinated domains [29], surfactant behaviour, and the solubility in water and biological fluids [30] will provide the ingredients needed to use FILs in biological applications where fluorocarbon compounds in general present the handicap of overly low solubility in water and biological fluids.

The main purpose of this work is to take the first steps into the development of a novel and improved strategy for protein drug delivery using biocompatible FILs with reduced immunogenicity that might deliver protein drugs to the body at therapeutic levels. The FILs analysed in this study have been selected based on previous works. They are miscible in water with improved surfactant behaviour as compared to traditional surfactants [30] and present low cytotoxicity in four different human cell lines [31,32]. In these reports, it is shown

that only the perfluorooctanesulfonate anion presents some cytotoxicity in one of the human cell cultures at high FIL concentrations (Caco-2 cell line with log EC_{50} = 3.65, 4467 µM; but HepG2 with log EC_{50} >4, >10000 µM) [31]. Even so, this value is negligible when compared with the corresponding acid, perfluorooctane sulfonic acid (log EC_{50} = 1.48, 30 µM in PC12 cells) [33], which belongs to a new class of environmental contaminants, globally distributed and persistent, bio-accumulative and toxic to various species [34]. It is thus important to become aware of the expansion of production and use of these perfluorinated compounds in the forthcoming years due to their utility, economic value and industrial application [34]. While the perfluorobutanesulfonate anion, $[C_4F_9SO_3]^-$, shares some of the oleophobic and hydrophobic properties of perfluorooctanesulfonate, $[C_8F_{17}SO_3]^-$, it is not considered to be as bio-accumulative or toxic [35]. The FILs based on the perfluorobutanesulfonate anion studied herein might be used as neoteric alternative compounds, being more environmentally friendly and presenting tuneable physicochemical properties as compared to other fluorinated compounds. Furthermore, it has been shown that the critical aggregation concentration (*CAC*) values of fluorinated surfactants are analogous to those of hydrogenated surfactants with a chain length approximately 1.5 times longer [30,36,37]. FILs with only four carbon atoms used in this work improve the surfactant power of conventional perfluorosurfactants with eight carbon atoms and the hydrogenated counterparts. These FILs have also been found to have small octanol-water partition coefficients compared with traditional solvents [38]. Taking these studies into account, the size of the side fluorinated alkyl chain must be smaller than eight carbon atoms in order to avoid toxicity. Nonetheless, the physiological safety, biodegradability, and health studies, among others, will have to be carried out to fully evaluate the actual possible application of these FILs.

Lysozyme (or muramidase, EC 3.2.1.17) is a ubiquitous protein present in a wide range of biological fluids and tissues including bacteria, avian egg, plant, and animal secretions. It is well known for its antibacterial properties by breaking the bonds between N-acetylglucosamine and N-acetylmuramic acid, which are peptidoglycan components in the cell wall of Gram-positive bacteria. Lysozyme also exhibits antiviral, antitumor and immune modulatory activities [39–45]. Moreover, lysozyme has been thoroughly characterized and often used as a model protein in a variety of studies, some of which involving traditional ionic liquids [46–51].

The main goal of this work is to investigate the effect of FILs on the stability, structure, and activity of lysozyme using various biophysical and biochemical techniques. Two traditional and non-surfactant ILs have also been included in this work to compare their behaviour with the novel FILs. Finally, the self-aggregation behaviour of this protein with surfactants based on FILs in aqueous solutions has been characterized using dynamic light scattering (DLS), scanning electron microscopy (SEM) and transmission electron microscopy (TEM). The use of novel, biocompatible and greener FILs shows tremendous promise in improving the bioavailability, stability, structure and efficacy of therapeutic proteins. Protein drugs are a biocompatible option for the pharmaceutical industry due to the relative ease with which they gain authorization for clinical use.

3. Experimental Procedures

3.1 Materials
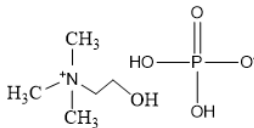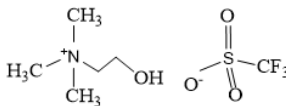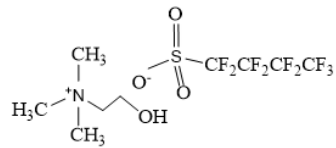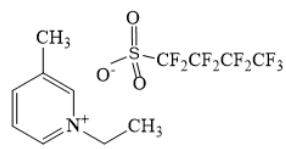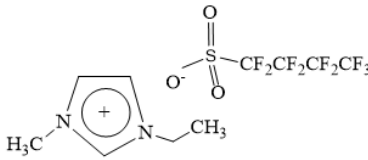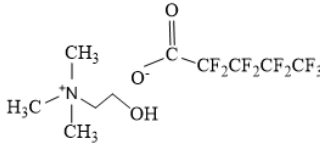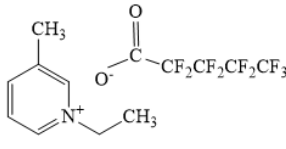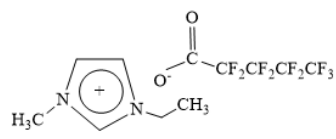
Lyophilized lysozyme from chicken egg white (L6876), *Micrococcus lysodeikticus* lyophilized cells (M3770) and Potassium Phosphate Monobasic (purity 99.0 %, P0662) were purchased from Sigma-Aldrich; Potassium Phosphate Dibasic (purity 99.0 %, P749.3) from Roth and SYPRO Orange (S6650) from ThermoFisher.

Cholinium ((2-hydroxyethyl)trimethylammonium) dihydrogen phosphate, $[N_{1112(OH)}][H_2PO_4]$ (> 98% mass fraction purity), cholinium perfluorobutanesulfonate, $[N_{1112(OH)}][C_4F_9SO_3]$ (> 97% mass fraction purity), 1-ethyl-3-methylimidazolium perfluorobutanesulfonate, $[C_2C_1Im][C_4F_9SO_3]$ (> 97% mass fraction purity), 1-ethyl-3-methylpyridinium perfluorobutanesulfonate, $[C_2C_1py][C_4F_9SO_3]$ (> 99% mass fraction purity) and cholinium trifluoromethanesulfonate, $[N_{1112(OH)}][CF_3SO_3]$ (> 97% mass fraction purity) were supplied by IoLiTec GmbH. Cholinium perfluoropentanoate, $[N_{1112(OH)}][C_4F_9CO_2]$ (> 98% mass fraction purity), 1-ethyl-3-methylimidazolium perfluoropentanoate, $[C_2C_1Im][C_4F_9CO_2]$ (> 98% mass fraction purity) and 1-ethyl-3-methylpyridinium perfluoropentanoate, $[C_2C_1py][C_4F_9CO_2]$, (> 99% mass fraction purity), were synthesized and characterized in our laboratory.[52,53] To reduce the volatile chemicals and water contents, all ILs were dried under vacuum ($3 \cdot 10^{-2}$ Torr) with vigorous stirring at about 323 K for at least 2 days, immediately prior to their use. No further purification was carried out and the purity of all ILs was checked by ^{1}H and ^{19}F NMR. The chemical structures of the ionic liquids used in this work are presented in Table 2.1.

3.2 Differential Scanning Fluorimetry

Experiments were performed in an iCycle iQ5 real time PCR detection system (Bio-Rad), equipped with a charge-coupled device camera and a Cy3 filter with excitation and emission wavelengths of 490 and 575 nm, respectively. The assay was performed on 96-well plates (low profile plate, Bio-Rad), with a final volume of 20 µL for each reaction. A first screen was done to examine the fluorescence spectra with different protein and dye concentrations to choose the best ratio for the DSF assays. Lysozyme was tested in the range of 0.2 to 0.5 mg·mL^{-1} at 0.1 intervals with SYPRO Orange diluted to 5, 10 and 25-fold

Table 2.1. Chemical structures and acronyms of the ionic liquids (ILs).

IL Designation	Chemical Structure	Critical Aggregation Concentration (cac) in water
Cholinium dihydrogen phosphate $[N_{1112(OH)}][H_2PO_4]$		Non-surfactant
Cholinium trifluoromethanesulfonate $[N_{1112(OH)}][CF_3SO_3]$		Non-surfactant
Cholinium perfluorobutanesulfonate $[N_{1112(OH)}][C_4F_9SO_3]$		16.07 mM (0.65% *v/v*) [30]
1-Ethyl-3-methylpyridinium perfluorobutanesulfonate $[C_2C_1py][C_4F_9SO_3]$		13.82 mM (0.58% *v/v*) [30]
1-Ethyl-3-methylimidazolium perfluorobutanesulfonate $[C_2C_1Im][C_4F_9SO_3]$		14.55 mM (0.60% *v/v*) [30]
Cholinium perfluoropentanoate $[N_{1112(OH)}][C_4F_9CO_2]$		*n.a.*
1-Ethyl-3-methylpyridinium perfluoropentanoate $[C_2C_1py][C_4F_9CO_2]$		*n.a.*
1-Ethyl-3-methylimidazolium perfluoropentanoate $[C_2C_1Im][C_4F_9CO_2]$		*n.a.*

(stock solution is 5000x). The selected conditions for this study consist of lysozyme at 0.2 mg·mL^{-1} and SYPRO orange dye in a five-fold dilution, as this combination yields the finest signal in the fluorescence spectrum. The subsequent DSF experiments to investigate the effect of ionic liquids on the stability of the protein were carried out using ionic liquid

concentrations ranging from 0 to 1.2% *v/v*. All samples were prepared in the same buffer – 0.1 M KH_2PO_4/K_2HPO_4 at pH 7. Blank assays were carried out to assess the behaviour of ILs with SYPRO Orange dye in the absence of lysozyme. The plate was sealed with optical quality sealing tape (Bio-Rad) and heated from 293.15 to 363.15 K in 1 K increments and a 60 s equilibration time was used, followed by a fluorescence readout. Measurements were done in duplicates from two independent assays. When the fluorescence intensity of the dye in the presence of the protein is plotted as a function of temperature, the apparent melting temperature of the protein can be derived from the inflection point of the resulting sigmoidal graph.

3.3 Enzymatic activity

This functional assay relies on the lysozyme lytic activity against the cell wall of *Micrococcus lysodeikticus* as the substrate. The reaction follows the change in turbidity of a bacterial suspension by measuring the decrease of absorbance at 450 nm with a common spectrophotometer or a microplate reader, which allows rapid data acquisition. The BMG FLUOstar Optima microplate reader with flat-bottomed 96-well plates (Nunc) was herein used to monitor the A_{450} along time and the activity assays were based on protocols previously described [54,55]. Lysozyme solutions at 0.2 mg·mL^{-1} were prepared with ionic liquids at different concentrations (0, 0.1, 0.6, 1 and 1.2% *v/v*) in 66 mM potassium phosphate buffer pH 6.2 and incubated at room temperature for 30 minutes. A 0.3 mg·mL^{-1} substrate solution of *M. lysodeikticus* was prepared in the same buffer as the protein and allowed to settle for 30 min. An aliquot of 200 µL of the *M. lysodeikticus* suspension was added to 20 µL of lysozyme at 0.05 mg·mL^{-1} in a 96-well plate at 298.15 K. The measurements of absorbance at 450 nm started immediately after substrate addition and were then monitored at 30 s intervals for 5 min, using a microplate reader. Blank assays were prepared as described for the samples but without the addition of lysozyme to check for possible autohydrolysis of the substrate (*M. lysodeikticus* only) and to assess the "free" ILs absorbance at 450 nm. Each measurement was done in duplicate. The average values of A_{450} at each time point were plotted against time (s) and the period of linear turbidity decline (slope) was used to calculate the enzyme activity. 1 unit is equivalent to a decrease of absorbance of 0.001/min, so unit/mg = (ΔA_{450}/min x 10^3) / mg of lysozyme in the reaction

mixture. The relative activity is then obtained considering the activity of lysozyme free of ILs as 100%.

3.4 Circular dichroism

CD spectra were obtained on a JASCO J-815 spectropolarimeter at 293.15 K using a quartz cuvette with 0.1 cm path length. Due to technical restrictions of the CD equipment, it was only possible to record spectra at wavelengths above 205 nm, so the range used was 205 to 260 nm. All samples were prepared in water (bidistilled and sterilized by filtration through 0.2 μm Millipore filter) to final concentrations of 0.2 mg·mL^{-1} for lysozyme and 0.6% v/v and 1.2% v/v for ionic liquids. The studied samples were incubated at room temperature for at least 30 min prior to CD experiments. Spectra were acquired with 4 accumulations at scan speeds of 50 nm/min and a response time of 1 s. Two replicates were measured and merged for each CD spectrum, which is displayed in millidegrees. Spectral deconvolution was done with K2D3[56] to estimate the secondary structure of lysozyme in the absence and presence of ILs.

3.5 Dynamic Light Scattering

Measurements were performed on a Zetasizer Nano Series ZEN3600 (Malvern Instruments, UK) apparatus equipped with a 633 nm laser. A non-invasive back-scattering technique (173°) was used for detection. A 4 mg·mL^{-1} stock solution of lysozyme was prepared in 66 mM potassium phosphate buffer with a pH of 6.2 and ionic liquid solutions were dissolved in Milli-Q water to 1 and 10% v/v concentrations. All the solutions were filtered with Millex PVDF filters of 0.22 μm pore diameter prior to use. Lysozyme and ILs were mixed, and the volume adjusted with buffer, so the final concentrations are 0.2 mg·mL^{-1} for the protein and 0 to 1.2% v/v for the ILs and allowed to equilibrate for approximately 24 h at room temperature with mild shaking. A 30 μL-aliquot of each sample was loaded into a Hellma Quartz Cell QS 3.00 mm and measured 3 times and the cell temperature was kept constant at 298.15 K.

3.6 Microscopy studies

Transmission electron microscopy (TEM) was performed in a Hitachi 8100 model with LaB6 filament, at a working voltage of 200 kV. Solutions of lysozyme (prepared in 66 mM potassium phosphate buffer with a pH of 6.2), fluorinated ionic liquid (1.2% *v/v* in buffer) and lysozyme with fluorinated ionic liquid 1.2% *v/v* were placed on a 200 mesh copper grid (3 mm diameter). The excess of sample was removed using filter paper and samples were dried before measurements. Scanning electron microscopy (SEM) analyses were performed in a Hitachi S2400 with Bruker light elements EDS detector at a working voltage of 10 kV. All grids were imaged at MicroLab-IST (Lisbon, Portugal).

4. Results and Discussion

4.1 Stability and function of lysozyme

The FILs herein studied, combining different cations with fluorinated anions, were selected because they are miscible in water with improved surfactant properties and low cytotoxicity levels in human cells. Two non-surfactant ionic liquids based on the cholinium cation, $[N_{1112(OH)}][H_2PO_4]$ and $[N_{1112(OH)}][CF_3SO_3]$ (see Table 2.1), were also chosen to compare their behaviour with that of the neoteric FILs. $[N_{1112(OH)}][H_2PO_4]$ was used as a biocompatible ionic liquid for biological applications [6,46,49] and $[N_{1112(OH)}][CF_3SO_3]$ is a conventional fluoro-containing IL useful to compare with the novel surfactants FILs selected in this work. The behaviour of ILs was evaluated in a range of concentrations (0 to 1.2% *v/v*) below and above the *CAC* (~ 0.6% *v/v*, Table 2.1). Concentrations of FILs higher than the *CAC* were used to allow for self-assembling of micellar structures. As the FIL micelles may encapsulate the protein, we have examined the impact of this encapsulation on several protein features, the first step towards DDS.

Experimental data from DSF and activity assays were analysed with GraphPad Prism, 7.0 (GraphPad Software, San Diego, USA) statistical software using one-way ANOVA followed by Dunnet test, when appropriate. Mean values were calculated for the
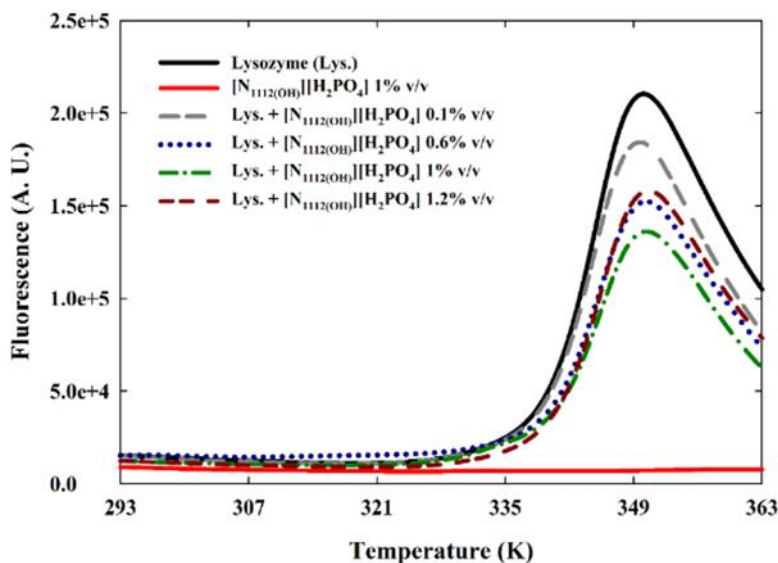
Figure 2.1. Melting temperature of lysozyme (0.2 mg·mL^{-1} in buffer) in the presence of $[N_{1112(OH)}][H_2PO_4]$ at different concentrations, dissolved in 66 mM potassium phosphate at pH 6.2, and T = 298.15 K.

different experiments with their respective standard deviation. The differences were considered significant when $p < 0.005$.

Differential Scanning Fluorimetry (DSF) was used to determine the melting temperature (T_m) of lysozyme, at which both the folded and unfolded states coexist at equilibrium. Upon protein unfolding, the exposed hydrophobic surfaces bind the SYPRO Orange dye, resulting in an increase in fluorescence by excluding water. Thus, the conformational stability of lysozyme at 0.2 mg·mL^{-1} upon the addition of ILs (0 to 1.2%) was monitored by this thermal shift assay. Both protein and IL samples were dissolved in 0.1 M KH$_2$PO$_4$/K$_2$HPO$_4$, pH 7. Controls using only ILs with SYPRO Orange dye show only fluorescence at residual values that remained constant with temperature, demonstrating that ILs are not interfering with the determination of the T_m values. Figure 2.1 illustrates the fluorescence curves of the DSF assays for lysozyme with [N$_{1112(OH)}$][H$_2$PO$_4$].

The melting temperature of lysozyme in the presence of various ILs at different concentrations is depicted in Figure 2.2, and T_m values can be found in Table 2.2. The T_m of lysozyme under the studied conditions was around 351 K, a value that is in agreement with other reports [57]. The ILs based on the cholinium cation show the least impact on lysozyme T_m, especially [N$_{1112(OH)}$][H$_2$PO$_4$] and [N$_{1112(OH)}$][CF$_3$SO$_3$], which are non-surfactant ILs. [N$_{1112(OH)}$][CF$_3$SO$_3$] causes only a negligible decrease on the protein melting temperature (to 348 K) at the highest concentration. The most pronounced effect is observed when [C$_2$C$_1$py][C$_4$F$_9$CO$_2$] at 1.2% *v/v* is added to the protein. However, the decrease of the protein
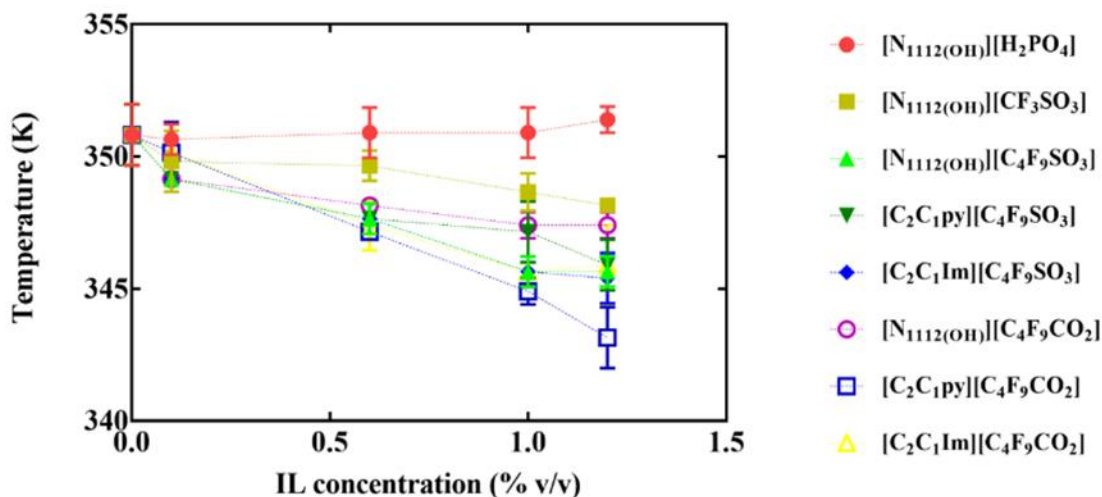
Figure 2.2. Melting temperature of lysozyme (0.2 mg·mL-1) with ionic liquids at different concentrations in 0.1 M potassium phosphate, pH 7, determined by DSF. The error bars indicate the standard deviations around the mean values.

melting temperature is only 2% (to 343 K). Interestingly, these small shifts are not reflected on the functional assays of lysozyme (see below) and may be due to some local conformational changes that do not directly affect the substrate binding site. Therefore, this DSF study shows that the stability of lysozyme is not considerably affected by the surfactant FILs.

Table 2.2. Melting temperature (T_m, K) of lysozyme (0.2 mg·mL^{-1} in buffer) measured by differential scanning fluorimetry

Ionic Liquid	Concentration (% in *v/v*)				
	0	0.1	0.6	1	1.2
$[N_{1112(OH)}][H_2PO_4]$		350.6 ± 0.6	350.9 ± 1.0	350.9 ± 1.0	351.4 ± 0.5
$[N_{1112(OH)}][CF_3SO_3]$		349.8 ± 1.2	349.6 ± 0.6	348.6 ± 0.7	348.1 ± 0.0*
$[N_{1112(OH)}][C_4F_9SO_3]$		349.1 ± 0.0	347.6 ± 0.6*	345.6 ± 0.6*	345.6 ± 0.6*
$[C_2C_1py][C_4F_9SO_3]$	350.8 ± 1.2	349.1 ± 0.0	347.6 ± 0.6*	347.1 ± 1.2*	345.9 ± 1.0*
$[C_2C_1Im][C_4F_9SO_3]$		349.1 ± 0.0	347.6 ± 0.6*	345.6 ± 0.6*	345.4 ± 1.0*
$[N_{1112(OH)}][C_4F_9CO_2]$		349.1 ± 0.0*	348.1 ± 0.0*	347.4 ± 0.5*	347.1 ± 0.5*
$[C_2C_1py][C_4F_9CO_2]$		350.1 ± 1.2	347.1 ± 0.0*	344.9 ± 0.5*	343.1 ± 1.2*
$[C_2C_1Im][C_4F_9CO_2]$		350.1 ± 0.0	347.4 ± 1.0*	345.6 ± 0.6*	345.9 ± 1.5*

Mean values were obtained from duplicates of two independent measurements with their standard deviations * significance when p < 0.005. (n=4, Dunnet test).

Lysozyme catalyses the hydrolysis of β-1,4-glucosidic linkages between *N*-acetylglucosamine and *N*-acetylmuramic acid. The muramidase activity of lysozyme was followed spectrophotometrically by measuring the absorbance decrease at 450 nm, which reflects the hydrolysis of the *M. lysodeikticus* cell wall by the enzyme. This activity depends on several parameters, such as pH and temperature [55,58], so we selected pH 6.2 (optimal value) and T = 298.15 K to perform the functional experiments and study the influence of ILs in the activity of lysozyme.

The A_{450} measurements from the substrate blank were similar along time, meaning that *M. lysodeikticus* is not auto hydrolysed, so these values were considered negligible when calculating the enzymatic activity. The various ILs blanks present A_{450} values between ~0.1 and 0.3 that remained constant along time and caused no interference on the initial absorbance measured immediately after substrate addition, which is around 0.8, regardless

of the IL mixed with lysozyme. Figure 2.3 displays the A_{450} variance upon substrate addition to lysozyme in the presence of two ILs for 5 minutes. The activity of lysozyme was calculated from the slope of the time course, in which the turbidity decline is considered linear (at 120 s). The linear regression of the data points using GraphPad Prism software for the different experiments yielded R^2 values between 0.9809 and 0.9945. A unit of enzyme corresponds to the quantity of enzyme that causes a decrease in the absorbance of 0.001/min (under our set of specified conditions at pH 6.2 (66 mM potassium phosphate and $T = 298.15$ K). We
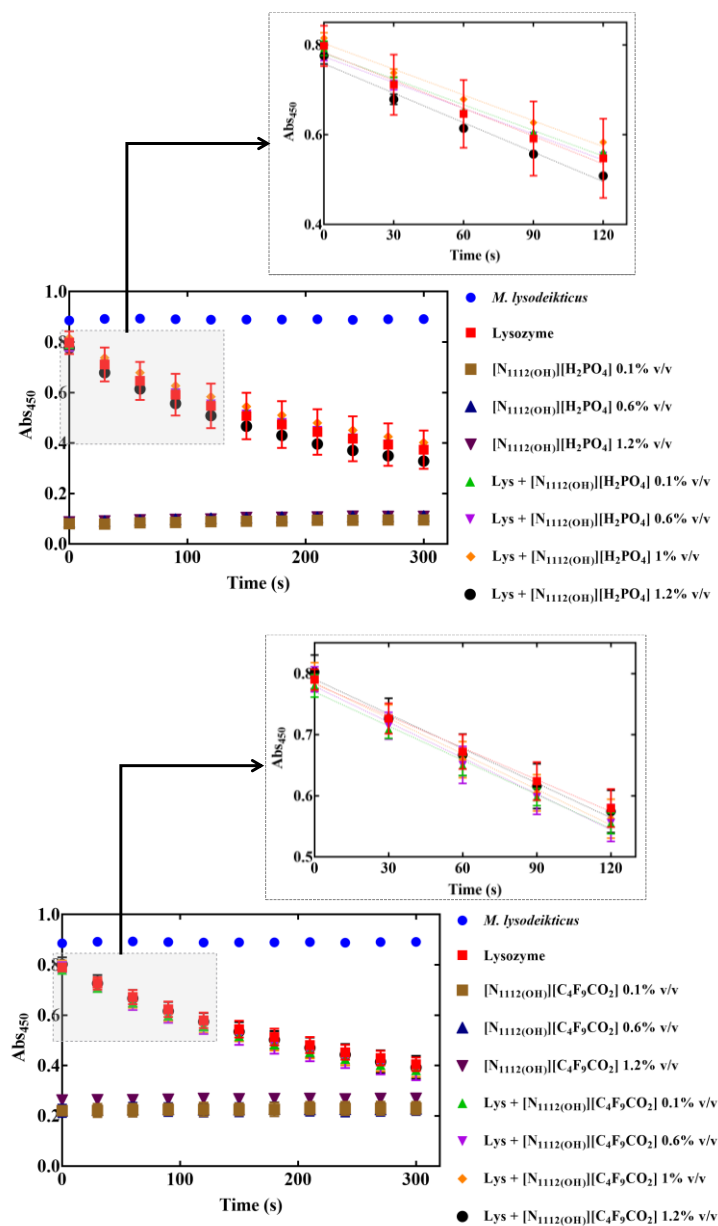
Figure 2.3. Absorbance measurements at 450 nm for lysozyme (0.2 mg·mL^{-1} in buffer) activity assays with [N$_{1112(OH)}$][H$_2$PO$_4$] *(top)*; and [N$_{1112(OH)}$][C$_4$F$_9$CO$_2$] *(bottom)* at different concentrations in buffer. Linear regression coefficients for the different data set vary between 0.9809 and 0.9945.

herein obtained a value around 98×10^3 U/mg for the activity of lysozyme (in the absence of ILs), which is comparable with other studies [54,55]. This activity is considered to be 100% and the other activities (lysozyme plus ILs) are reported relative to this one (Figure 2.4 and Table 2.3). These functional studies show that the activity of lysozyme is not significantly affected by the presence of ILs. Indeed, the addition of surfactant ILs promotes a slight increase in the enzymatic activity, where $[C_2C_1Im][C_4F_9SO_3]$ is responsible for the most pronounced effect, up to 20%, followed by $[C_2C_1py][C_4F_9CO_2]$.
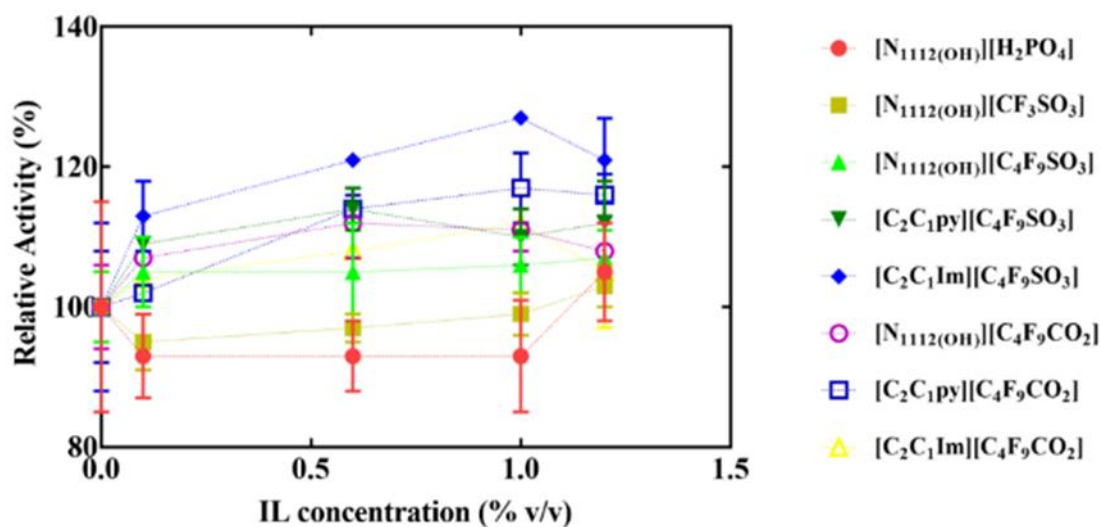
Figure 2.4. Relative activity of lysozyme (0.2 mg·mL^{-1} during the incubation time) with ionic liquids at different concentrations in 66 mM potassium phosphate, pH 6.2 and $T = 298.15$ K. Absorbance measurements were repeated two times in a microplate. The error bars indicate the standard deviations around the mean values.

4.2 Structural studies

Circular dichroism (CD) spectroscopy is useful to rapidly examine the secondary structure and folding properties of proteins since different structural elements have characteristic CD spectra [59]. CD spectra were recorded between 205 and 260 nm (Figure 2.5) and analysed with the program K2D3 [56] to estimate the secondary structure of lysozyme upon addition of ionic liquids (see Table 2.4). Noteworthy, CD spectra for ILs containing either imidazolium or pyridinium as cation groups could not be recorded due to their high intensity signals (HT voltage rising above 600 V for IL at 0.1% *v/v*). Therefore, CD measurements were carried out only for cholinium derived-ILs. The secondary structure predictions obtained herein for lysozyme, of 28.5% α-helix and 19.8% of β-strand, are in

Table 2.3. Relative activity (in percentage) of lysozyme (0.2 mg·mL-1 in buffer during the incubation time) as a function of the ILs concentration.

Ionic Liquid	Concentration (% in *v/v*)				
	0	0.1	0.6	1	1.2
$[N_{1112(OH)}][H_2PO_4]$	100 ± 15	93 ± 6	93 ± 5	93 ± 8	105 ± 7
$[N_{1112(OH)}][CF_3SO_3]$	100 ± 15	95 ± 4	97 ± 2	99 ± 3	103 ± 3
$[N_{1112(OH)}][C_4F_9SO_3]$	100 ± 5	105 ± 5	105 ± 7	106 ± 4	107 ± 4
$[C_2C_1py][C_4F_9SO_3]$	100 ± 1	109 ± 1	114 ± 3*	110 ± 4	112 ± 6*
$[C_2C_1Im][C_4F_9SO_3]$	100 ± 12	113 ± 5	121 ± 0	127 ± 1	121 ± 6
$[N_{1112(OH)}][C_4F_9CO_2]$	100 ± 6	107 ± 0	112 ± 5	111 ± 3	108 ± 4
$[C_2C_1py][C_4F_9CO_2]$	100 ± 8	102 ± 1	114 ± 2	117 ± 5*	116 ± 3
$[C_2C_1Im][C_4F_9CO_2]$	100 ± 5	104 ± 1	108 ± 0	112 ± 4	105 ± 8

Mean values were obtained from duplicates of two independent measurements with their standard deviations * significance when $p < 0.005$. (n=4, Dunnet test).

good agreement with the analysis based on various methods and yielding values of approximately 30% and 19%, respectively, by Greenfield [59]. The estimated structural content for lysozyme on IL addition is slightly higher for helical elements and lower for β-strands (see Table 2.4). However, pairwise comparison of CD spectra with the different ionic
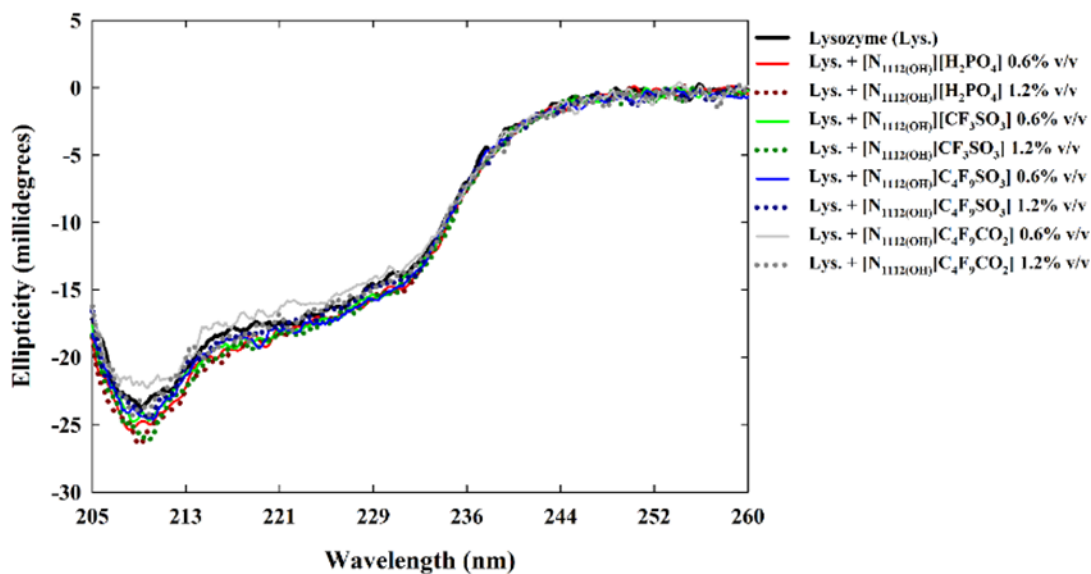
Figure 2.5. CD spectra of lysozyme (0.2 mg·mL-1) with ionic liquids at different concentrations in water at 293.15 K, measured on a JASCO J-815 spectropolarimeter.

liquids (protein-IL at 0.6/1.2% *v/v*) shows no substantial alteration on the predicted values for both non-surfactant ILs as well as for [$N_{1112(OH)}$][$C_4F_9SO_3$] (Figure 2.5). In contrast, the CD spectra of [$N_{1112(OH)}$][$C_4F_9CO_2$] seem noisier than the others. In addition, the differences in the estimated secondary structure between the duplicated experiments may be due to errors inherent to the protein concentration. Therefore, these CD results suggest no substantial protein structural modification upon IL addition at concentrations below and above the *CAC*.

Table 2.4. Secondary structure prediction of lysozyme (0.2 mg·mL^{-1} in water) using K2D3.

	α-helix content (%)	β-strand content (%)
Lysozyme (Lys)	28.5	19.8
Lys + [$N_{1112(OH)}$][H_2PO_4] 0.6 % *v/v*	30.3	18.6
Lys + [$N_{1112(OH)}$][H_2PO_4] 1.2 % *v/v*	31.3	18.2
Lys + [$N_{1112(OH)}$][CF_3SO_3] 0.6 % *v/v*	31.0	18.8
Lys + [$N_{1112(OH)}$][CF_3SO_3] 1.2 % *v/v*	31.4	18.3
Lys + [$N_{1112(OH)}$][$C_4F_9SO_3$] 0.6 % *v/v*	31.0	18.8
Lys + [$N_{1112(OH)}$][$C_4F_9SO_3$] 1.2 % *v/v*	30.0	19.4
Lys + [$N_{1112(OH)}$][$C_4F_9CO_2$] 0.6 % *v/v*	27.5	20.4
Lys + [$N_{1112(OH)}$][$C_4F_9CO_2$] 1.2 % *v/v*	29.6	19.7

Mean values were calculated from 2 replicates with their respective standard deviations

4.2 Aggregation behaviour

In the previous sections, it was possible to prove that FILs do not interfere with either stability, activity or structure of lysozyme. The next step to evaluate if FILs can be used in DDS, requires the characterization of the aggregates composed of FILs and lysozyme. Lysozyme, which is a relatively small globular protein consisting of 129 amino acid residues with approximate dimensions of 45 Å x 31 Å x 30 Å, was used to probe the notorious ability of FILs to encapsulate biomolecules. The encapsulation is facilitated by the incorporation of fluorinated chains in the IL, which improves the self-assembly behaviour at lower

concentrations [30], making them better candidates for DDS than traditional fluorosurfactants [28,46].

Dynamic light scattering (DLS) is a common and powerful tool used to assess the size of aggregated structures in solutions. Due to its non-invasive nature, this technique is commonly used in the field of nanoparticle design for biomedical purposes [60,61]. Self-assembled structures of different ionic liquids in solution with lysozyme were analysed in a concentration range from 0 to 1.2% *v/v*. Our aim is to examine whether lysozyme is being encapsulated inside the aggregates of the most promising FILs, according to the previous assays. These studies were performed with IL concentration of up to 1.2% *v/v* since this concentration corresponds to two times that of the *CAC* (see Table 2.1). All samples were dissolved in 66 mM potassium phosphate at pH 6.2. Blank samples of lysozyme and pure ionic liquids (1.2% *v/v*) in buffer were also measured to obtain the characteristic hydrodynamic diameters of these compounds. For pure lysozyme, a characteristic broad peak is observed between 4-5 nm [62] indicating some polydispersion in the protein solutions, while pure ionic liquids do not exhibit any aggregates in this range, as shown in Figure 2.6. These compounds only show peaks at higher diameter ranges (100-1000 nm).

In these DLS experiments, it is possible to compare distinct classes of ILs (Figure 2.6), e.g., the $[N_{1112(OH)}]^+$ cation conjugated with a non-surfactant anion, $[CF_3SO_3]^-$, or a surfactant one, $[C_4F_9SO_3]^-$. In Figure 2.6a one can identify the characteristic peak of lysozyme (diameter ~4 nm) in all solutions. This result shows that the non-surfactant IL, $[N_{1112(OH)}][CF_3SO_3]$, is not encapsulating the protein (even at higher IL concentrations). Moreover, the identification of lysozyme aggregates is possible because the protein remains in solution without being surrounded by the ILs micelles. DLS spectra obtained using surfactant fluorinated ionic liquids, $[N_{1112(OH)}][C_4F_9SO_3]$ (Figure 2.6b) or $[C_2C_1Im][C_4F_9SO_3]$ (Figure 2.6c), show a decrease in the intensity peak of lysozyme (diameter ~4 nm) with the addition of FIL and its disappearance at 1.2% *v/v* FIL, with the concomitant appearance of a higher intensity peak at hydrodynamic diameters around 1000 nm. These results suggest the encapsulation of lysozyme by these surfactant FILs at concentrations above the *CAC*.

Finally, two different electron microscopy studies (TEM and SEM) were performed to compare the morphology and size of different aggregates. These studies provide images at higher resolution than optical microscopes and allow us to confirm whether lysozyme could be encapsulated by these surfactants. TEM and SEM images were acquired for: i)
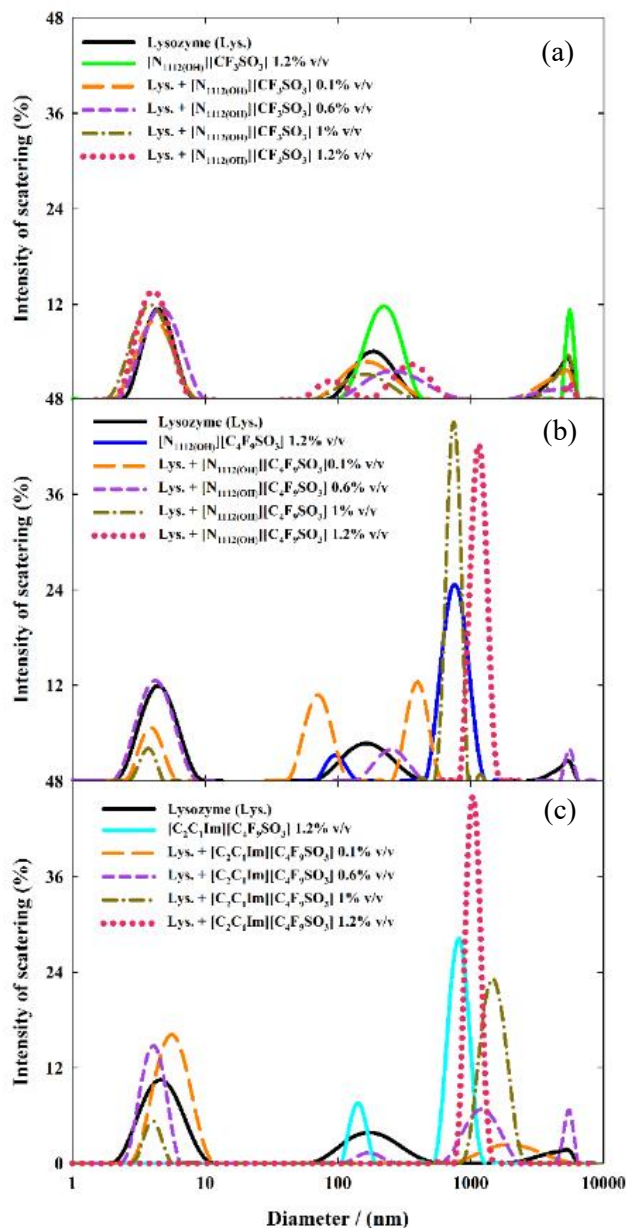
Figure 2.6. DLS spectra of lysozyme (0.2 mg·mL-1) in 66 mM potassium phosphate, pH 6.2 upon the addition of several ILs in water: (a) $[N_{1112(OH)}][CF_3SO_3]$; (b) $[N_{1112(OH)}][C_4F_9SO_3]$; and (c) $[C_2C_1Im][C_4F_9SO_3]$ at 298.15 K.

pure lysozyme (0.2 mg·mL^{-1}) in 66 mM potassium phosphate with a pH of 6.2; ii) pure ionic liquid $[C_2C_1Im][C_4F_9SO_3]$ in phosphate buffer at a concentration of 1.2% *v/v* (two times that of the *CAC*); and iii) a mixture of both lysozyme and IL at the above concentrations in the same buffer.

Figure 2.7 depicts transmission electron microscopy images for the three samples herein studied. TEM images of lysozyme (Figure 2.7a) show larger lighter grey shades

circles than those observed for $[C_2C_1Im][C_4F_9SO_3]$ (Figure 2.7b), while the mixture of the protein with the IL at 1.2% *v/v* displays circles with a darker contour at the exterior of the aggregates (Figure 2.7c). In TEM, the areas comprising heavier atoms (with larger atomic number and more powerful scattering centres) will appear darker than those containing lighter atoms.[63] Thus, the comparison between TEM images of the different solutions suggests the encapsulation of lysozyme (light grey) inside the micelles of $[C_2C_1Im][C_4F_9SO_3]$, with the presence of the IL anion in the external part of the structures (darker grey). Besides, the micelle sizes obtained by TEM are in accordance with the hydration diameters of these solutions measured by DLS. TEM images show well separated aggregates of pure FIL in buffer with diameters around 200-400 nm (see Figure 2.7b). Remarkably, TEM images for the same FIL, $[C_2C_1Im][C_4F_9SO_3]$, using Milli-Q water as dispersant, show that the micelles form aggregates with an average hydrodynamic diameter of 184 nm.[30] These results suggest that the nature of the dispersant plays an important role in the stabilization of the self-assembled structures. The size of micelles increases significantly in the presence of the buffer.
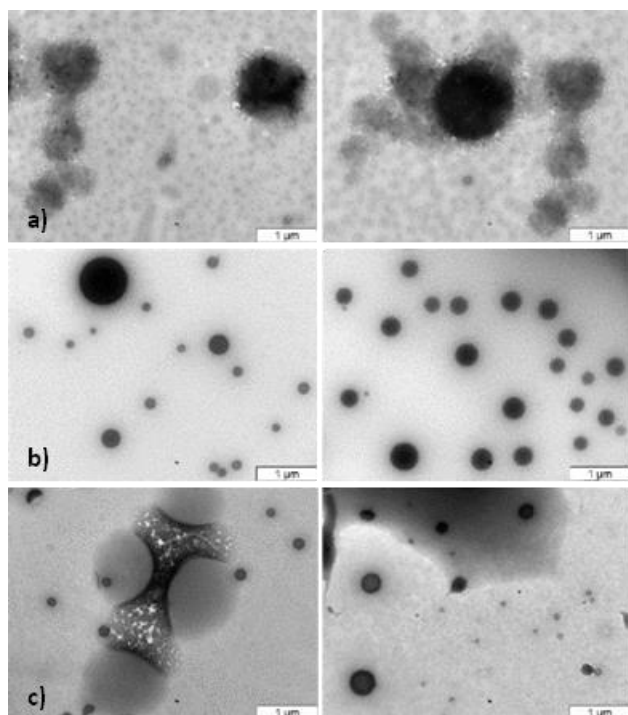
Figure 2.7. TEM images of: (a) lysozyme aggregates (0.2 mg·mL-1); (b) $[C_2C_1Im][C_4F_9SO_3]$ 1.2% *v/v*; and (c) 1.2% *v/v* of $[C_2C_1Im][C_4F_9SO_3]$ with lysozyme (0.2 mg·mL-1). All samples were prepared in 66 mM potassium phosphate, pH 6.2 and T = 298.15 K. The scale bar corresponds to 1 μm.

SEM images provide insights into the surface structure of each sample. In Figure 2.8, spherical particles of different sizes with a pale contour are observed for lysozyme (Figure 2.8a) and a rough surface for $[C_2C_1Im][C_4F_9SO_3]$ (Figure 2.8b). Interestingly, it was also possible to observe a granular aspect for the mixture of lysozyme with FIL at 1.2% *v/v* (Figure 2.8b), more similar to the structures formed by the fluorinated ionic liquid in buffer (Figure 2.8c). The aspect of both SEM and TEM images of FIL mixed with lysozyme are more alike pure $[C_2C_1Im][C_4F_9SO_3]$ in buffer (than the protein "alone"). Therefore, these electron microscopy results confirm those obtained by DLS suggesting the encapsulation of lysozyme inside the micelles of FILs-based surfactants at concentrations above the *CAC*.
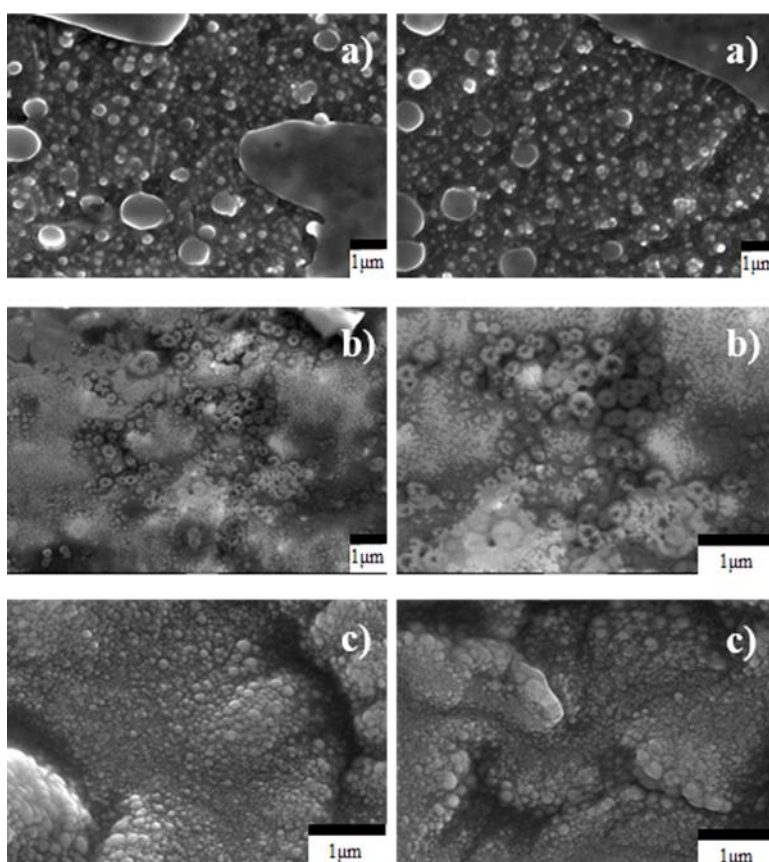
Figure 2.8. SEM images of: (a) lysozyme (0.2 mg·mL-1); (b) $[C_2C_1Im][C_4F_9SO_3]$ 1.2% *v/v* and (c) 1.2% *v/v* of $[C_2C_1Im][C_4F_9SO_3]$ with lysozyme in buffer (0.2 mg·mL-1). All samples were prepared in 66 mM potassium phosphate, pH 6.2 and T = 298.15 K. The scale bar corresponds to 1μm.

5. Conclusions

A diversity of proteins, *e.g.* insulin, coagulation factors, interferons and antibodies are currently available for pharmaceutical use to treat a wide range of diseases, such as diabetes, haemophilia, multiple sclerosis and cancers. This work aims to evaluate the possible application of surfactants based on fluorinated ionic liquids in drug delivery systems of therapeutic proteins. Hence, lysozyme was used as a model protein for these initial studies because it is a well-characterized protein which is commercially available and shows antimicrobial properties. The comparison between non-surfactant ionic liquids (cholinium dihydrogen phosphate and cholinium trifluoromethanesulfonate) and surfactant FILs corroborates the encapsulation of lysozyme using these surfactant FILs at concentrations above the *CAC*.

Novel and nontoxic FILs that are totally miscible in water and with improved surfactant behaviour were used. The evaluation of the conditions and structures where lysozyme maintains or improves its activity and stability were performed using various techniques that may be applied to other proteins. These studies have proven that both the stability and activity of lysozyme are not affected by the incorporation of surfactant FILs. Lysozyme encapsulation by ionic liquids did not decrease its hydrolytic performance, contrary to our expectations (as the enzyme inside a micelle is anticipated to be less accessible towards the external medium). Further studies are necessary to elucidate the permeability of protein-IL-micelle aggregates.

The encapsulation and stability of the potential drug delivery systems herein studied were also proved using dynamic light scattering (DLS) and scanning and transmission electron microscopy (SEM/TEM) supporting the ability of fluorinated ionic liquids to be used as drug delivery systems of therapeutic proteins. Further studies are needed to better characterize the micellar structure formed upon mixture of protein and ILs. However, these results constitute a first step towards the biomedical application of these specific ionic liquids. The encapsulation and stabilization of therapeutic proteins using FILs might overcome some of the actual issues involving the delivery of these drugs in the human body by improving their bioavailability, stability, structure, and efficacy. Novel drug delivery systems based on FILs may increase the efficiency of therapeutic proteins by incorporating protection while decreasing their immunogenicity.

6. References

1.   Dimitrov, D.S. Therapeutic proteins. *Methods Mol. Biol.* **2012**, *899*, 1–26, doi:10.1007/978-1-61779-921-1_1.

2.   Ibraheem, D.; Elaissari, A.; Fessi, H. Administration strategies for proteins and peptides. *Int. J. Pharm.* **2014**, *477*, 578–589, doi:10.1016/j.ijpharm.2014.10.059.

3.   Brasnjevic, I.; Steinbusch, H.W.M.M.; Schmitz, C.; Martinez-Martinez, P. Delivery of peptide and protein drugs over the blood-brain barrier. *Prog. Neurobiol.* **2009**, *87*, 212–251, doi:10.1016/j.pneurobio.2008.12.002.

4.   Leader, B.; Baca, Q.J.; Golan, D.E. Protein therapeutics: a summary and pharmacological classification. *Nat. Rev. Drug Discov.* **2008**, *7*, 21–39, doi:10.1038/nrd2399.

5.   Dai, C.; Wang, B.; Zhao, H. Microencapsulation peptide and protein drugs delivery system. *Colloids Surfaces B Biointerfaces* **2005**, *41*, 117–120, doi:10.1016/j.colsurfb.2004.10.032.

6.   Fujita, K.; MacFarlene, D.R.; Forsyth, M.; Yoshizawa-Fujita, M.; Murata, K.; Nakamura, N.; Ohno, H. Solubility and stability of cytochrome c in hydrated ionic liquids: Effect of oxo acid residues and kosmotropicity. *Biomacromolecules* **2007**, *8*, 2080–2086, doi:10.1021/bm070041o.

7.   Ohno, H.; Suzuki, C.; Fukumoto, K.; Yoshizawa, M.; Fujita, K. Electron transfer process of poly(ethylene oxide)-modified cytochrome c in imidazolium type ionic liquid. *Chem. Lett.* **2003**, *32*, 450–451, doi:10.1246/cl.2003.450.

8.   Araújo, J.M.M.; Pereiro, A.B.; Alves, F.; Marrucho, I.M.; Rebelo, L.P.N. Nucleic acid bases in 1-alkyl-3-methylimidazolium acetate ionic liquids: A thermophysical and ionic conductivity analysis. *J. Chem. Thermodyn.* **2013**, *57*, 1–8, doi:https://doi.org/10.1016/j.jct.2012.07.022.

9.   Araújo, J.M.M.; Florindo, C.; Pereiro, A.B.; Vieira, N.S.M.; Matias, A.A.; Duarte, C.M.M.; Rebelo, L.P.N.; Marrucho, I.M. Cholinium-based ionic liquids with pharmaceutically active anions. *RSC Adv.* **2014**, *4*, 28126–28132, doi:10.1039/C3RA47615D.

10. Moniruzzaman, M.; Tamura, M.; Tahara, Y.; Kamiya, N.; Goto, M. Ionic liquid-in-oil microemulsion as a potential carrier of sparingly soluble drug: characterization and cytotoxicity evaluation. *Int. J. Pharm.* **2010**, *400*, 243–250, doi:10.1016/j.ijpharm.2010.08.034.

11. Mahkam, M.; Abbaszad Rafi, A.; Mohammadzadeh Gheshlaghi, L. Preparation of novel pH-sensitive nanocomposites based on ionic-liquid modified montmorillonite for colon specific drug delivery system. *Polym. Compos.* **2016**, *37*, 182–187, doi:https://doi.org/10.1002/pc.23169.

12. Goindi, S.; Kaur, R.; Kaur, R. An ionic liquid-in-water microemulsion as a potential carrier for topical delivery of poorly water soluble drug: Development, ex-vivo and in-vivo evaluation. *Int. J. Pharm.* **2015**, *495*, 913–923, doi:10.1016/j.ijpharm.2015.09.066.

13. Wang, X.; Chen, H.; Luo, Z.; Fu, X. Preparation of starch nanoparticles in water in oil microemulsion system and their drug delivery properties. *Carbohydr. Polym.* **2016**, *138*, 192–200, doi:10.1016/j.carbpol.2015.11.006.

14. Tang, W.; Liu, B.; Wang, S.; Liu, T.; Fu, C.; Ren, X.; Tan, L.; Duan, W.; Meng, X. Doxorubicin-loaded ionic liquid–polydopamine nanoparticles for combined chemotherapy and microwave thermal therapy of cancer. *RSC Adv.* **2016**, *6*, 32434–32440, doi:10.1039/C6RA02434C.

15. Rossi, S.; Waton, G.; Krafft, M.P. Phospholipid-Coated Gas Bubble Engineering: Key Parameters for Size and Stability Control, as Determined by an Acoustical Method. *Langmuir* **2010**, *26*, 1649–1655, doi:10.1021/la9025987.

16. Schutt, E.G.; Klein, D.H.; Mattrey, R.M.; Riess, J.G. Injectable microbubbles as contrast agents for diagnostic ultrasound imaging: the key role of perfluorochemicals. *Angew. Chem. Int. Ed. Engl.* **2003**, *42*, 3218–3235, doi:10.1002/anie.200200550.

17. Stride, E.; Edirisinghe, M. Special issue on microbubbles: from contrast enhancement to cancer therapy. *Med. Biol. Eng. Comput.* **2009**, *47*, 809–811, doi:10.1007/s11517-009-0510-8.

18. Krafft, M.-P.; Riess, J.G. Stable Highly Concentrated Fluorocarbon Gels. *Angew. Chemie Int. Ed. English* **1994**, *33*, 1100–1101, doi:https://doi.org/10.1002/anie.199411001.

19. Krafft, M.P. Highly fluorinated compounds induce phase separation in, and nanostructuration of liquid media. Possible impact on, and use in chemical reactivity control. *J. Polym. Sci. Part A Polym. Chem.* **2006**, *44*, 4251–4258, doi:https://doi.org/10.1002/pola.21508.

20. Bertilla, S.M.; Thomas, J.-L.; Marie, P.; Krafft, M.P. Cosurfactant effect of a semifluorinated alkane at a fluorocarbon/water interface: impact on the stabilization of fluorocarbon-in-water emulsions. *Langmuir* **2004**, *20*, 3920–3924, doi:10.1021/la036381m.

21. Garnett, M.C.; Stolnik, S.; Dunn, S.E.; Armstrong, I.; Lin, W.; Schacht, E.; Ferutti, P.; Vert, M.; Davies, M.C.; Illum, L.; et al. Application of Novel Biomaterials in Colloidal Drug Delivery Systems. *MRS Bull.* **1999**, *24*, 49–56, doi:DOI: 10.1557/S0883769400052325.

22. Courrier, H.M.; Vandamme, T.F.; Krafft, M.P. Reverse water-in-fluorocarbon emulsions and microemulsions obtained with a fluorinated surfactant. *Colloids Surfaces A Physicochem. Eng. Asp.* **2004**, *244*, 141–148, doi:10.1016/j.colsurfa.2004.06.003.

23. Riess, J.G. Oxygen Carriers ("Blood Substitutes")Raison d'Etre, Chemistry, and Some Physiology Blut ist ein ganz besondrer Saft. *Chem. Rev.* **2001**, *101*, 2797–2920, doi:10.1021/cr970143c.

24. Riess, J.G. Understanding the fundamentals of perfluorocarbons and perfluorocarbon emulsions relevant to in vivo oxygen delivery. *Artif. Cells. Blood Substit. Immobil. Biotechnol.* **2005**, *33*, 47–63, doi:10.1081/bio-200046659.

25. Riess, J.G. Perfluorocarbon-based oxygen delivery. *Artif. Cells. Blood Substit. Immobil. Biotechnol.* **2006**, *34*, 567–580, doi:10.1080/10731190600973824.

26. Krafft, M.P.; Riess, J.G. Highly fluorinated amphiphiles and colloidal systems, and their applications in the biomedical field. A contribution. *Biochimie* **1998**, *80*, 489–514, doi:10.1016/s0300-9084(00)80016-4.

27. Tan, M.L.; Choong, P.F.M.; Dass, C.R. Recent developments in liposomes, microparticles and nanoparticles for protein and peptide drug delivery. *Peptides* **2010**, *31*, 184–193, doi:10.1016/j.peptides.2009.10.002.

28. Salwiczek, M.; Nyakatura, E.K.; Gerling, U.I.M.; Ye, S.; Koksch, B. Fluorinated amino acids: compatibility with native protein structures and effects on protein–protein interactions. *Chem. Soc. Rev.* **2012**, *41*, 2135–2171, doi:10.1039/C1CS15241F.

29. Pereiro, A.B.; Pastoriza-Gallego, M.J.; Shimizu, K.; Marrucho, I.M.; Lopes, J.N.C.; Piñeiro, M.M.; Rebelo, L.P.N. On the Formation of a Third, Nanostructured Domain in Ionic Liquids. *J. Phys. Chem. B* **2013**, *117*, 10826–10833, doi:10.1021/jp402300c.

30. Pereiro, A.B.; Araújo, J.M.M.; Teixeira, F.S.; Marrucho, I.M.; Piñeiro, M.M.; Rebelo, L.P.N. Aggregation behavior and total miscibility of fluorinated ionic liquids in water. *Langmuir* **2015**, *31*, 1283–1295, doi:10.1021/la503961h.

31. Pereiro, A.B.; Araújo, J.M.M.; Martinho, S.; Alves, F.; Nunes, S.; Matias, A.; Duarte, C.M.M.; Rebelo, L.P.N.; Marrucho, I.M. Fluorinated ionic liquids: Properties and applications. *ACS Sustain. Chem. Eng.* **2013**, *1*, 427–439, doi:10.1021/sc300163n.

32. Vieira, N.S.M.; Bastos, J.C.; Hermida-Merino, C.; Pastoriza-Gallego, M.J.; Rebelo, L.P.N.; Piñeiro, M.M.; Araújo, J.M.M.; Pereiro, A.B. Aggregation and phase equilibria of fluorinated ionic liquids. *J. Mol. Liq.* **2019**, *285*, 386–396, doi:10.1016/j.molliq.2019.04.086.

33. Oldham, E.D.; Xie, W.; Farnoud, A.M.; Fiegel, J.; Lehmler, H.-J. Disruption of phosphatidylcholine monolayers and bilayers by perfluorobutane sulfonate. *J. Phys. Chem. B* **2012**, *116*, 9999–10007, doi:10.1021/jp304412p.

34. Lindstrom, A.B.; Strynar, M.J.; Libelo, E.L. Polyfluorinated Compounds: Past, Present, and Future. *Environ. Sci. Technol.* **2011**, *45*, 7954–7961, doi:10.1021/es2011622.

35. Newsted, J.L.; Beach, S.A.; Gallagher, S.P.; Giesy, J.P. Acute and chronic effects of perfluorobutane sulfonate (PFBS) on the mallard and northern bobwhite quail. *Arch.*

Environ. Contam. Toxicol. **2008**, *54*, 535–545, doi:10.1007/s00244-007-9039-8.

36. Szajdzinska-Pietek, E.; Wolszczak, M. Time-Resolved Fluorescence Quenching Study of Aqueous Solutions of Perfluorinated Surfactants with the Use of Protiated Luminophore and Quencher. *Langmuir* **2000**, *16*, 1675–1680, doi:10.1021/la990981x.

37. Wadekar, M.N.; Boekhoven, J.; Jager, W.F.; Koper, G.J.M.; Picken, S.J. Micellization Behavior of Aromatic Moiety Bearing Hybrid Fluorocarbon Sulfonate Surfactants. *Langmuir* **2012**, *28*, 3397–3402, doi:10.1021/la2047799.

38. Vieira, N.S.M.; Bastos, J.C.; Rebelo, L.P.N.; Matias, A.; Araújo, J.M.M.; Pereiro, A.B. Human cytotoxicity and octanol/water partition coefficients of fluorinated ionic liquids. *Chemosphere* **2019**, *216*, 576–586, doi:10.1016/j.chemosphere.2018.10.159.

39. Abeyrathne, E.D.N.S.; Lee, H.Y.; Ahn, D.U. Egg white proteins and their potential use in food processing or as nutraceutical and pharmaceutical agents--a review. *Poult. Sci.* **2013**, *92*, 3292–3299, doi:10.3382/ps.2013-03391.

40. Aminlari, L.; Hashemi, M.M.; Aminlari, M. Modified lysozymes as novel broad spectrum natural antimicrobial agents in foods. *J. Food Sci.* **2014**, *79*, R1077-90, doi:10.1111/1750-3841.12460.

41. Leśnierowski, G.; Cegielska-Radziejewska, R. Potential possibilities of production, modification and practical application of lysozyme. *Acta Sci. Pol. Technol. Aliment.* **2012**, *11*, 223–230.

42. Tenovuo, J. Clinical applications of antimicrobial host proteins lactoperoxidase, lysozyme and lactoferrin in xerostomia: efficacy and safety. *Oral Dis.* **2002**, *8*, 23–29, doi:10.1034/j.1601-0825.2002.1o781.x.

43. Sava, G.; Benetti, A.; Ceschia, V.; Pacor, S. Lysozyme and cancer: role of exogenous lysozyme as anticancer agent (review). *Anticancer Res.* **1989**, *9*, 583–591.

44. Sava, G. Pharmacological aspects and therapeutic applications of lysozymes. *EXS* **1996**, *75*, 433–449, doi:10.1007/978-3-0348-9225-4_22.

45. Lee-Huang, S.; Huang, P.L.; Sun, Y.; Huang, P.L.; Kung, H.F.; Blithe, D.L.; Chen, H.C. Lysozyme and RNases as anti-HIV components in beta-core preparations of human chorionic gonadotropin. *Proc. Natl. Acad. Sci. U. S. A.* **1999**, *96*, 2678–2681, doi:10.1073/pnas.96.6.2678.

46. Du, K.; Sun, J.; Song, X.; Chen, H.; Feng, W.; Ji, P. Investigation of Ionic LIquid [bmin][CF3SO3] with Lysozyme. *ACS Sustain. Chem. Eng.* **2014**, *2*, 1420–1428.

47. Kowacz, M.; Mukhopadhyay, A.; Carvalho, A.L.; Esperança, J.M.S.S.; Romão, M.J.; Rebelo, L.P.N. Hofmeister effects of ionic liquids in protein crystallization: Direct and water-mediated interactions. *CrystEngComm* **2012**, *14,* 4912, doi:10.1039/c2ce25129a.

48. Kowacz, M.; Marchel, M.; Juknaite, L.; Esperan??a, J.M.S.S.; Romao, M.J.; Carvalho, A.L.; Rebelo, L.P.N. Ionic-liquid-functionalized mineral particles for protein crystallization. *Cryst. Growth Des.* **2015**, *15,* 2994–3003, doi:10.1021/acs.cgd.5b00403.

49. Weaver, K.D.; Vrikkis, R.M.; Van Vorst, M.P.; Trullinger, J.; Vijayaraghavan, R.; Foureau, D.M.; McKillop, I.H.; MacFarlane, D.R.; Krueger, J.K.; Elliott, G.D. Structure and function of proteins in hydrated choline dihydrogen phosphate ionic liquid. *Phys. Chem. Chem. Phys.* **2012**, *14*, 790–801, doi:10.1039/C1CP22965F.

50. Takekiyo, T.; Yamazaki, K.; Yamaguchi, E.; Abe, H.; Yoshimura, Y. High Ionic Liquid Concentration-Induced Structural Change of Protein in Aqueous Solution: A Case Study of Lysozyme. *J. Phys. Chem. B* **2012**, *116,* 11092–11097, doi:10.1021/jp3057064.

51. Vrikkis, R.M.; Fraser, K.J.; Fujita, K.; Macfarlane, D.R.; Elliott, G.D. Biocompatible ionic liquids: a new approach for stabilizing proteins in liquid formulation. *J. Biomech. Eng.* **2009**, *131*, 74514, doi:10.1115/1.3156810.

52. Vieira, N.S.M.; Reis, P.M.; Shimizu, K.; Cortes, O.A.; Marrucho, I.M.; Araújo, J.M.M.; Esperança, J.M.S.S.; Lopes, J.N.C.; Pereiro, A.B.; Rebelo, L.P.N. A thermophysical and structural characterization of ionic liquids with alkyl and perfluoroalkyl side chains. *RSC Adv.* **2015**, *5*, 65337–65350, doi:10.1039/C5RA13869H.

53. Vieira, N.S.M.M.; Luís, A.; Reis, P.M.; Carvalho, P.J.; Lopes-Da-Silva, J.A.; Esperança, J.M.S.S.S.; Araújo, J.M.M.M.; Rebelo, L.P.N.N.; Freire, M.G.; Pereiro, A.B. Fluorination effects on the thermodynamic, thermophysical and surface properties of ionic liquids. *J. Chem. Thermodyn.* **2016**, *97*, 354–361, doi:10.1016/j.jct.2016.02.013.

54. Lee, Y.C.; Yang, D. Determination of lysozyme activities in a microplate format. *Anal. Biochem.* **2002**, *310*, 223–224, doi:10.1016/s0003-2697(02)00320-2.

55. Toro, T.B.; Nguyen, T.P.; Watt, T.J. An improved 96-well turbidity assay for T4 lysozyme activity. *MethodsX* **2015**, *2*, 256–262, doi:10.1016/j.mex.2015.05.004.

56. Louis-Jeune, C.; Andrade-Navarro, M.A.; Perez-Iratxeta, C. Prediction of protein secondary structure from circular dichroism using theoretically derived spectra. *Proteins* **2012**, *80,* 374–381, doi:10.1002/prot.23188.

57. Rodrigues, J. V.; Prosinecki, V.; Marrucho, I.; Rebelo, L.P.N.; Gomes, C.M. Protein stability in an ionic liquid milieu: on the use of differential scanning fluorimetry. *Phys. Chem. Chem. Phys.* **2011**, *13*, 13614–13616, doi:10.1039/c1cp21187k.

58. Shugar, D. The measurement of lysozyme activity and the ultra-violet inactivation of lysozyme. *Biochim. Biophys. Acta* **1952**, *8,* 302–309, doi:10.1016/0006-3002(52)90045-0.

59. Greenfield, N.J. Using circular dichroism spectra to estimate protein secondary

structure. *Nat. Protoc.* **2006**, *1*, 2876–2890, doi:10.1038/nprot.2006.202.

60. Aleandri, S.; Bandera, D.; Mezzenga, R.; Landau, E.M. Biotinylated Cubosomes: A Versatile Tool for Active Targeting and Codelivery of Paclitaxel and a Fluorescein-Based Lipid Dye. *Langmuir* **2015**, *31*, 12770–12776, doi:10.1021/acs.langmuir.5b03469.

61. Singh, I.; Swami, R.; Pooja, D.; Jeengar, M.K.; Khan, W.; Sistla, R. Lactoferrin bioconjugated solid lipid nanoparticles: a new drug delivery system for potential brain targeting. *J. Drug Target.* **2016**, *24*, 212–223, doi:10.3109/1061186X.2015.1068320.

62. Parmar, A.S.; Muschol, M. Hydration and hydrodynamic interactions of lysozyme: effects of chaotropic versus kosmotropic ions. *Biophys. J.* **2009**, *97*, 590–598, doi:10.1016/j.bpj.2009.04.045.

63. Krumeich, F. Properties of Electrons, their Interactions with Matter and Applications in Electron Microscopy. *ETH Zurich* **2015**, 1–24.

CHAPTER III

Insights into the interaction of Bovine Serum Albumin with Surface-Active Ionic Liquids

MMS Alves contribution to the work described in this chapter: MMS Alves performed the experiments, analysed the data, and wrote the manuscript.

This chapter contains published data:

Alves, M.M.S.; Araújo, J.M.M.; Martins, I.C.; Pereiro, A.B.; Archer, M. Insights into the interaction of Bovine Serum Albumin with Surface-Active Ionic Liquids in aqueous solution. *J. Mol. Liq.* **2021**, *322*, 114537, doi:10.1016/j.molliq.2020.114537.

1. Abstract

The unique physicochemical properties of ionic liquids (ILs) make them very desirable for biomedical applications, such as surface-active ionic liquids (SAILs). SAILs surface activity, intrinsically higher than conventional surfactants, allows them to enhance drug permeability across biomembranes and, thus, become better drug carriers than current solutions. To harvest the full potential of these materials, in-depth studies of ILs interactions with model proteins are necessary to understand the mechanisms controlling these biological processes. Albumin, a key protein of blood serum, is of particular relevance, namely in drug carrier applications. Here we characterize the interaction of bovine serum albumin (BSA) with fluorinated ionic liquids which are SAILs that possess fluorous tags equal to or longer than four carbon atoms. Their impact on BSA stability and structure was evaluated using different biophysical techniques. Differential scanning fluorimetry (DSF) and calorimetry (DSC), as well as circular dichroism (CD), yielded insights on the stabilisation and secondary structure of BSA upon incubation with the ILs. Binding dynamics of the interaction were studied by conductimetry and isothermal titration calorimetry (ITC), which give the values of critical aggregation concentration (*CAC*) of the BSA-IL complex formation, as well as thermodynamic parameters. The results presented herein support the hypothesis that BSA is stabilised and encapsulated in the presence of FILs. Thus, the FILs studied in this work have potential for uses in biomedical applications.

2. Introduction

Ionic liquids (ILs) are salts consisting of organic cations and organic or inorganic anions which present low melting temperatures, usually lower than 373.15 K. Nowadays, ILs are being applied in a variety of fields, such as extraction and separation, biocatalysis, organic synthesis, electrochemistry and polymer science [1–10]. These molten salts present an array of physicochemical properties, such as negligible vapor pressure, non-flammability, high thermal stability, low toxicity and tuneable solvent quality, that depend on their structure and can therefore be easily tailored by altering the anion or cation [11,12]. For instance, the presence of longer alkyl chains increases surface activity of ILs, which are then referred to as surface active ionic liquids (SAILs) [1,13]. SAILs behave like surfactants, and their hydrophobicity can be controlled through the length of the alkyl chain, type of headgroup and counterion. Thus, the structure and dynamics of the aggregates that are formed, such as micelles, can be finely tuned. The ability of SAILs to enhance drug permeability across biomembranes and to act as better drug carriers than conventional surfactants makes them very desirable to the pharmaceutical industry [11,14,15]. Moreover, formulations containing SAILs and proteins can have commercial applications in cosmetics, detergents and biochemical reactions [16].

The interaction between surfactants and proteins needs to be well understood, since it can alter the intramolecular forces responsible for maintaining protein secondary structure, which can either lead to stabilization or unfolding/misfolding/refolding [16,17]. The effect of this interaction depends both on the protein and SAIL characteristics, such as polarity, hydrophobicity, viscosity and solvent miscibility [2,11].

Fluorinated Ionic Liquids (FILs) are SAILs that contain fluorous tags with four or more carbon atoms, forming distinct aggregated structures (from spherical to lamellar micelles) depending on their total concentration in aqueous solution [18]. Recently, FILs have also been shown to be biocompatible and non-toxic in four human cell lines (Caco-2, HepG2, EA.hy926 and HaCaT) and in aquatic species with different levels of biological organization (*Vibrio fischeri, Daphnia magna and Lemna minor*) [19,20]. Furthermore, we have previously evaluated the effect of these biocompatible FILs using lysozyme as a model protein [21]. However, more studies are needed with other model and therapeutic proteins to better understand the interactions, encapsulation and assess the potential of these FILs for biological applications such as protein drug carrier functions.

In the present work we have selected bovine serum albumin (BSA), a model protein with increased molecular mass and higher complexity compared to lysozyme. Our aim is to investigate BSA in the context of its interaction and encapsulation with FILs. BSA is a standard protein used in different procedures due to its well characterized structure, physicochemical properties, stability and solubility [22,23]. This biological macromolecule is an acidic, non-glycosylated, 66 kDa protein, with approximate dimensions of 140 × 40 × 40 Å^3 [24]. Serum albumins are important to maintain the osmotic pressure and pH in the blood [24] and present several binding sites which allow the transport of metabolites, hormones and fatty acids in the body fluids of vertebrates [22]. Serum albumins have a heart shaped structure with three helical domains, which in turn comprise two subdomains with common structural motifs connected by a long loop [23]. Pockets are formed between these domains and subdomains displaying an intrinsic mobility that enables albumin to bind ligands with different sizes and chemical properties [22].

Studies on the interaction of BSA with different SAILs have been previously reported [17,25–29]. Geng *et al.* showed that one SAIL with imidazolium derived cation was able to bind to BSA and stabilize its structure at low concentrations. However, protein denaturation occurred using SAIL at its critical micelle concentration (*CMC*) [17,25]. Singh *et al.* studied the interaction of amphiphilic IL based on chloride and sulfate anions with BSA, which is governed by hydrophobic, electrostatic and hydrogen bonding interactions. Protein unfolding was also observed for both SAILs at concentrations around 1/3 or 1/2 of their *CMC* values [26]. Wang *et al.* synthesized two SAILs with long alkyl chains in the anion that showed higher surface activity than traditional surfactants, but that compromised BSA secondary structure at 1x *CMC*, and induced more severe changes at 2.5x *CMC* [27]. Banerjee *et al.* characterized giant SAIL vesicles, which were then loaded with BSA. The SAILs caused partial unfolding of the protein, with SAILs containing aromatic moieties having a bigger effect on protein denaturation, with an increase in BSA hydrodynamic radius of up to 2-fold [28]. Thoppil *et al.* also synthesized SAILs with higher surface activity than traditional surfactants, and BSA micellization was found to be a spontaneous process occurring in four stages. Nevertheless, BSA was destabilized and unfolded at concentrations equal to or higher than the *CMC* [29].

Herein, the impact of FILs on the stability, structure and encapsulation of BSA is assessed and compared with the behaviour of a non-surfactant IL. Different biophysical techniques, such as isothermal titration calorimetry (ITC), differential scanning calorimetry

(DSC) and fluorimetry (DSF), and circular dichroism (CD), were used to investigate the interactions of FILs with BSA, as well as their binding dynamics. Moreover, the self-aggregation behaviour was analysed using ionic conductivity and ITC measurements. The final goal is to determine if BSA is stabilized and encapsulated by non-toxic and biocompatible FILs, as such clarification would enable the potential use of these systems for biomedical applications in the future.

3. Experimental procedures

3.1 Materials

Lyophilized bovine serum albumin, BSA (A7030) and potassium chloride, KCl (purity 99.0%, P9333) were purchased from Sigma-Aldrich and HEPES (4-(2-hydroxyethyl)-1-piperazineethanesulfonic acid) buffer (purity 99.5%, 9105) was from Roth. Cholinium ((2-hydroxyethyl)trimethylammonium) dihydrogen phosphate, $[N_{1112(OH)}][H_2PO_4]$ (> 98% mass fraction purity), cholinium perfluorobutanesulfonate, $[N_{1112(OH)}][C_4F_9SO_3]$ (> 97% mass fraction purity), 1-ethyl-3-methylimidazolium perfluorobutanesulfonate, $[C_2C_1Im][C_4F_9SO_3]$ (> 97% mass fraction purity) were supplied by IoLiTec GmbH. To reduce the volatile chemicals and water contents, all ILs were dried under vacuum (4 Pa) with vigorous stirring at about 323 K for at least 2 days, immediately prior to their use. No further purification was carried out and the purity of all ILs was checked by ^1H and ^{19}F NMR. The water content was determined using a Metrohm 831 Karl Fisher Coulometer, obtaining less than 100 ppm in all ILs. The chemical structures of the ionic liquids used in this work are shown in Table 3.1.

Table 3.1. Chemical structures and acronyms of the ionic liquids (ILs).

IL Designation	Chemical Structure	Critical Aggregation Concentration (*CAC*) in water
Cholinium dihydrogen phosphate $[N_{1112(OH)}][H_2PO_4]$		Non-surfactant
Cholinium perfluorobutanesulfonate $[N_{1112(OH)}][C_4F_9SO_3]$		16.07 mM (0.65% *v/v*) [18]
1-Ethyl-3-methylimidazolium perfluorobutanesulfonate $[C_2C_1Im][C_4F_9SO_3]$		14.55 mM (0.60% *v/v*) [18]

3.2 Protein purification

Size exclusion chromatography was undertaken in order to isolate BSA monomer and ensure its monodispersity in the following studies. Briefly, lyophilized BSA was reconstituted in 50 mM HEPES pH 7.5, 50 mM KCl and loaded onto a HiLoad 16/600 Superdex 200 column (GE Healthcare) which was pre-equilibrated in the same buffer. Fractions of 1.5 mL were collected and those corresponding to the BSA monomer were pooled and flash frozen in liquid nitrogen. Aliquots were thawed, centrifuged (9184 *xg*, 10 min, 277.15 K) and used for further experiments. All assays were performed using 50 mM HEPES pH 7.5, 50 mM KCl buffer, unless otherwise stated.

3.3 Thermal shift assays

Thermal stability of BSA in the presence or absence of ILs was evaluated using three methods: differential scanning fluorimetry (DSF), nano differential scanning fluorimetry (nanoDSF) and differential scanning calorimetry (DSC). All experimental data on thermal stability were analysed with GraphPad Prism 8.0 (GraphPad Software, San Diego, USA), using one-way ANOVA followed by Dunnet test, when appropriate. The differences were considered significant when $p < 0.005$. The methodology followed for obtaining each set of experimental data each is described hereafter.

DSF monitors protein unfolding with temperature using a sensitive dye which fluoresces upon binding to the hydrophobic amino acid residues that become exposed as the protein unfolds. DSF experiments were performed in a QuantStudio 7 Flex Real Time PCR detection system (Applied Biosystems), using 96-well Endura plates sealed with optical adhesive films (MicroAmp, Applied Biosystems), with a final volume of 20 µL for each reaction, using Protein Thermal Shift Dye (1000x, Applied Biosystems) as probe. An initial screen was done using BSA in the range of 0.1–0.5 mg·mL^{-1} with probe diluted 2, 4 and 6-fold. The combination yielding the best fluorescence signal consisted of 0.25 mg·mL^{-1} of BSA with 2x diluted dye. The subsequent DSF experiments were all carried out using this protein/dye ratio, with the addition of ionic liquid at concentrations below and above critical aggregation concentration (*CAC*), from 0 to 2.5% *v/v*. Control assays were used to analyse the behaviour of ILs with the probe in the absence of protein. Sealed plates were heated from 293.15 to 363.15 K in 1 K·min^{-1} increments, and fluorescence intensity was monitored

with the ROX filter (λ_{exc} = 580 ± 10 and λ_{em} = 623 ± 14 nm). Measurements were performed in triplicate. Dye fluorescence intensity is plotted as a function of temperature, where the midpoint of the unfolding transition corresponds to the melting temperature (T_m).

NanoDSF assays were performed using a Prometheus NT.48 instrument (NanoTemper Technologies). Samples containing 0.25 mg·mL^{-1} BSA with different concentrations of ILs (serial dilution from 2.4 to 0.00015% *v/v*) were loaded into Prometheus Capillaries (NanoTemper Technologies). Temperature was increased from 293.15 to 363.15 K at a rate of 1 K·min^{-1}, while intrinsic fluorescence intensity was recorded at 330 and 350 nm. T_m is then calculated from the inflection point of the unfolding curves (or the minimum of the first derivative) similarly to the previous DSF assay.

DSC is a thermoanalytical technique in which the difference in the amount of heat required to increase the temperature of a sample and reference is measured as a function of temperature. The plot shows the heat capacity (Cp) as a function of temperature, where T_m corresponds to the maximum of the melting transition. DSC measurements were carried out in a VP-DSC microcalorimeter (MicroCal/Malvern Instruments, UK) with BSA at 1 mg·mL^{-1} in the presence of 0.6, 1.2 and 2.5% *v/v* ILs. All samples were degassed and then loaded onto the cells. The reference cell was filled with 50 mM HEPES pH 7.5 and 50 mM KCl. Thermal scans were performed from 293.12 to 373.12 K at a rate of 1.5 K·min^{-1}. At least two scans were conducted for each sample. Resulting data were subtracted from a buffer-buffer baseline and processed using the MicroCal Origin software.

3.4 Circular dichroism

CD is an absorption spectroscopy method based on the differential absorption of left and right circularly polarized light that can provide information on protein structure. CD spectra were measured on a JASCO J-815 spectropolarimeter (JASCO Inc, USA) at 293.15 K with a quartz cuvette of 0.1 cm path length. All samples were prepared in 55 mM KH_2PO_4 and 100 mM KCl in order to avoid an interfering signal from HEPES buffer in the far-UV. Final concentrations were 0.2 mg·mL^{-1} for BSA, and 0.6, 1.2 and 2% *v/v* for $[N_{1112(OH)}][C_4F_9SO_3]$. Samples were incubated during at least 30 min at room temperature prior to the CD experiments. CD spectra were acquired at scan speeds of 50 nm·min^{-1} with 4 accumulations and a response time of 1 s. Two different replicates were obtained and

merged for each CD experiment. Spectral deconvolution was carried out with Dichroweb, using the K2D algorithm [30,31].

3.5 Conductometry measurements

Conductometry measures electrical conductivity due to free ions in solution and the motion of ionic charge, thus monitoring ion mobility. Ionic conductivities were measured at 298.15 K with a CDM210 Radiometer Analytical conductometer using a CDC749 electrode in a glass vial with a magnetic stirrer. The equipment was calibrated using the certified 0.01 D and 0.1 D KCl standard solutions provided by Radiometer Analytical. The samples were in a thermostatised water bath where the temperature was monitored by a platinum resistance thermometer coupled to a Keithley 199 multimeter (with an uncertainty of $\pm$ 0.01 K). Two different experiments were performed: i) $[C_2C_1Im][C_4F_9SO_3]$ blank, and ii) 0.2 mg$\cdot$mL^{-1} BSA in the presence of $[C_2C_1Im][C_4F_9SO_3]$, in the tested concentration range (up to ~98 mM or 4% *v/v*, and diluted in the above mentioned buffer). Each solution was added to the vial and allowed to equilibrate prior to the measurements. At least three conductivity measurements were recorded, and the uncertainty of the measurements is estimated to be lower than 1%.

3.6 Isothermal titration calorimetry

ITC is a staple technique for the determination of binding interactions involving proteins. Through the measurement of the heat that is either released or absorbed during a biomolecular binding event a thermodynamic profile can be plotted, and parameters such as enthalpy and affinity are calculated [17]. BSA-FIL interactions were studied using a VP-ITC (Microcal, USA). The sample cell was loaded with 0.1 mM BSA (~6.6 mg$\cdot$mL^{-1}), the reference cell was filled with buffer and the syringe was filled with a $[C_2C_1Im][C_4F_9SO_3]$ solution. The solution was titrated into the protein in four consecutive reactions with increasing FIL concentration (1, 10 and 100 mM) in order to obtain a complete profile. All samples were degassed prior to use. After temperature stabilization at 298.15 K, FIL was added to the sample cell as a sequence of 29 injections of 10 μL each, per reaction, using a Hamilton syringe with continuous stirring at 200 rpm. Each injection lasted for 12 s, with an interval of 240 s between injections, to allow re-equilibration. Control experiments were

performed for the FIL and BSA. The measurement of the enthalpy variation at each injection yielded raw data peaks that were then transformed into an integrated heat profile using the Microcal Origin software. A single site binding model was chosen to fit the experimental data and calculate the thermodynamic parameters.

4. Results and Discussion

4.1 Protein thermal stability

BSA melting temperature (T_m) was measured in the absence or presence of ILs using different thermal shift assays. The effect of ILs on the stability of BSA is herein discussed, along with the basic principles, outputs, and limitations of each technique. T_m is the temperature at which both folded and unfolded states of the protein coexist at equilibrium and is calculated from the thermal denaturation profiles. Shifts in T_m indicate changes in protein stability and can provide insights into protein-IL interactions.
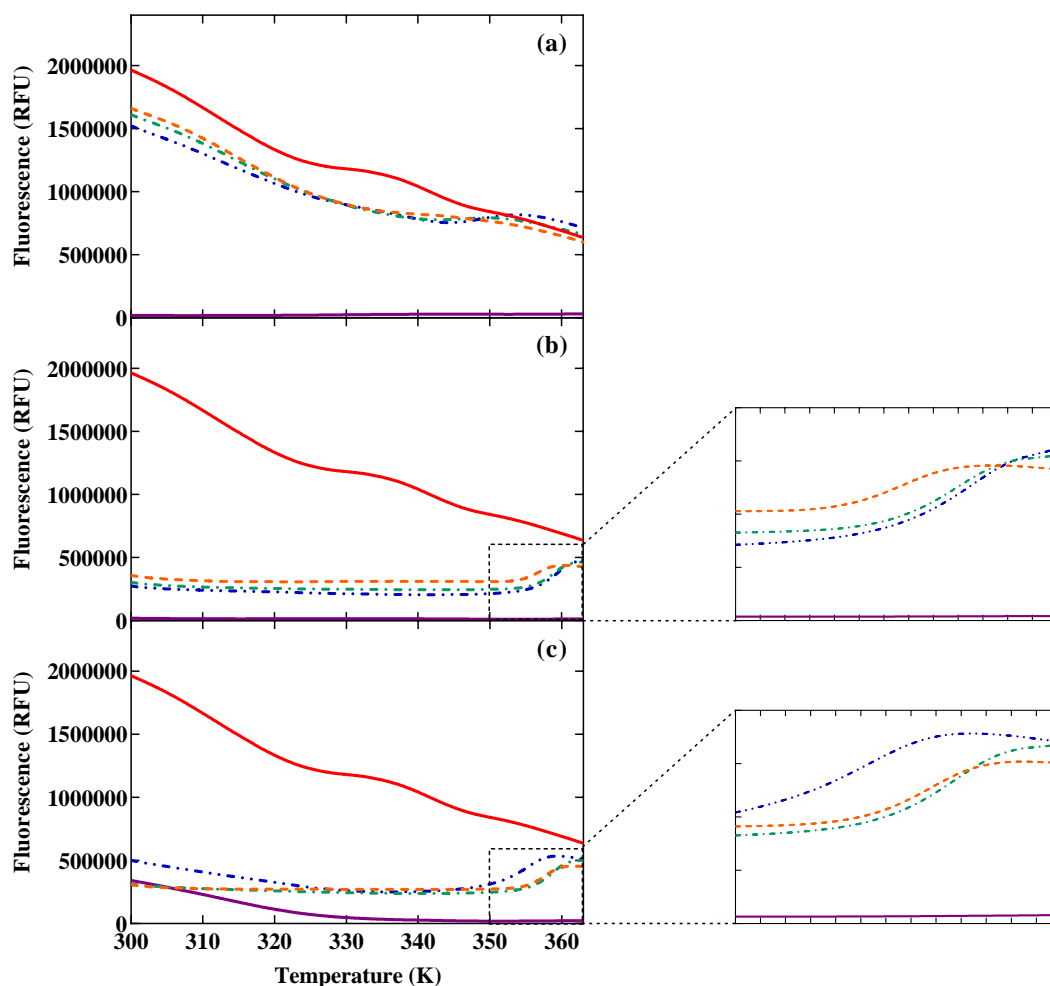
Figure 3.1. Differential Scanning Fluorimetry raw data for 0.25 mg·mL^{-1} BSA in the presence of (a) [N$_{1112(OH)}$][H$_2$PO$_4$], (b) [N$_{1112(OH)}$][C$_4$F$_9$SO$_3$], and (c) [C$_2$C$_1$Im][C$_4$F$_9$SO$_3$]; where (——) represents BSA in the absence of IL, (– – · , – · – , – · ·) refer to BSA in the presence of 0.6, 1.2 and 2.5% *v/v* IL, respectively, and (——) displays 2.5% *v/v* IL Blank. Inserts show BSA transition curves in more detail.

DSF monitors protein unfolding using a sensitive dye. As temperature increases and the protein unfolds, it exposes hydrophobic surfaces that bind the dye, resulting in the observed increase in fluorescence. The midpoint of this unfolding transition corresponds to the T_m. The thermogram obtained for BSA shows an unusually high initial fluorescence signal (Figure 3.1), which is likely caused by dye binding to the exposed hydrophobic pockets of albumin [32]. Remarkably, this initial high signal is significantly reduced upon addition of ILs to the protein; around 80% for $[N_{1112(OH)}][C_4F_9SO_3]$ and $[C_2C_1Im][C_4F_9SO_3]$ FILs, in contrast with only 15% for non-surfactant IL $[N_{1112(OH)}][H_2PO_4]$ (Figure 3.1). ILs may be arranging around the albumin structure in such a way that hinders the access of the fluorescent dye to the protein hydrophobic pockets. This would lead to a decrease in initial fluorescence, which is more pronounced for the surfactant FILs, probably due to a stronger interaction with BSA. IL controls (2.5% *v/v*) show no initial fluorescence (Figure 3.1a-b) except for $[C_2C_1Im][C_4F_9SO_3]$, although it does not interfere with the transition peak (Figure 3.1c).

Despite the poor definition of the melting curves for BSA and BSA+$[N_{1112(OH)}][H_2PO_4]$ (Figure 3.1a) using DSF, it was still possible to determine protein T_m (330 K, see Table 3.2) that is in accordance with the literature [32]. Addition of surfactant FILs increases the definition of the unfolding peaks, which are shifted towards higher temperatures (Figure 3.1b-c).

Table 3.2. Comparison of BSA melting temperature (T_m, K) measured by DSF, nanoDSF and DSC.

	DSF				nanoDSF				DSC			
	0	0.6	1.2	2.5	0	0.6	1.2	2.5	0	0.6	1.2	2.5
$[N_{1112(OH)}][H_2PO_4]$	330.3 ± 1.09	341.2 ± 0.62	346.7 ± 0.72	348.4 ± 0.18	333.1	336.9	337.5	335.6	334.5 ± 0.13	337.8 ± 0.06	337.9 ± 4.6	335.5 ± 0.28
$[N_{1112(OH)}][C_4F_9SO_3]$	330.3 ± 1.09	356.7 ± 0.09	358.9 ± 0.13	359.6 ± 0.04	333.3	358.5	360.7	361.9	334.5 ± 0.13	358.9 ± 0.09	361.3 ± 0.09	362.5 ± 0.13
$[C_2C_1Im][C_4F_9SO_3]$	330.3 ± 1.09	357.8 ± 0.00	358.7 ± 0.04	355.3 ± 0.25	332.9	359.8	360.6	357.5	334.5 ± 0.13	359.7 ± 0.05	361.4 ± 0.06	359.5 ± 0.17

Mean values were obtained from triplicate (DSF) or duplicate (DSC) measurements with their standard deviations. NanoDSF results were obtained from a single experiment.

As can be seen in Figure 3.2, BSA T_m increased significantly in the presence of ILs in all tested conditions, indicating protein stabilization by the ionic liquids. The addition of ILs at the highest concentration (2.5% *v/v*) resulted in an increase of T_m by approximately 18 K for $[N_{1112(OH)}][H_2PO_4]$, 29 K for $[N_{1112(OH)}][C_4F_9SO_3]$, and 25 K for $[C_2C_1Im][C_4F_9SO_3]$. Noteworthy, a slight decrease on the protein T_m is observed upon addition of

[C$_2$C$_1$Im][C$_4$F$_9$SO$_3$] at 2.5% compared to 1.2% *v/v*. In contrast, incubation of these FILs with lysozyme showed no relevant impact on its thermostability (T_m determined by DSF was ~ 351 K), in fact protein T_m decreased around 4 K upon addition of surfactant FILs at 1.2% *v/v* (maximum concentration tested)[21]. This shows some level of discrimination in the BSA-FILs interaction system, as not all protein-FILs interaction lead to equal results.
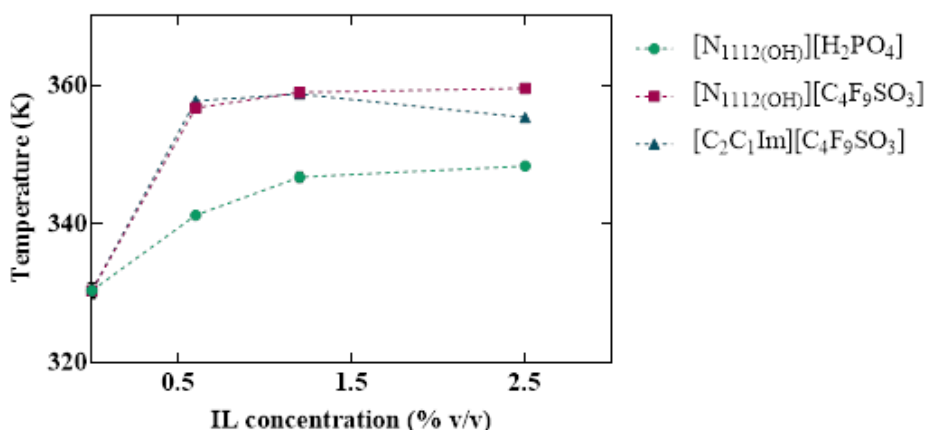
Figure 3.2. T_m values from Differential Scanning Fluorimetry of BSA (0.25 mg·mL^{-1}) in the presence of [N$_{1112(OH)}$][H$_2$PO$_4$], [N$_{1112(OH)}$][C$_4$F$_9$SO$_3$], and [C$_2$C$_1$Im][C$_4$F$_9$SO$_3$], at 0.6, 1.2 and 2.5% *v/v*. The error bars indicate the standard deviations around the mean values values from triplicate measurements.

As DSF showed inherent limitations to study BSA thermostability due to the high initial dye fluorescence values, nanoDSF assays were also performed, as this technique monitors the intrinsic fluorescence signal of a protein (mainly due to tryptophan residues) as a measure of its folding state. The fluorescent signal is plotted against increasing temperature to determine the protein melting temperature. Moreover, the serial dilution of IL (from 2.4 to 0.0001% *v/v*) with the acquisition of 15 thermal denaturation profiles within this concentration range enables a much more detailed analysis of their influence on BSA stability.

In Figure 3.3 experimental recordings of tryptophan fluorescence at 330 nm are depicted (very similar to 350 nm). As expected, ILs show no fluorescent signal. The T_m values for BSA from nanoDSF (see Table 3.2) are quite similar to the ones obtained by DSF. A decrease of BSA intrinsic fluorescence intensity is observed upon the addition of ILs, more noticeable for FILs. As can be seen in Figure 3.5, [N$_{1112(OH)}$][H$_2$PO$_4$] barely interferes with albumin stability (maximum increment in T_m ~ 4 K at 1.3% *v/v*). In the case of FILs however, T_m gradually increases with their concentration, showing a more accentuated slope after

0.0023% *v/v* and reaching its maximum at 2.4% *v/v* for $[N_{1112(OH)}][C_4F_9SO_3]$ (+28.7 K) and 1.2% *v/v* for $[C_2C_1Im][C_4F_9SO_3]$ (+27.5 K), after which a slight decrease is observed.
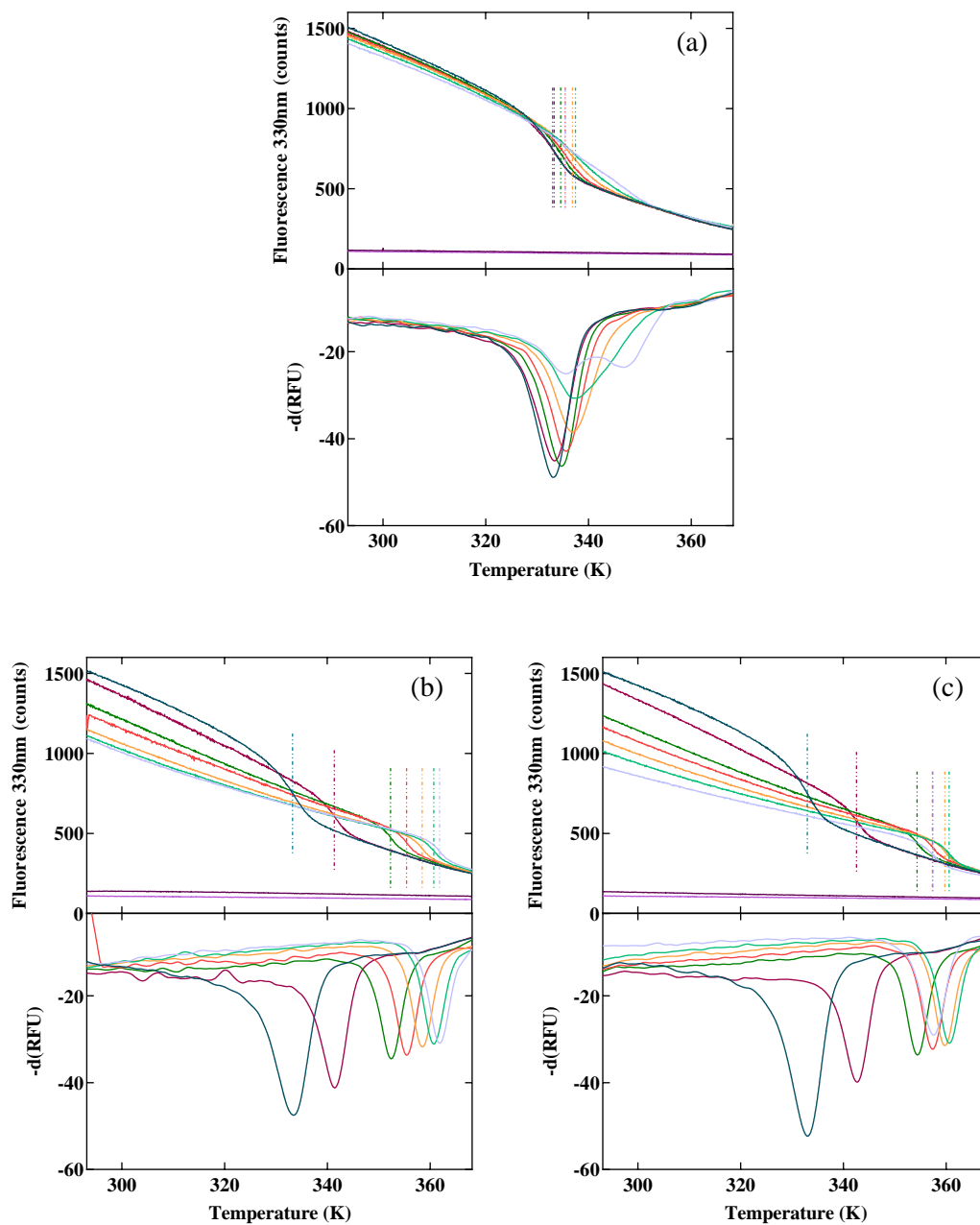
Figure 3.3. Experimental intrinsic fluorescence data at 330 nm and first derivative of nanoDSF with 0.25 mg·mL^{-1} BSA : (a) $[N_{1112(OH)}][H_2PO_4]$, (b) $[N_{1112(OH)}][C_4F_9SO_3]$, and (c)$[C_2C_1Im][C_4F_9SO_3]$, where (——) is BSA without IL, (—— , —— , —— , —— , —— , ——) correspond to BSA in the presence of 0.01, 0.15, 0.3, 0.6, 1.2 and 2.4 % v/v IL, respectively; (——) is Buffer; and (——) is 2.4% v/v IL Blank. Vertical lines represent T_m.
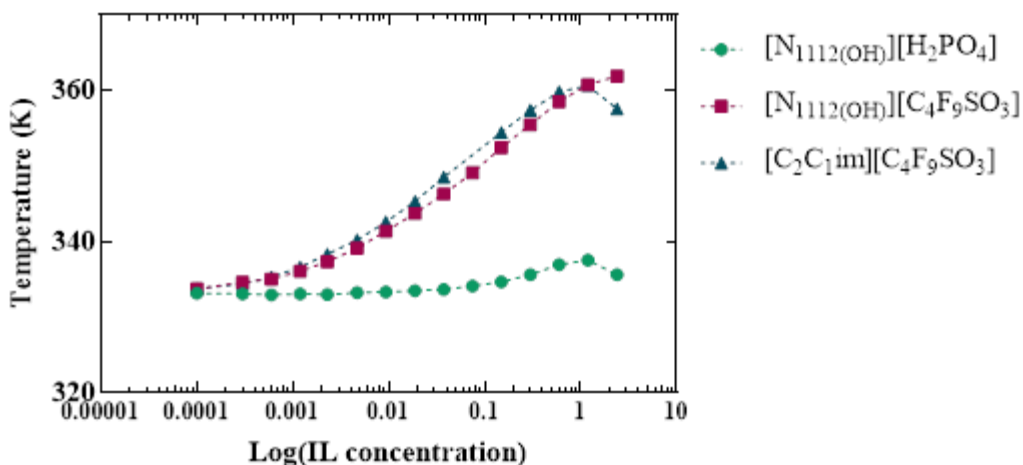
Figure 3.5. T_m values from Nano Differential Scanning Fluorimetry of BSA (0.25 mg·mL^{-1}) in the presence of [N$_{1112(OH)}$][H$_2$PO$_4$], [N$_{1112(OH)}$][C$_4$F$_9$SO$_3$], and [C$_2$C$_1$Im][C$_4$F$_9$SO$_3$] at increasing concentrations.

To rule out differences in T_m due to protein fluorescence quenching by the ILs [17,26], DSC experiments were carried out. DSC monitors the thermodynamic properties of a sample along temperature increase, determining both the temperature and heat flow associated with protein transitions. During a temperature gradient, DSC measures the heat that is radiated or absorbed by the sample, in comparison to the reference [33]. The results from DSC are shown in Figure 3.4 and Table 3.2 and are in good agreement with the previous techniques. A thermostabilizing effect is observed in the presence of both FILs with
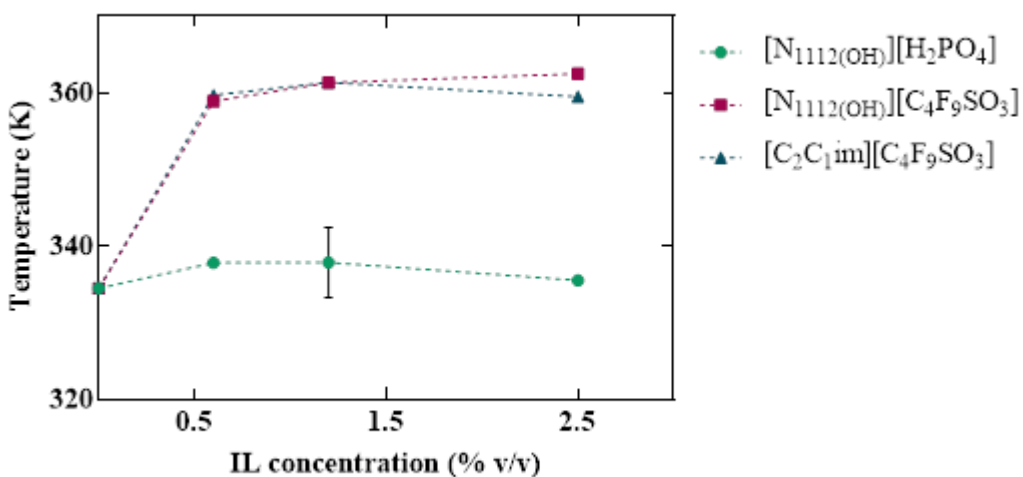
Figure 3.4. T_m values from Differential Scanning Calorimetry of BSA (1 mg·mL^{-1}) in the presence of [N$_{1112(OH)}$][H$_2$PO$_4$], [N$_{1112(OH)}$][C$_4$F$_9$SO$_3$], and [C$_2$C$_1$Im][C$_4$F$_9$SO$_3$], at 0.6, 1.2 and 2.5 % *v/v*. The error bars indicate the standard deviations around the mean values from multiple scans.

a significant increase in BSA T_m from 334.47 to 362.46 K for 2.5% v/v [N$_{1112(OH)}$][C$_4$F$_9$SO$_3$], to 359.46 K for 2.5% v/v [C$_2$C$_1$Im][C$_4$F$_9$SO$_3$], and a non-significant effect of [N$_{1112(OH)}$][H$_2$PO$_4$] on BSA.

Overall, the three techniques yielded very similar results (see Table 3.2). BSA T_m was within the expected values [32], and the behaviour of ionic liquids was also consistent throughout the assays. [N$_{1112(OH)}$][H$_2$PO$_4$] was the IL with least impact on BSA stabilization, whereas surfactant ILs increased T_m by approximately 28 K (> 8%). Notably, [C$_2$C$_1$Im][C$_4$F$_9$SO$_3$] at 2.5% v/v consistently reduces T_m by ~ 3 K, which can indicate a turning point in BSA stability.

4.2 Structural studies

CD spectroscopy was used to probe BSA secondary structure, since the spectra are characteristic of different structural elements. Measurements were recorded from 190 to 260 nm with and without IL. Since [C$_2$C$_1$Im][C$_4$F$_9$SO$_3$] has a high signal intensity due to the imidazolium ring, and therefore is not technically feasible for CD, spectra were only measured for [N$_{1112(OH)}$][C$_4$F$_9$SO$_3$]. This FIL was incubated with BSA prior to the CD experiments at concentrations below and above its *CAC* (0.65% v/v) (Figure 3.6). The protein secondary structure content was predicted with DichroWeb K2D [30,31,34] and is displayed in Table 3.3.
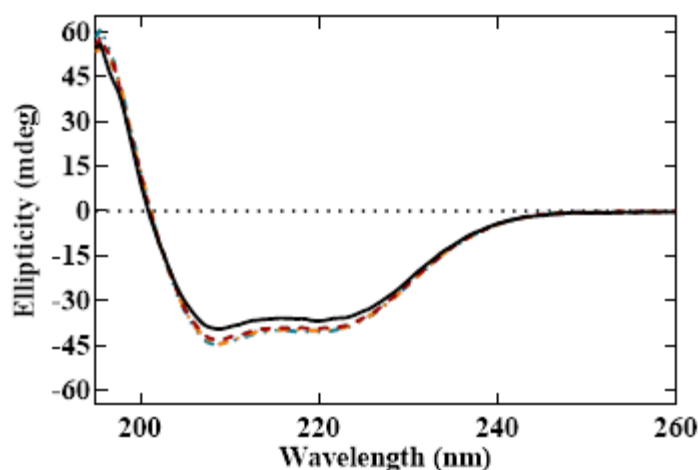
Figure 3.6. CD spectra of BSA (0.2 mg·mL^{-1}) in the absence (——) or presence of [N$_{1112(OH)}$][C$_4$F$_9$SO$_3$] at (– – ·) 0.6, (– · –) 1.2 and (– · · ·) 2% v/v.

The native BSA spectrum presents two negative bands in the far-UV region at 208 and 220 nm, which are distinctive of α-helical structure [26], and the predicted α-helical content of 70% is also in good agreement with previous reports [35,36]. Upon IL addition, BSA maintains its characteristic spectra, with a slight increase (8%) in molar ellipticity, which may indicate secondary structure stabilization [37] and a more compact state of BSA [17]. Furthermore, the relative α-helical content also increases in the presence of the IL while the β-sheet and random coil decreases, supporting the conclusion that BSA is stabilized in the presence of $[N_{1112(OH)}][C_4F_9SO_3]$ at concentrations up to 2% *v/v*. Previous CD studies conducted with lysozyme and the same FIL showed a similar behaviour [21], although the *α*-helical content increment was less pronounced (~2.5%). Thus, this implies, again, in agreement with the above thermal stability data, that the BSA-FILs system is more stable than when other proteins are employed.

Table 3.3. Secondary structure prediction of BSA (0.2 mg·mL^{-1}) with FIL $[N_{1112(OH)}][C_4F_9SO_3]$**.**

Secondary structure content	Concentration of FIL (% in *v/v*)			
	0	0.6	1.2	2
α-helix	0.7	0.78	0.79	0.8
β-sheet	0.03	0.01	0.01	0.01
Random coil	0.26	0.21	0.2	0.2

4.3 Self-aggregation behaviour

Ionic conductivity measurements were performed to assess the micellization process of $[C_2C_1Im][C_4F_9SO_3]$ in buffer and in the presence of BSA. Overall, ionic conductivity increases as FIL concentration also increases (Figure 3.7). The deviation from linear behaviour and the changes of slope are directly related to the different transitions and the critical aggregation concentrations. These *CAC*s (data in Table 3.4) were calculated using the Phillips definition [38], where *CAC* is the concentration which corresponds to the maximum change in gradient in the ionic conductivity–concentration curve. All transitions are depicted in Figure 3.7 and Figure 3.8 together with the conventional conductivity curves.
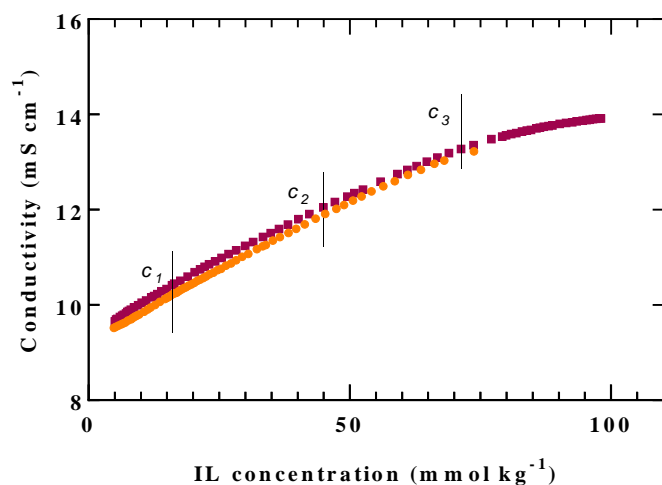
Figure 3.7. Conductivity profile for $[C_2C_1Im][C_4F_9SO_3]$ at 298.15 K, measured in (■) 50 mM HEPES pH 7.5, 50 mM KCl, and (●) 50 mM HEPEs pH 7.5, 50 mM KCl in the presence of 0.2 mg·mL^{-1} BSA.
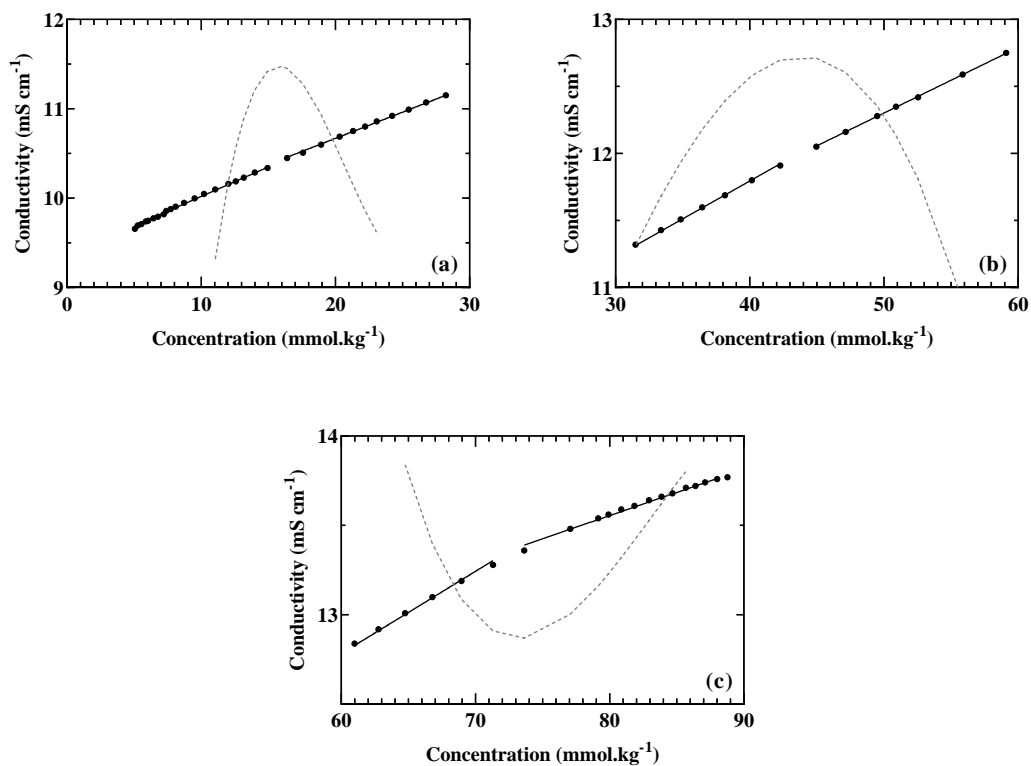
Figure 3.8. Concentration dependence of the ionic conductivity for $[C_2C_1Im][C_4F_9SO_3]$ at 298.15 K (a) the first critical aggregation concentration, (b) the second critical aggregation concentration, and (c) the third critical aggregation concentration. Dashed lines show the maximum change in the gradient of ionic conductivity as a function of FIL concentration, second derivative

Firstly, $[C_2C_1Im][C_4F_9SO_3]$ ionic conductivities were measured in buffer. In the tested concentration range (up to ~98 mM or 4% *v/v*) three transitions were observed, as reported in a previous work where the FIL was tested in water [18]. The first transition corresponds to the *CAC* from traditional surfactants, while the 2nd and 3rd *CAC*s are associated with the presence of increasingly more complex structures that are formed with the increment of FIL concentration [18]. After each *CAC*, the rate of conductivity increase becomes smaller since micelles have lower mobility than free ions. The values obtained for the *CAC*s are similar to those observed in the FILs aqueous solutions (see Table 3.4). A slight increment is detected for the measurements in buffer, except for the third *CAC*. At low concentrations of FIL, the buffer ions may be obstructing the self-aggregation of the FILs. However, when the concentration of the FIL ions is increased, this obstruction no longer exists.

Table 3.4. Parameters determined by conductometry at 298.15 K for FIL and FIL+BSA. Critical aggregation concentrations, *CAC*, ionization degree, *α*, and Gibbs free energy of aggregation, ΔG^0_{agg}.

		mM	% *v/v*	α	ΔG^0_{agg} / kcal.mol^{-1}
$[C_2C_1Im][C_4F_9SO_3]$ in buffer	1st *cac*	15.712	0.64	0.89	-3.5
	2nd *cac*	43.258	1.77	0.87	-2.9
	3rd *cac*	71.628	2.92	0.47	-3.4
$[C_2C_1Im][C_4F_9SO_3]$ + BSA (0.2 mg mL^{-1}) in buffer	1st *cac*	16.341	0.67	0.94	-3.3
	2nd *cac*	44.053	1.8	0.84	-2.9
	3rd *cac*			n.a.	
$[C_2C_1Im][C_4F_9SO_3]$ in H_2O [18]	1st *cac*	14.538	0.6	0.79	-5.9
	2nd *cac*	38.646	1.58	0.84	-4.97
	3rd *cac*	81.76	3.32	0.29	-6.58

$[C_2C_1Im][C_4F_9SO_3]$ in the presence of BSA was tested only up to 73 mM (~3% *v/v*) due to concerns regarding protein denaturation, as seen in the Protein Thermal Stability section. Nevertheless, two transitions were still observed, and the *CAC* values obtained are very similar to the ones from FIL in the absence of BSA (0.64 to 0.67% *v/v* and 1.77 to 1.80% *v/v*). These results indicate that BSA does not impact FIL micellization. The minimal difference might also be related to a slight increase in the difficulty of the FIL self-aggregation in the presence of this protein.

The ratio of the slopes before and after each *CAC* was also used to determine the degree of ionization of the aggregates (*α*). In solution, the monomers of ionic surfactants are completely dissociated, but within the aggregates they are partially associated with the counterions. This behaviour is described by *α*, which is related to the fraction of charges of surfactant in the micelle neutralized by micelle bound counterions. Table 3.4 also contains the values of *α*, where a lower *α* value indicates a better packed micelle. Following the above discussion, the best packing is observed for the FIL aqueous solutions. The *α* values obtained for [C$_2$C$_1$Im][C$_4$F$_9$SO$_3$] *CAC* in buffer are higher than the reference [18], indicating that the micelles are not as well packed during the first transition, probably due to the presence of ions from the buffer which may interfere with FIL solvation. The degree of counterion binding, or fraction of counterions condensed on the aggregate surface (*β)* can also be calculated from the degree of ionization:

$$\beta = 1 - \alpha \tag{1}$$

The values of *β* are associated to the charge density at the surface of the aggregate, its size, and the hydrophobic nature of the counterion. The trends of these parameters are the same as those observed in the *α* values. Furthermore, the increment of FIL concentration is directly related to higher *β* and smaller *α* values (see Table 3.4) which is associated with a more efficient packing of the polar headgroups, changing the shape of the aggregates. For the second *CAC*, there is no significant difference between the degree of ionization in any of the samples.

Standard Gibbs free energy of aggregation (ΔG^0_{agg}) accounts for the free energy required for transferring one mole of surfactant from the aqueous solution to the micellar pseudophase [39], indicating the free energy difference per mole between FIL monomers in solution and in aggregates. ΔG^0_{agg} was determined for the ionic surfactants using the following equation:

$$\Delta G^0_{agg} = RT\,(\beta + 1)\ln x{\cdot}CAC \tag{2}$$

where *R* and *T* represent the universal gas constant and absolute temperature respectively, and *x·CAC* is the critical aggregation concentration defined in mole fraction. Spontaneous aggregation processes are characterized by ΔG^0_{agg} < 0. The difference in ΔG^0_{agg} between

the reference and experimental data indicates that $[C_2C_1Im][C_4F_9SO_3]$ micellization is more favourable in water, probably due to the lack of other ions that can hinder FIL aggregation.

Since similar α and ΔG^0_{agg} were obtained for both samples with or without protein, we conclude that BSA does not interfere in the $[C_2C_1Im][C_4F_9SO_3]$ micellization.

4.4 Study of FIL-BSA interactions

ITC provides great insight into the aggregation of surfactants and their interaction with proteins without the need for labels. Besides, this technique provides useful information about thermodynamic behaviour of these complex systems. In order to obtain the binding constants and thermodynamic parameters for the interaction of BSA with $[C_2C_1Im][C_4F_9SO_3]$, one continuous reaction was performed in four consecutive batches of increasing FIL concentration. Control experiments were performed for the FIL (Figure 3.9) and BSA, although the calorimetric profile for BSA showed no relevant behaviour.
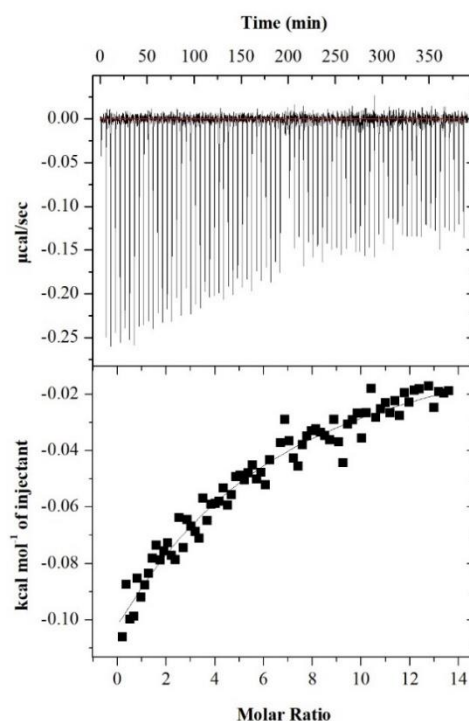
Figure 3.9. ITC profile for $[C_2C_1Im][C_4F_9SO_3]$ titrated into buffer. Top panel: ITC raw profile of heat flow against time; Bottom panel: Corresponding integrated heat profiles plotted as the amount of heat liberated as a function of the molar ratio.
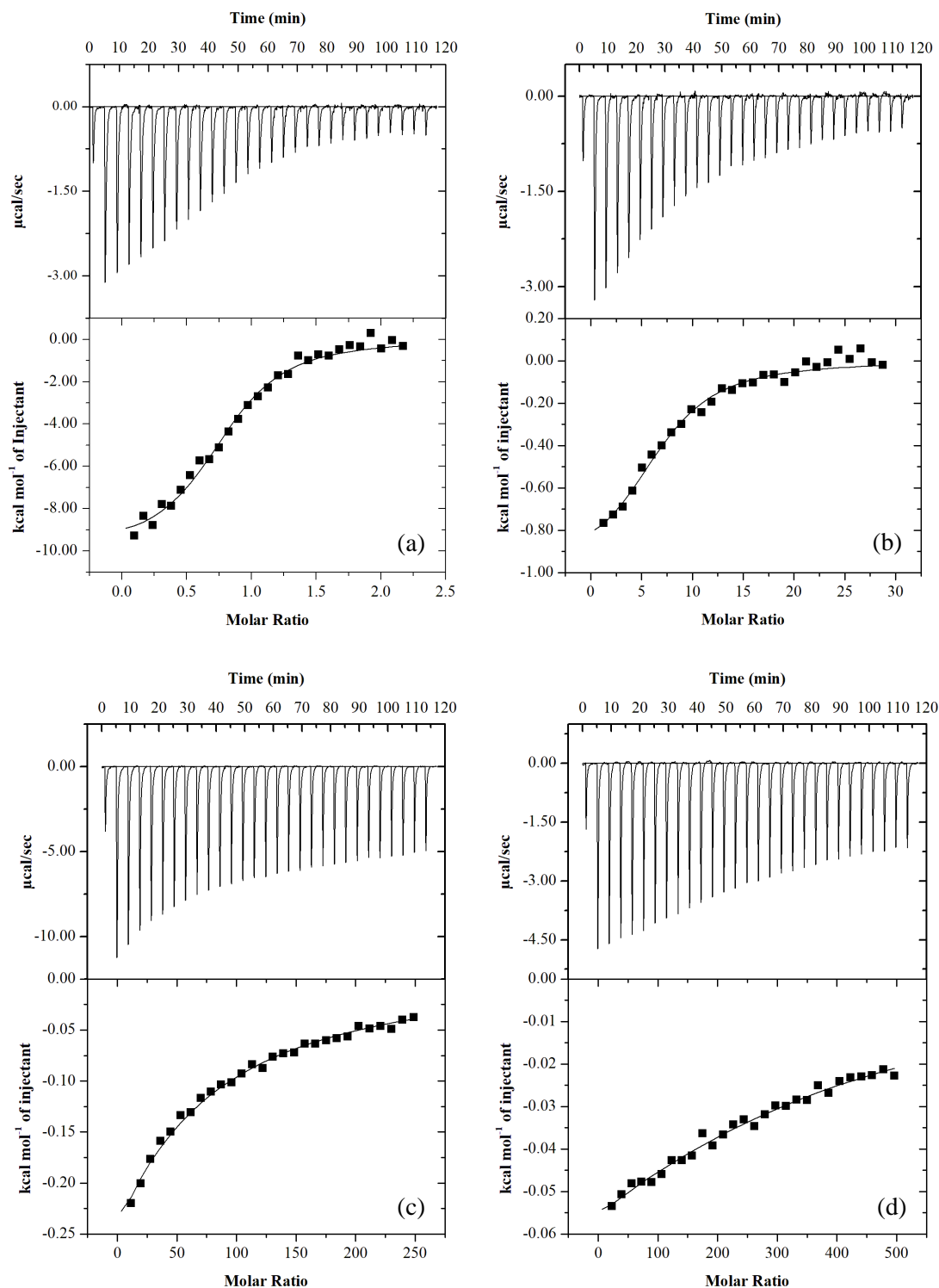
Figure 3.10. ITC profiles for the continuous titration of [C$_2$C$_1$Im][C$_4$F$_9$SO$_3$] at 1 mM (a), 10 mM (b), 100 mM (c and d) into 0.1 mM BSA (~ 6.6 mg·mL^{-1}) in buffer at 295.15 K. Top panels: ITC raw profile of heat flow against time; Bottom panels: corresponding integrated heat profiles plotted as the amount of heat liberated as a function of the molar ratio.

Figure 3.10 depicts the interaction profile of each batch. The top panel represents the calorimetric titration profile, where each peak corresponds to a single injection of FIL solution, and the bottom panel is the resulting heat profile after peak integration and correction for dilution. From these profiles, we observe that all four batches display exothermic changes and that there are at least four binding events in the concentration range studied.

For obtaining the binding and thermodynamic parameters, the 'One set of sites' binding model from the Microcal software was used for each data set. The resulting binding/affinity constant, K_D, and enthalpy of aggregation, ΔH^0_{agg}, were used to calculate ΔG^0_{agg} from Equation 3, and the standard entropy of aggregation, $-T\Delta S^0_{agg}$, from the Gibbs−Helmholtz equation (Equation 4):

$$\Delta G^0_{agg} = RT \ln K_D \tag{3}$$

$$\Delta G^0_{agg} = \Delta H^0_{agg} - T\Delta S^0_{agg} \tag{4}$$

The values obtained are detailed in Table 3.5 and are in agreement with the values determined from conductivity measurements.

Table 3.5. Binding constant (K_D), and thermodynamic properties of aggregation of [C$_2$C$_1$Im][C$_4$F$_9$SO$_3$] titrated into BSA solution determined by ITC at 298.15 K.

	K_D mM	K_D % *v/v*	ΔH kcal·mol-1	ΔG kcal·mol-1	-$T\Delta S$ kcal·mol·K^{-1}
Batch 1	0.0129	0.0005	-11.2	-6.66	4.51
Batch 2	0.125	0.0052	-1.01	-5.32	-4.31
Batch 3	13.3	0.55	-0.177	-2.56	-2.38
Batch 4	28.3	1.2	-0.0309	-2.11	-2.08
FIL Blank	12.4	0.51	-0.0861	-2.6	-2.51

Batch 1 shows unfavourable entropy ($-T\Delta S^0_{agg} > 0$), which indicates that this event is enthalpy driven and can involve protein conformational changes as well as hydrogen bonding. All other batches are entropy driven, and the binding is driven both by hydrogen bonding and hydrophobic interactions.

Batches 1 and 2 refer to the interaction of BSA with the monomers of $[C_2C_1Im][C_4F_9SO_3]$, before the first *CAC* determined by conductimetry, as neither have been described in the previous work characterizing this FIL [18]. The third batch is in accordance with the first FIL aggregation found in the conductivity measurements. Both the K_D (13.33 mM) and ΔG^0_{agg} (-2.56 kcal·mol^{-1}) obtained in ITC are similar to the 1st *CAC* (16.34 mM) and corresponding ΔG^0_{agg} (-3.3 kcal·mol^{-1}) from conductivity, taking into account the limits of the sensitivity of each technique. The ΔH^0_{agg} from the ITC experiment (-0.18 kcal·mol^{-1}) is however higher than that of its respective blank (-0.09 kcal·mol^{-1}; see Figure 3.9), while the other parameters remain unaffected, indicating that the protein impacts this aggregation process, and that the interaction between $[C_2C_1Im][C_4F_9SO_3]$ and BSA is more intense than the FIL self-aggregation in buffer [40]. Batch 4, which has no correspondence in the conductivity measurements, most likely describes the interaction between BSA and the FIL aggregates.

The results obtained both from ITC and conductivity support the conclusion that BSA is not only interacting with $[C_2C_1Im][C_4F_9SO_3]$, but that it is being encapsulated by the FIL while its stability is improved.

5. Conclusion

In this work, we characterized the interaction of BSA with biocompatible, non-toxic fluorinated ionic liquids known for their high surface-active properties. Three different techniques were used to evaluate protein thermal stability and assess their suitability to measure T_m of BSA with ILs. Although all the techniques yielded similar results, DSF was not the most appropriate one. In the presence of either $[N_{1112(OH)}][C_4F_9SO_3]$ or $[C_2C_1Im][C_4F_9SO_3]$, which showed affinity for the hydrophobic patches on the protein surface, BSA T_m increased by approximately 25 K for concentrations above 0.6% v/v (1x CAC), whereas the same concentration of non-surfactant $[N_{1112(OH)}][H_2PO_4]$ resulted in an increase in T_m of only 3 K. Circular dichroism was used to analyse protein secondary structure. The increase in α-helical content upon incubation of $[N_{1112(OH)}][C_4F_9SO_3]$ suggests that BSA is stabilized and possibly in a more compact state, up to 2% v/v FIL (~3x CAC). This validates the results obtained from the thermal stability assays, and is in contrast to what has been previously reported in the literature, where BSA was usually denatured at SAIL concentrations higher than CAC [17,25–29].

The micellization of $[C_2C_1Im][C_4F_9SO_3]$ was analysed through conductivity assays, where we found that FIL aggregation profile was not affected by BSA, as shown by CAC and ΔG^0_{agg} values. ITC showed a more detailed profile on the FIL-BSA interaction. $[C_2C_1Im][C_4F_9SO_3]$ interacts with BSA at low concentrations, is able to encapsulate the protein, and the FIL-BSA interaction is maintained.

In our previous work characterizing the interaction of lysozyme with FILs, we found that protein encapsulation by $[N_{1112(OH)}][C_4F_9SO_3]$ and $[C_2C_1Im][C_4F_9SO_3]$ caused a slight decrease in protein T_m, although this did not translate into a loss in enzymatic activity. Lysozyme secondary structure in the presence of $[N_{1112(OH)}][C_4F_9SO_3]$ was also studied by CD, where no significant effect was observed. These results complement the ones obtained in the present work: while neither protein showed any denaturation upon interaction with FILs in concentrations up to 2x CAC for lysozyme and 3x CAC for albumin (maximum concentrations tested), BSA demonstrates a clear stabilization likely due to its more flexible structure. The juxtaposition of both sets of results highlights the need for characterizing SAIL interactions and encapsulation using various proteins, since each complex will behave differently according to their characteristics.

Considering FILs compatibility with an important protein from vertebrates, such as albumin, further studies are already under way for future biomedical applications, as a promising potential novel biomaterial for drug delivery systems using therapeutic proteins.

6. References

1.   Pal, A.; Yadav, A. Binding interactions of anesthetic drug with surface active ionic liquid. *J. Mol. Liq.* **2016**, *222*, 471–479, doi:10.1016/J.MOLLIQ.2016.07.076.

2.   Patel, R.; Kumari, M.; Khan, A.B. Recent advances in the applications of ionic liquids in protein stability and activity: A review. *Appl. Biochem. Biotechnol.* **2014**, *172*, 3701–3720, doi:10.1007/s12010-014-0813-6.

3.   Shamsi, S.A.; Danielson, N.D. Utility of ionic liquids in analytical separations. *J. Sep. Sci.* **2007**, *30*, 1729–1750, doi:10.1002/jssc.200700136.

4.   Werner, S.; Haumann, M.; Wasserscheid, P. Ionic Liquids in Chemical Engineering. *Annu. Rev. Chem. Biomol. Eng.* **2010**, *1*, 203–230, doi:10.1146/annurev-chembioeng-073009-100915.

5.   Patel, D.D.; Lee, J.-M. Applications of ionic liquids. *Chem. Rec.* **2012**, *12*, 329–355, doi:10.1002/tcr.201100036.

6.   Sun, P.; Zhang, S.; Pang, J.; Tan, Y.; Sun, D.; Xia, C.; Cheng, X.; Xin, X. *Self-assembly of ionic-liquid-type imidazolium gemini surfactant with polyoxometalates into supramolecular architectures for photocatalytic degradation of dye*; Elsevier B.V, 2018; Vol. 272; ISBN 8653188363.

7.   Sun, P.; Zhang, S.; Xiang, Z.; Zhao, T.; Sun, D.; Zhang, G.; Chen, M.; Guo, K.; Xin, X. Photoluminescent sensing vesicle platform self-assembled by polyoxometalate and ionic-liquid-type imidazolium gemini surfactants for the detection of Cr 3+ and MnO 4− ions. *J. Colloid Interface Sci.* **2019**, *547*, 60–68, doi:10.1016/j.jcis.2019.03.085.

8.   Wang, S.; Yin, X.; Yan, Y.; Xiang, Z.; Liu, P.; Chen, Y.; Xin, X.; Yang, Y. Gold Extraction through Vesicles Self-Assembled by Cationic Gemini Surfactant and Sodium Deoxycholate. *Ind. & Eng. Chem. Res.* **2016**, *55*, 8207–8214, doi:10.1021/acs.iecr.6b01712.

9.   Wang, S.; Zheng, Y.; Zhang, H.; Yan, Y.; Xin, X.; Yang, Y. Ionic-Liquid-Type Imidazolium Gemini Surfactant Based Water-in-Oil Microemulsion for Extraction of Gold from Hydrochloric Acid Medium. *Ind. & Eng. Chem. Res.* **2016**, *55*, 2790–2797, doi:10.1021/acs.iecr.5b04115.

10.   Xiang, Z.; Zheng, Y.; Zhang, H.; Yan, Y.; Yang, X.; Xin, X.; Yang, Y. Effect of spacer length of ionic liquid-type imidazolium gemini surfactant-based water-in-oil microemulsion for the extraction of gold from hydrochloric acid. *New J. Chem.* **2017**, *41*, 6180–6186, doi:10.1039/c7nj00551b.

11.   Harada, L.; Pereira, J.; Campos, W.; Silva, E.; Moutinho, C.; Vila, M.; Oliveira Jr., J.; Teixeira, J.; Balcão, V.; Tubino, M.; et al. Insights into Protein-Ionic Liquid Interactions Aiming at Macromolecule Delivery Systems. *J. Braz. Chem. Soc.* **2018**, *29*, 1983–

1998, doi:10.21577/0103-5053.20180141.

12. Zhang, S.; Sun, N.; He, X.; Lu, X.; Zhang, X. Physical Properties of Ionic Liquids: Database and Evaluation. *J. Phys. Chem. Ref. Data* **2006**, *35*, 1475–1517, doi:10.1063/1.2204959.

13. Zhou, L.; Tian, T.; Xiao, J.; Wang, T.; Yu, L. Aggregation behavior of pyrrolidinium-based surface active ionic liquids in H2O-EAN binary solvents. *J. Mol. Liq.* **2017**, *225*, 50–55, doi:10.1016/J.MOLLIQ.2016.10.142.

14. Singh, O.; Singla, P.; Aswal, V.K.; Mahajan, R.K. Aggregation and Morphological Aptitude of Drug-Based Ionic Liquids in Aqueous Solution. *ACS Omega* **2017**, *2*, 3296–3307, doi:10.1021/acsomega.7b00578.

15. Singla, P.; Singh, O.; Chabba, S.; Mahajan, R.K. Pluronic-SAILs (surface active ionic liquids) mixed micelles as efficient hydrophobic quercetin drug carriers. *J. Mol. Liq.* **2018**, *249*, 294–303, doi:10.1016/j.molliq.2017.11.044.

16. Bharmoria, P.; Kumar, A. Thermodynamic investigations of protein's behaviour with ionic liquids in aqueous medium studied by isothermal titration calorimetry. *Biochim. Biophys. Acta - Gen. Subj.* **2016**, *1860*, 1017–1025, doi:10.1016/J.BBAGEN.2015.08.022.

17. Geng, F.; Zheng, L.; Liu, J.; Yu, L.; Tung, C. Interactions between a surface active imidazolium ionic liquid and BSA. *Colloid Polym. Sci.* **2009**, *287*, 1253–1259, doi:10.1007/s00396-009-2085-1.

18. Pereiro, A.B.; Araújo, J.M.M.; Teixeira, F.S.; Marrucho, I.M.; Piñeiro, M.M.; Rebelo, L.P.N. Aggregation behavior and total miscibility of fluorinated ionic liquids in water. *Langmuir* **2015**, *31*, 1283–1295, doi:10.1021/la503961h.

19. Vieira, N.S.M.; Bastos, J.C.; Rebelo, L.P.N.; Matias, A.; Araújo, J.M.M.; Pereiro, A.B. Human cytotoxicity and octanol/water partition coefficients of fluorinated ionic liquids. *Chemosphere* **2019**, *216*, 576–586, doi:10.1016/j.chemosphere.2018.10.159.

20. Vieira, N.S.M.; Stolte, S.; Araújo, J.M.M.; Rebelo, L.P.N.; Pereiro, A.B.; Markiewicz, M. Acute Aquatic Toxicity and Biodegradability of Fluorinated Ionic Liquids. *ACS Sustain. Chem. Eng.* **2019**, *7*, 3733–3741, doi:10.1021/acssuschemeng.8b03653.

21. Alves, M.; Vieira, N.S.M.; Rebelo, L.P.N.; Araújo, J.M.M.; Pereiro, A.B.; Archer, M. Fluorinated ionic liquids for protein drug delivery systems: Investigating their impact on the structure and function of lysozyme. *Int. J. Pharm.* **2017**, *526*, 309–320, doi:10.1016/j.ijpharm.2017.05.002.

22. Bujacz, A. Structures of bovine, equine and leporine serum albumin. *Acta Crystallogr. Sect. D Biol. Crystallogr.* **2012**, *68*, 1278–1289, doi:10.1107/S0907444912027047.

23. Majorek, K.A.; Porebski, P.J.; Dayal, A.; Zimmerman, M.D.; Jablonska, K.; Stewart, A.J.; Chruszcz, M.; Minor, W. Structural and immunologic characterization of bovine, horse, and rabbit serum albumins. *Mol. Immunol.* **2012**, *52*, 174–182,

doi:10.1016/J.MOLIMM.2012.05.011.

24. Banipal, T.S.; Kaur, A.; Banipal, P.K. Physicochemical aspects of the energetics of binding of sulphanilic acid with bovine serum albumin. *Spectrochim. Acta - Part A Mol. Biomol. Spectrosc.* **2017**, *170*, 214–225, doi:10.1016/j.saa.2016.07.022.

25. Geng, F.; Zheng, L.; Yu, L.; Li, G.; Tung, C. Interaction of bovine serum albumin and long-chain imidazolium ionic liquid measured by fluorescence spectra and surface tension. *Process Biochem.* **2010**, *45*, 306–311, doi:10.1016/J.PROCBIO.2009.10.001.

26. Singh, T.; Bharmoria, P.; Morikawa, M.A.; Kimizuka, N.; Kumar, A. Ionic liquids induced structural changes of bovine serum albumin in aqueous media: A detailed physicochemical and spectroscopic study. *J. Phys. Chem. B* **2012**, *116*, 11924–11935, doi:10.1021/jp303609h.

27. Wang, X.; Liu, J.; Sun, L.; Yu, L.; Jiao, J.; Wang, R. Interaction of Bovine Serum Albumin with Ester-Functionalized Anionic Surface-Active Ionic Liquids in Aqueous Solution: A Detailed Physicochemical and Conformational Study. *J. Phys. Chem. B* **2012**, *116*, 12479–12488, doi:10.1021/jp307516a.

28. Banerjee, C.; Roy, A.; Kundu, N.; Banik, D.; Sarkar, N. A new strategy to prepare giant vesicles from surface active ionic liquids (SAILs): A study of protein dynamics in a crowded environment using a fluorescence correlation spectroscopic technique. *Phys. Chem. Chem. Phys.* **2016**, *18*, 14520–14530, doi:10.1039/c5cp07225e.

29. Thoppil, A.A.; Chennuri, B.K.; Gardas, R.L. Insights into the structural changes of bovine serum albumin in ethanolammonium laurate based surface active ionic liquids. *J. Mol. Liq.* **2019**, *290*, 111229, doi:10.1016/J.MOLLIQ.2019.111229.

30. Whitmore, L.; Wallace, B.A. Protein secondary structure analyses from circular dichroism spectroscopy: Methods and reference databases. *Biopolymers* **2008**, *89*, 392–400, doi:10.1002/bip.20853.

31. Andrade, M.A.A.; Chacón, P.; Merelo, J.J.J.; Morán, F. Evaluation of secondary structure of proteins from UV circular dichroism spectra using an unsupervised learning neural network. *Protein Eng. Des. Sel.* **1993**, *6*, 383–390, doi:10.1093/protein/6.4.383.

32. Borzova, V.A.; Markossian, K.A.; Chebotareva, N.A.; Kleymenov, S.Y.; Poliansky, N.B.; Muranov, K.O.; Stein-Margolina, V.A.; Shubin, V. V.; Markov, D.I.; Kurganov, B.I. Kinetics of Thermal Denaturation and Aggregation of Bovine Serum Albumin. *PLoS One* **2016**, *11*, e0153495, doi:10.1371/journal.pone.0153495.

33. Gill, P.; Moghadam, T.T.; Ranjbar, B. Differential scanning calorimetry techniques: applications in biology and nanoscience. *J. Biomol. Tech.* **2010**, *21*, 167–193.

34. Whitmore, L.; Wallace, B.A. DICHROWEB, an online server for protein secondary structure analyses from circular dichroism spectroscopic data. *Nucleic Acids Res.*

2004, *32*, W668–W673, doi:10.1093/nar/gkh371.

35. Ganguly, A.; Paul, B.K.; Ghosh, S.; Dalapati, S.; Guchhait, N. Interaction of a potential chloride channel blocker with a model transport protein: A spectroscopic and molecular docking investigation. *Phys. Chem. Chem. Phys.* **2014**, *16*, 8465–8475, doi:10.1039/c3cp53843e.

36. Chakraborty, T.; Chakraborty, I.; Moulik, S.P.; Ghosh, S. Physicochemical and conformational studies on BSA - Surfactant interaction in aqueous medium. *Langmuir* **2009**, *25*, 3062–3074, doi:10.1021/la803797x.

37. Li, Y.; Wang, X.; Wang, Y. Comparative studies on interactions of bovine serum albumin with cationic gemini and single-chain surfactants. *J. Phys. Chem. B* **2006**, *110*, 8499–8505, doi:10.1021/jp060532n.

38. Phillips, B.Y.J.N. THE ENERGETICS OF MICELLE FORMATION. **1954**.

39. Zana, R. Critical Micellization Concentration of Surfactants in Aqueous Solution and Free Energy of Micellization. **1996**, 1208–1211, doi:10.1021/la950691q.

40. Wang, J.; Wang, H.; Zhang, S.; Zhang, H.; Zhao, Y. Conductivities, volumes, fluorescence, and aggregation behavior of ionic liquids [C4mim][BF4] and [Cnmim]Br (n = 4, 6, 8, 10, 12) in aqueous solutions. *J. Phys. Chem. B* **2007**, *111*, 6181–6188, doi:10.1021/jp068798h.

CHAPTER IV

Studies on the interaction between model proteins and Fluorinated Ionic Liquids

Alves MMS contribution: Alves MMS, contributed to the work described in this chapter, in the conceptualization, performance of the experiments, data analysis and writing of the manuscript.

1. Abstract

Proteins are inherently unstable, which limits their use as therapeutic agents. However, the use of biocompatible cosolvents or surfactants can help to circumvent this problem through the stabilization of intramolecular and solvent mediated interactions. Ionic liquids (ILs) have been known to act as cosolvents or surface-active compounds. In the presence of proteins, ILs can assist in refolding, increasing shelf life, enhancing thermal stability, and improving enzymatic reaction rates. This potential for surfactant ILs to stabilize and encapsulate proteins has been previously studied, using lysozyme (Lys) and bovine serum albumin (BSA), which show great promise in the formulation of protein-based pharmaceuticals. In the work described herein, we used other techniques to improve our knowledge and understanding on how Lys and BSA interact with ILs. Small angle X-ray scattering (SAXS) experiments were prepared for both Lys and BSA, to describe the aggregates in solution. In order to comprehend Lys-FIL interactions, coarse grain molecular dynamics (CG-MD) simulations were performed. Finally, in an attempt to visualize the encapsulated protein, fluorescence microscopy assays were carried out. The results obtained allowed us to confirm protein stabilization and encapsulation, as well as bettercharacterize the surface interaction between these proteins and ILs.

2. Introduction

Proteins are highly complex biomolecules, which are present in several vital processes. In order to remain active, proteins must maintain their secondary structural elements, which are shaped through a delicate balance between hydrogen bonds, disulphide bridges, and hydrophobic and ionic interactions [1,2]. As a result of these interactions, native globular proteins are densely packed, which discourages non-specific aggregation [3]. Concomitantly, when the protein structure is destabilized, the exposure of the buried hydrophobic domains may lead to non-specific interactions. Although the interaction between proteins is essential for life, an abnormal increase in protein-protein interactions can lead to the unwanted formation of protein aggregates, which play major roles in diseases such as Alzheimer's, diabetes type 2 and spongiform encephalopathies [4]. This inherent structural and chemical instability, associated with short half-lives when subjected to physical and chemical stress, limits the use of proteins as therapeutic agents [5]. However, since proteins are stabilized by the equilibrium between intramolecular interactions and interactions with the solvent environment, the employment of biocompatible cosolvents can be an interesting strategy to preserve their stability [5].

Ionic liquids (ILs) are organic salts comprising ions that are liquid at room temperature [2]. ILs display low vapour pressures, low flammability, are thermodynamically stable and are generally recognized as safe starting materials [1,2]. These properties make ILs very desirable solvents in biocatalysis, extraction and electrochemistry, as they are able to solvate a broad range of organic substrates [6]. In the presence of proteins, ILs are known to act as cosolvents, with the ability to assist in refolding, increase shelf life, enhance thermal stability and improve enzymatic reaction rates [5]. The potential for ILs to stabilize and solubilize proteins demonstrates great promise in the formulation of protein-based biopharmaceuticals, since their use is still not widespread due to the aforementioned protein instability [2]. Surface-active ionic liquids (SAILs) in particular display an intrinsic amphiphilic nature due to the presence of long alkyl chains, and their characteristic aggregation behaviour enhances the permeability of drugs across biomembranes, acting as better drug carriers than conventional surfactants [2].

In previous works, we have studied the behaviour of model proteins lysozyme (Lys) and bovine serum albumin (BSA) in the presence of biocompatible, non-toxic SAILs [7,8]. We found that Lys was encapsulated by fluorinated ionic liquids (FILs, which belong to the

SAILs family), at concentrations above their critical aggregation concentration (*CAC*), with no significant impact on the protein stability and activity [7,9]. In contrast, the stability of BSA improved upon encapsulation by FILs, as shown by the increase in melting temperature (T_m) – verified by multiple thermostability assays –probably due to a more compact folding state, since protein α-helical content also increased in the presence of FIL [8].

In the work described herein, efforts were made to further understand how proteins interact with FILs. Small angle X-ray scattering (SAXS) experiments were prepared for both Lys and BSA, to describe the aggregates in solution. In order to comprehend Lys-FIL interactions, coarse grain molecular dynamics (CG-MD) simulations were performed, and, in an attempt to visualize the encapsulated protein, fluorescence microscopy assays were carried out.

3. Experimental procedures
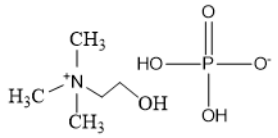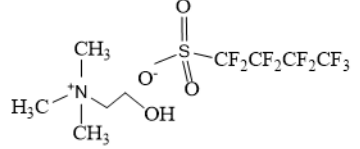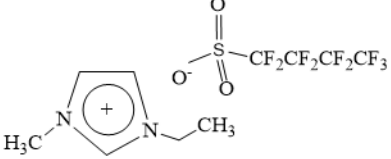
3.1 Materials

Lyophilized lysozyme from chicken egg white (L6876), lyophilized bovine serum albumin (A7030), potassium chloride, KCl (purity 99.0%, P9333) and potassium Phosphate Monobasic (purity 99.0 %, P0662) were purchased from Sigma-Aldrich; Potassium Phosphate Dibasic (purity 99.0 %, P749.3) and HEPES (4-(2-hydroxyethyl)-1-piperazineethanesulfonic acid) buffer (purity 99.5%, 9105) from Roth.

Cholinium ((2-hydroxyethyl)trimethylammonium) dihydrogen phosphate, $[N_{1112(OH)}][H_2PO_4]$ (> 98% mass fraction purity), cholinium perfluorobutanesulfonate, $[N_{1112(OH)}][C_4F_9SO_3]$ (> 97% mass fraction purity) and 1-ethyl-3-methylimidazolium perfluorobutanesulfonate, $[C_2C_1Im][C_4F_9SO_3]$ (> 97% mass fraction purity) were supplied by IoLiTec GmbH. To reduce the volatile chemicals and water contents, all ILs were dried under vacuum (3·10-2 Torr) with vigorous stirring at about 323 K for at least 2 days, immediately prior to their use. No further purification was carried out and the purity of all ILs was checked by ^{1}H and ^{19}F NMR. The chemical structures of the ionic liquids used in this work are presented in Table 4.1.

Fluorescent reagents Nile Red, NHS-Rhodamine and NHS-Fluorescein were purchased from Thermo Fisher Scientific.

Table 4.1. Chemical structures and acronyms of the ionic liquids (ILs) used in this work.

IL Designation	Chemical Structure	Critical Aggregation Concentration (CAC) in water
Cholinium dihydrogen phosphate $[N_{1112(OH)}][H_2PO_4]$		Non-surfactant
Cholinium perfluorobutanesulfonate $[N_{1112(OH)}][C_4F_9SO_3]$		16.07 mM (0.65% *v/v*) [9]
1-Ethyl-3-methylimidazolium perfluorobutanesulfonate $[C_2C_1Im][C_4F_9SO_3]$		14.55 mM (0.60% *v/v*) [9]

3.2 Protein purification

BSA monomers were isolated according to the protocol described in Section 3.2 of Chapter III.

3.3 Small Angle X-ray Scattering

SAXS data were collected at beamline P12 operated by EMBL Hamburg at the PETRA III storage ring (DESY, Hamburg, Germany) [10]. Measurements were performed under constant flow in batch mode. Protein concentrations were 3-4 mg·mL^{-1} for lysozyme (50 mM Tris HCl pH 7.5), and 5 mg·mL^{-1} for BSA (50 mM HEPES pH 7.5). Ionic liquid stock solutions were prepared at 50% *v/v*, in MilliQ water, and were then added in a concentration range from 0 to 1.8% *v/v* in the respective buffers. IL blanks were also measured. Images were recorded using a Pilatus-6M detector at a sample to detector distance of 3.0 m and λ = 0.12 nm, covering the range of momentum transfer $0.01 < s < 7$ nm^{-1} ($s = 4\pi\sin\theta/\lambda$, where 2θ is the scattering angle). Data were processed and analysed with the ATSAS program suite, version 3.0.3.1 (Hamburg, Germany) [11], using PRIMUS [12] for further subtraction and averaging as required and for radius of gyration (R_g) and other SAXS invariant estimations. The program OLIGOMER was used for equilibrium analysis of components in solution for BSA, with computed scattering intensities of components (PDB ID: 4F4S) calculated in FFMAKER [12].

3.4 Coarse Grained Molecular Dynamics

The Martini 3 CG model [13] was employed to simulate lysozyme in the presence and absence of FIL and for single proteins or in pairs. The GROMACS v2020 software [14] was used for simulation. CG protein structures and molecular topologies were obtained using the *martinize2* tool [15] and set up in boxes at a final protein/water ratio corresponding to approximately 3 mM for the single protein runs or 1.5 mM for the two-protein runs; 130 mM FIL was used.

Cholinium parameters were obtained from existing Martini 3 models. Perfluorobutanesulfonate was parameterized following the Martini 3 building block

approach, where a sulphate particle (or bead) was connected to two perfluoro beads (each covering two carbons) of type X1e — an addition in Martini 3 that better represents haloalkanes. Beads were constrained at a separation corresponding to their centre-of-mass distances when mapped on the fully extended atomic structure of perfluorobutanesulfonate (sulphate–perfluoro at 2.45Å and perfluoro–perfluoro at 2.8Å). Analogously to Martini 3 alkanes, the three beads were weakly restrained to 180º by a 50 kJ/mol cosine-harmonic potential.

Systems were solvated first with FIL (when used) in a randomly dispersed fashion around the protein(s), and then with copies of equilibrated Martini water boxes. 150 mM NaCl ionic strength was then added at this stage, with excess chloride ions to neutralize the protein's charge. Simulations employed a standard Martini timestep of 20 fs, with nonbonded interactions cut off at 1.1 nm. Reaction field electrostatics with a dielectric constant of 15 were used. Equilibration to 1 bar and 300 K was carried out over 10 ns using the Berendsen barostat[16], for its robustness, and the v-rescale thermostat [17]. Production runs employed the Parrinello-Rahman barostat [18]. Each system was run in triplicate from the equilibration step (when random velocities were assigned to particles) with individual production runs of at least 39 µs for the single-protein systems without FIL, 59 µs with FIL, and 83 µs for the two-protein systems with or without FIL (the total simulation time, over all replicas, was of 0.81 ms).

Trajectory analysis was done using the VMD v1.9.3 visualization software [19] as well as the NumPy [20] and MDAnalysis [21] Python packages. Structure clustering was done using the algorithm by Daura *et al.* [22]. To correctly cluster the cases of asymmetric dimers, trajectories were analysed duplicated, with protein identities switched in the duplicated segment.

3.5 Preparation of Nile Red-loaded micelles

Nile Red (NR) is an environment-sensitive stain, which becomes intensely fluorescent in lipid-rich or hydrophobic environments. Since it acts as a hydrophobic probe, NR has been used to study the local polarity of heterogeneous systems such as micelles and has also been found to fluoresce when combined with proteins bearing hydrophobic domains, as is the case of albumins [23,24].

The study of NR encapsulation into FIL micelles consisted in diluting a 1 mM NR stock solution to a final concentration of 10 µM in the presence of varying FIL concentrations, in PBS. These NR-FIL solutions were allowed to equilibrate overnight at RT. Dye absorbance was then measured using a NanoDrop One from 400 to 700 nm with subtraction of the blank buffer, and resulting data were extrapolated for 1 cm pathlength.

3.6 Protein labelling

Protein labelling was performed using N-hydroxysuccinimide (NHS)-ester fluorescent reagents, namely NHS-Rhodamine and NHS-Fluorescein, which react with primary amines to form stable amide bonds. Reactions were prepared according to the manufacturer's instructions. Briefly, the dye was dissolved in DMSO and added to lysozyme in phosphate buffer at 5:1 molar ratio. The solution was then incubated for 1 h at RT, and excess dye was removed using Fluorescent Dye Removal Columns (Thermo Fisher Scientific). After labelling, the protein was stored at 277 K prior to use, and protected from light. Dye and protein absorbance were quantified using a NanoDrop One.

3.7 Fluorescence Microscopy

Samples for fluorescence microscopy were applied to microscopy slides coated with 1.7% agarose and observed on a Leica DM 6000B microscope equipped with a phase contrast Uplan F1 100x objective and a CCD Andor Ixon camera (Andor Technologies). Images were acquired and analysed with bright field, Tx2 and FITC filters, according to fluorophore properties (see Table 4.2), using the Metamorph software suite (Molecular Devices).

Table 4.2. List of fluorophores and respective excitation and emission wavelengths.

	Ex/Em (nm)
Nile Red (NR)	552/635
NHS-Rhodamine (Rho)	552/575
NHS-Fluorescein (Fluo)	494/518

4. Results and Discussion

4.1 SAXS

SAXS allows for the analysis of the shape and size of biomolecules in solution, making it ideal to study dynamic systems such as protein-IL. However, we first had to ensure that the scattering density of the ILs would not interfere with further measurements, as can happen when conventional surfactants are used above their critical micelle concentration (*CMC*) [25]. Data were collected for $[N_{1112(OH)}][H_2PO_4]$, the non-surfactant IL, at 0.6, 1.2 and 1.8% *v/v* (see Figure 4.1). As expected, no assemblies were detected for this IL. Serial dilutions of the surfactant FILs were performed in the 0.16 to 5% *v/v* concentration range, in order to gage whether any of the concentrations would lead to the detection of stuctures. Scattering for $[N_{1112(OH)}][C_4F_9SO_3]$ remained unchanged up to 5% v/v, whereas $[C_2C_1Im][C_4F_9SO_3]$ at 5% *v/v* contributed strongly to the SAXS signal (Figure 4.1), although both FILs have been described to self-assemble into organized nanostructures above their critical aggregation concentration (*CAC*) [9]. As the SAXS signal for $[C_2C_1Im][C_4F_9SO_3]$ only occurs at high concentrations (8x *CAC*), which are well above the concentrations used in
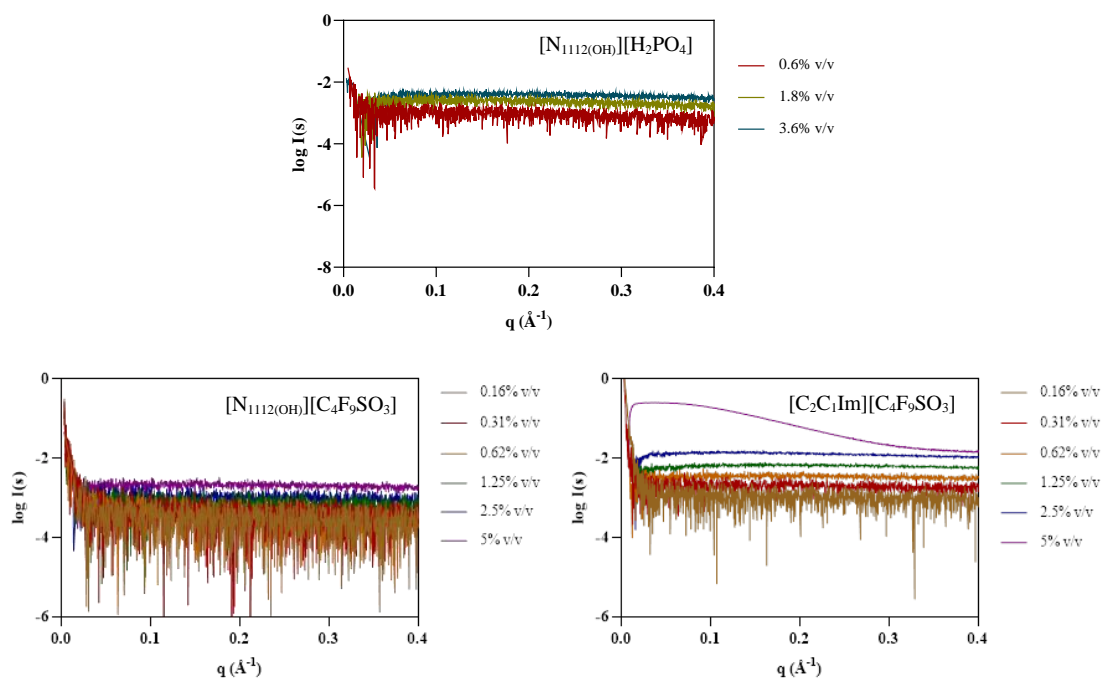
Figure 4.1. Experimental scattering curves for IL Blanks. $[N_{1112(OH)}][H_2PO_4]$ *(top)*, $[N_{1112(OH)}][C_4F_9SO_3]$ *(bottom left)* and $[C_2C_1Im][C_4F_9SO_3]$ *(bottom right)*.

our studies, its interference with protein measurements will not be significant. Nevertheless, all IL blank buffers were subtracted from their corresponding samples.

$[N_{1112(OH)}][H_2PO_4]$:

$[N_{1112(OH)}][C_4F_9SO_3]$:

$[C_2C_1Im][C_4F_9SO_3]$:

- Lys
- Lys + 0.3% v/v
- Lys + 0.6% v/v
- Lys + 1.2% v/v
- Lys + 1.8% v/v

Figure 4.2. Scaled experimental scattering curves *(left)* and dimensionless Kratky plots *(right)* for Lys in the presence of $[N_{1112(OH)}][H_2PO_4]$, $[N_{1112(OH)}][C_4F_9SO_3]$ and $[C_2C_1Im][C_4F_9SO_3]$.

Once the behaviour of the ILs had been established, data were collected for the model proteins, starting with lysozyme. The shape of the dimensionless Kratky plots (Figure 4.2, *right*) indicates that Lys maintains its globular folded structure. However, the peak shift observable in the presence of the ILs – which is even more apparent in the case of the FILs – suggests that some flexibility may have been introduced to the protein, which also justifies the increase in noise in the traces for both $[N_{1112(OH)}][C_4F_9SO_3]$ and $[C_2C_1Im][C_4F_9SO_3]$. All ILs led to an increase in average Lys particle size (see Table 4.3), which was overall more significant for the FILs. At 1.8% *v/v* $[N_{1112(OH)}][C_4F_9SO_3]$, the radius of gyration (R_g) increased by 22%, and maximum particle dimensions (D_{max}) 29%, while bo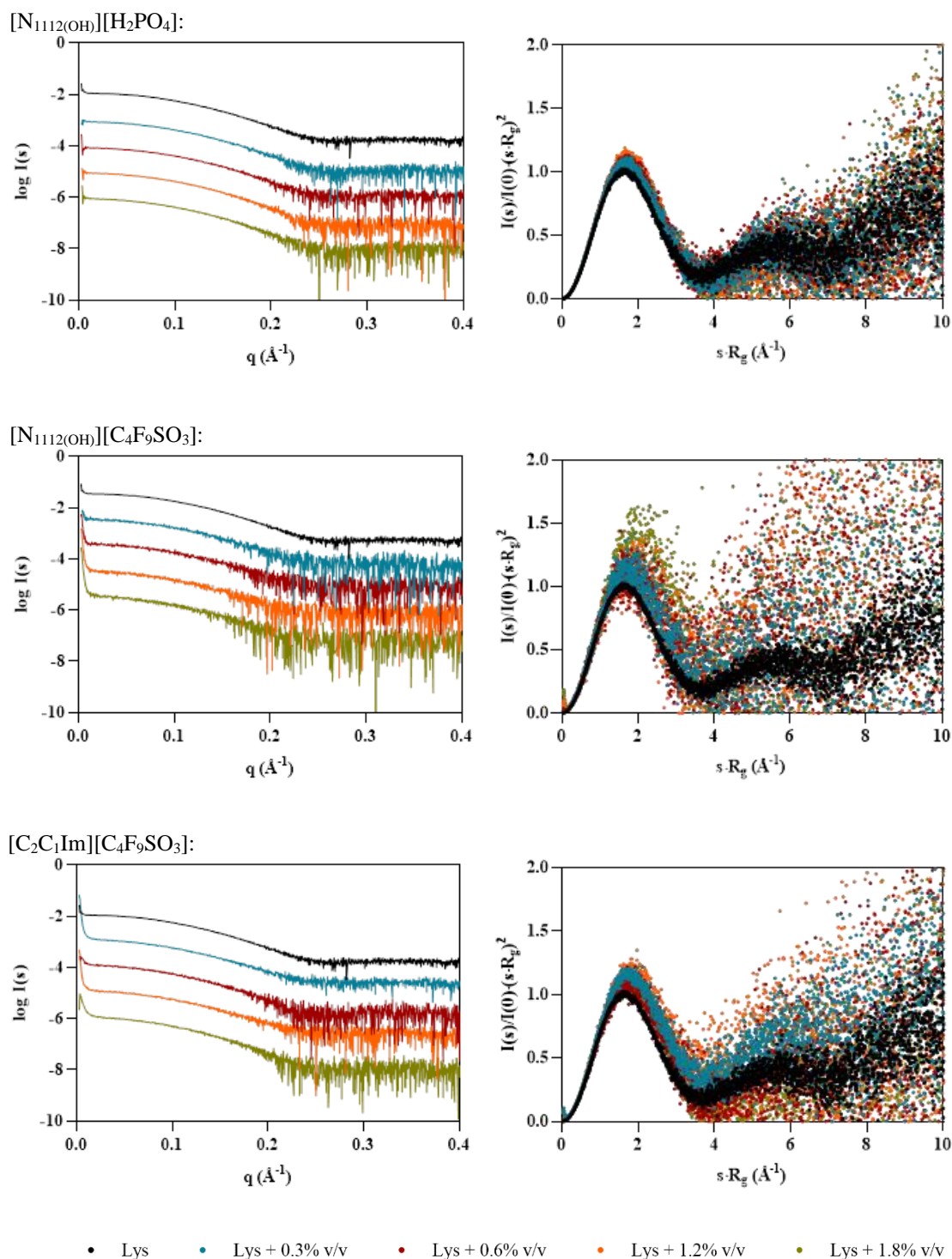th Porod volume (V_P) and molecular mass (MM) had a maximum increase of 22% in the presence of 1.8% *v/v* $[C_2C_1Im][C_4F_9SO_3]$.

Table 4.3. SAXS structural parameters of Lys in the presence and absence of ILs.

	R_g (Å)	V_P (Å³)	D_{max} (Å)	MM (kDa)
Lysozyme	14.4 ± 0.00	21,658	42.7	13.54
$[N_{1112(OH)}][H_2PO_4]$ (% *v/v*)				
0.3	14.8 ± 0.00	22,968	44.0	14.35
0.6	14.9 ± 0.01	23,033	46.8	14.40
1.2	15.1 ± 0.00	24,239	47.0	15.15
1.8	15.3 ± 0.01	25,188	48.8	15.74
$[N_{1112(OH)}][C_4F_9SO_3]$ (% *v/v*)				
0.3	15.4 ± 0.02	22,889	49.1	14.31
0.6	15.4 ± 0.02	22,966	53.0	14.35
1.2	15.7 ± 0.03	24,559	40.8	15.35
1.8	17.6 ± 0.03	23,404	55.0	14.63
$[C_2C_1Im][C_4F_9SO_3]$ (% *v/v*)				
0.3	15.3 ± 0.01	21,963	50.6	13.73
0.6	15.8 ± 0.01	25,171	51.0	15.73
1.2	15.7 ± 0.01	21,578	50.9	13.49
1.8	15.9 ± 0.01	26,523	51.3	16.58

Radii of gyration (R_g) were estimated from the Guinier approximation. Excluded particle volumes (V_P) were estimated from the Porod approximation. Maximum particle dimensions (D_{max}) were obtained from the pair-distribution function. Molecular mass (MM) values were derived from the Porod volume as MM = VP/1.6.

Interestingly, BSA displayed the opposite behaviour to Lys, with particles appearing to become smaller in the presence of the ILs (Table 4.4). At 1.8% *v/v* [C$_2$C$_1$Im][C$_4$F$_9$SO$_3$] all calculated structural parameters reached their minimum, with R_g, V_P, D_{max} and MM decreasing by 11, 20, 25 and 20%, respectively. These results corroborate our previous results, where we concluded that BSA became more compact in the presence of FILs [8]. The scattering curves for BSA (Figure 4.3, *left*) show that some inter-particle repulsions (downturn shape at low angles) are always present even in the absence of ILs, but become more pronounced with [C$_2$C$_1$Im][C$_4$F$_9$SO$_3$]. This behaviour indicates that the solution may be becoming partially ordered due to repulsive structure factors. The dimensionless Kratky plots (Figure 4.3, *right*) also reveal that BSA remains in a compact folded globular structure, but again displays the opposite behaviour to Lys, with a slight shift to the left.

Table 4.4. SAXS structural parameters of BSA in the presence and absence of ILs.

	R_g (Å)	V_P (Å^3)	D_{max} (Å)	MM (kDa)
BSA	29.5 ± 0.01	111,818	101.7	69.89
[N$_{1112(OH)}$][H$_2$PO$_4$] (% *v/v*)				
0.3	27.5 ± 0.02	98,843	82.4	61.78
0.6	27.0 ± 0.00	95,974	79.0	59.99
1.2	27.7 ± 0.00	97,216	85.1	60.76
1.8	28.0 ± 0.00	97,685	91.1	61.05
[N$_{1112(OH)}$][C$_4$F$_9$SO$_3$] (% *v/v*)				
0.3	26.4 ± 0.01	95,236	83.2	59.52
0.6	26.3 ± 0.01	93,533	81.4	58.46
1.2	26.5 ± 0.01	91,602	79.9	57.25
1.8	26.1 ± 0.01	90,896	78.5	56.81
[C$_2$C$_1$Im][C$_4$F$_9$SO$_3$] (% *v/v*)				
0.3	26.5 ± 0.01	93,024	79.9	58.14
0.6	26.4 ± 0.01	92,497	79.1	57.81
1.2	26.3 ± 0.01	90,556	78.8	56.60
1.8	26.3 ± 0.01	89,995	76.6	56.25

Radii of gyration (R_g) were estimated from the Guinier approximation. Excluded particle volumes (V_P) were estimated from the Porod approximation. Maximum particle dimensions (D_{max}) were obtained from the pair-distribution function. Molecular mass (MM) values were derived from the Porod volume as MM = VP/1.6.

[N$_{1112(OH)}$][H$_2$PO$_4$]:

[N$_{1112(OH)}$][C$_4$F$_9$SO$_3$]:

[C$_2$C$_1$Im][C$_4$F$_9$SO$_3$]:

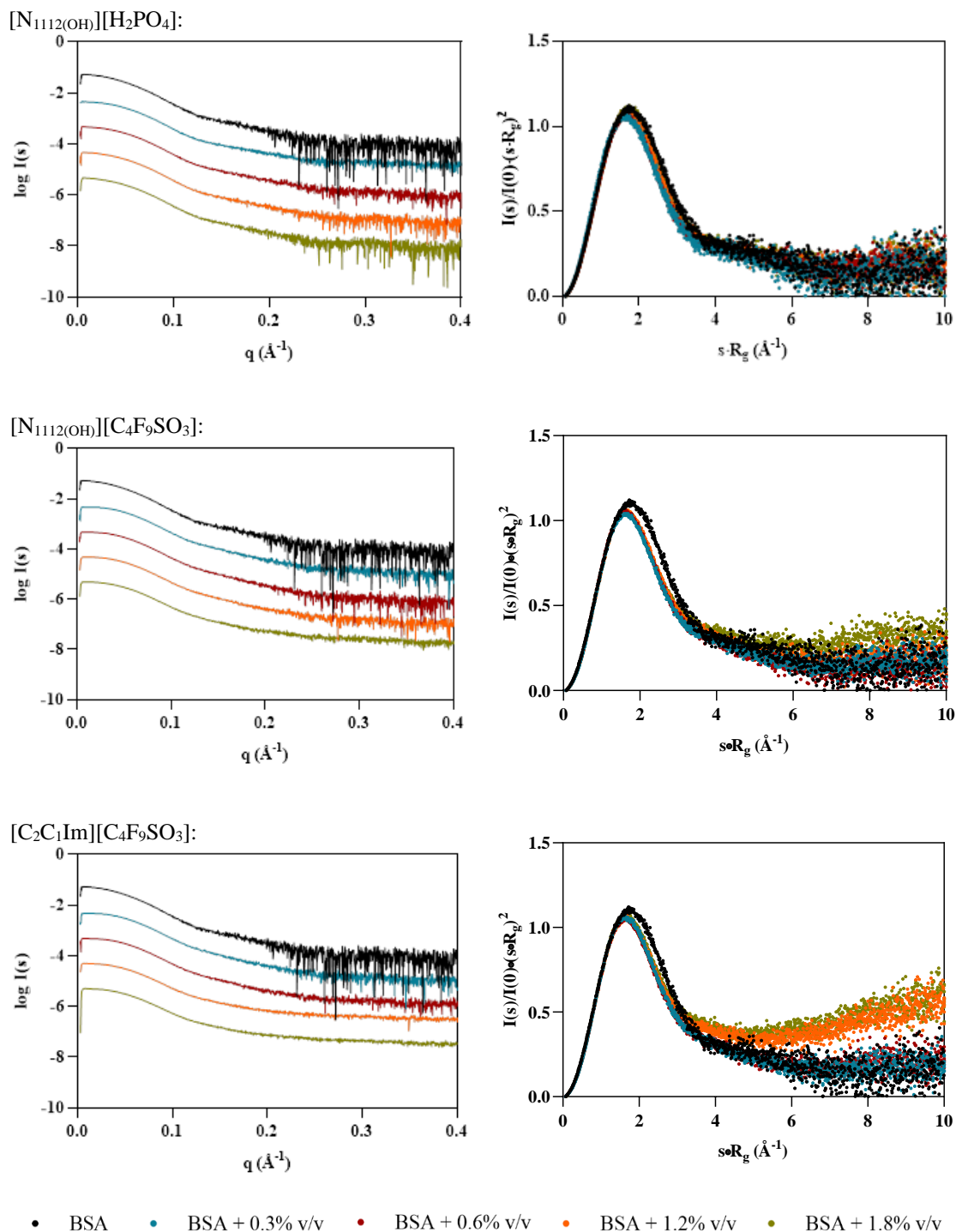- •   BSA   •   BSA + 0.3% v/v   •   BSA + 0.6% v/v   •   BSA + 1.2% v/v   •   BSA + 1.8% v/v

Figure 4.3. Scaled experimental scattering curves *(left)* and dimensionless Kratky plots *(right)* for BSA in the presence of [N$_{1112(OH)}$][H$_2$PO$_4$], [N$_{1112(OH)}$][C$_4$F$_9$SO$_3$] and [C$_2$C$_1$Im][C$_4$F$_9$SO$_3$].

Although the BSA samples used in these assays were monomeric fractions isolated after SEC, there were still concerns that some spontaneous dimerization could be biasing the results. In order to account for this possibility, the OLIGOMER software package was employed to analyse the oligomeric equilibrium in the different samples. Overall, the data is always described by 100% monomer, with no dimers present (Figure 4.4). In the presence of $[N_{1112(OH)}][H_2PO_4]$, the small differences between the scattering and the fit may be accounted for slight conformational rearrangements and/or changes in flexibility. For the FILs, the visible smearing out of the characteristic BSA minima at $0.12 - 0.13$ Å^{-1} supports possible structure compaction and increased flexibility/ conformational polydispersity.
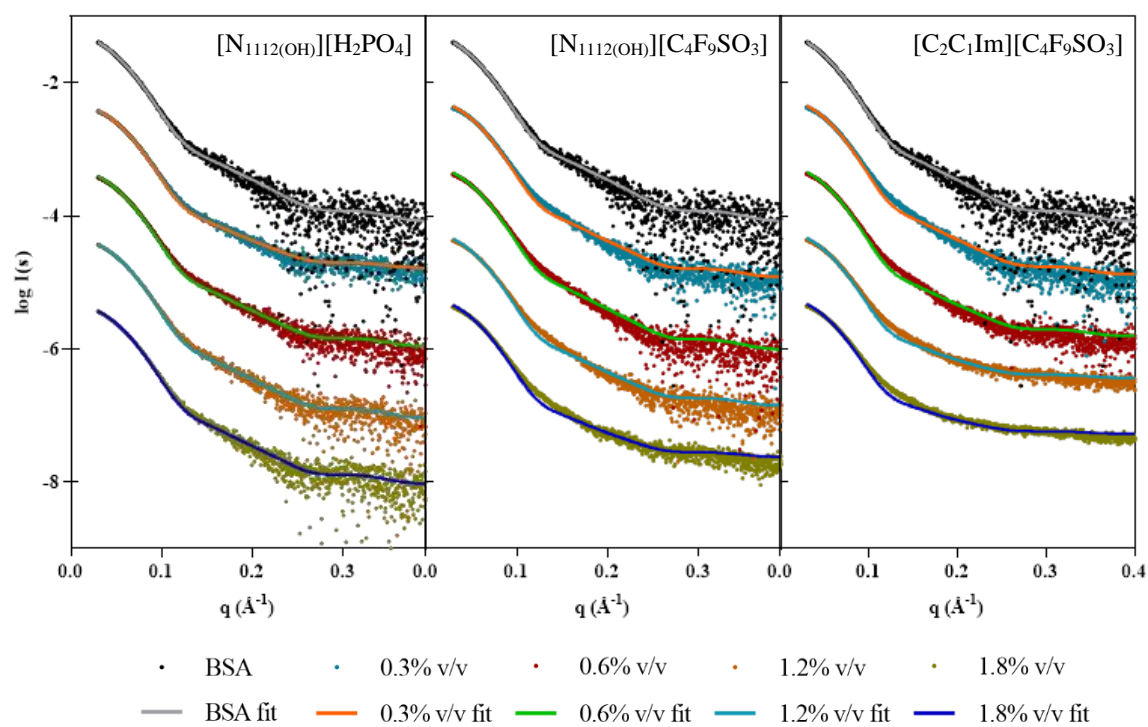
Figure 4.4. Scaled experimental scattering curves superimposed with fits obtained from OLIGOMER for BSA in the presence of $[N_{1112(OH)}][H_2PO_4]$, $[N_{1112(OH)}][C_4F_9SO_3]$ and $[C_2C_1Im][C_4F_9SO_3]$.

4.2 Molecular Dynamics

To characterize the interaction between $[N_{1112(OH)}][C_4F_9SO_3]$ and Lys, coarse-grain molecular dynamics (CG-MD) simulations were performed. Initially, the simulations consisted in only one Lys molecule in the presence of FIL. As can be seen in Figure 4.5c,

the amphipathic $[C_4F_9SO_3]^-$ anions self-assembled into micelles at the surface of the protein. These micelles interacted with both cationic and apolar residues and were able to occupy the substrate binding cleft (Figure 4.5d).

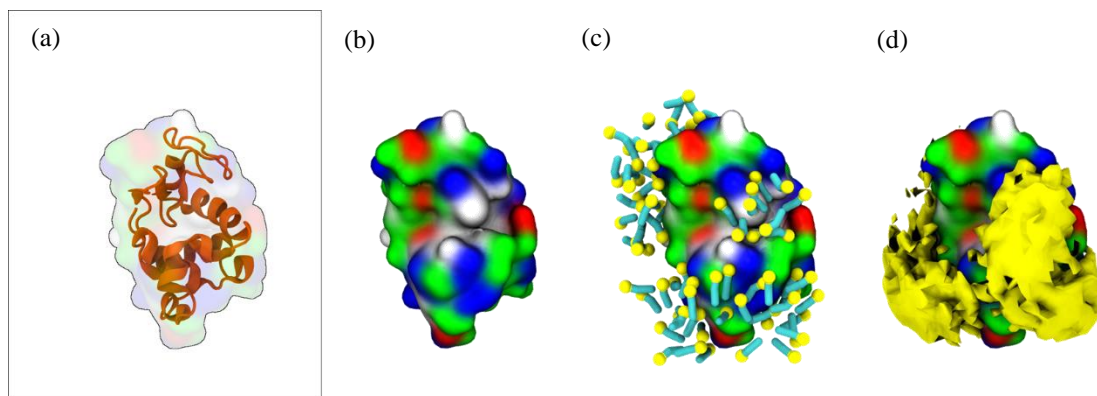**Figure 4.5.** MD simulations of interaction between Lys and $[N_{1112(OH)}][C_4F_9SO_3]$. (**a**) Atomistic structure of Lys (PDB ID:1DPX); (**b**) CG structure of Lys; (**c**) $[C_4F_9SO_3]^-$ micelles interacting with Lys surface (C_4F_9 – turquoise, SO_3 – yellow); (**d**) Micelle occupancy. Protein surface residues are represented as polar (green), apolar (white), cationic (blue), or anionic (red).

A second set of simulations was then carried out with two Lys molecules. In the absence of FIL, the two Lys molecules interact frequently, but always dissociated within the µs timescale (simulations were run too close to 100 µs due to these unbinding timescales). Such behaviour was in stark contrast to that when FIL was included. In the presence of $[N_{1112(OH)}][C_4F_9SO_3]$, the proteins came together and remained in contact for the entire length
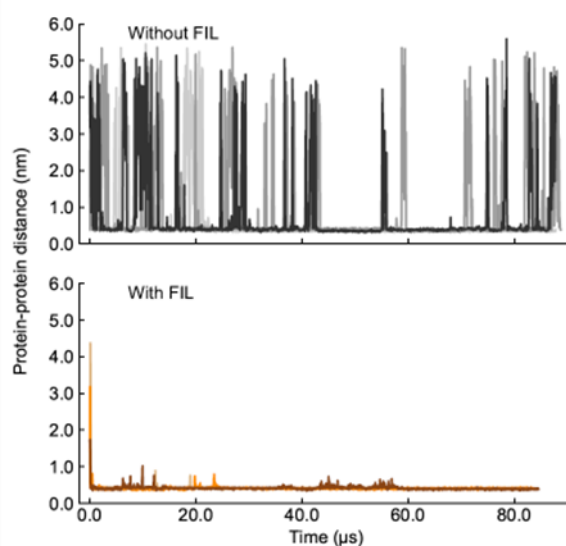

Figure 4.6. Lys-Lys contacts over time, in the absence (*top*) and presence (*bottom*) of $[N_{1112(OH)}][C_4F_9SO_3]$.

of the simulation, only separating to small extents and for brief periods to rearrange (Figure 4.6).

Further analysis into the contacts between both proteins reveals that the residues involved in the interactions are modulated by the presence of FIL (Figure 4.7). In the absence of FIL the residues engaged in longer Lys-Lys interactions are mainly 21-24 and 100-120. However, when $[N_{1112(OH)}][C_4F_9SO_3]$ is present, the interactions with residues 100-120 (which are mostly apolar) become longer lived, and residues 35-60 also become involved, even though this is mostly a polar region. Throughout the simulations with FIL, protein structures were similarity-clustered yielding four main Lys-Lys dimerization
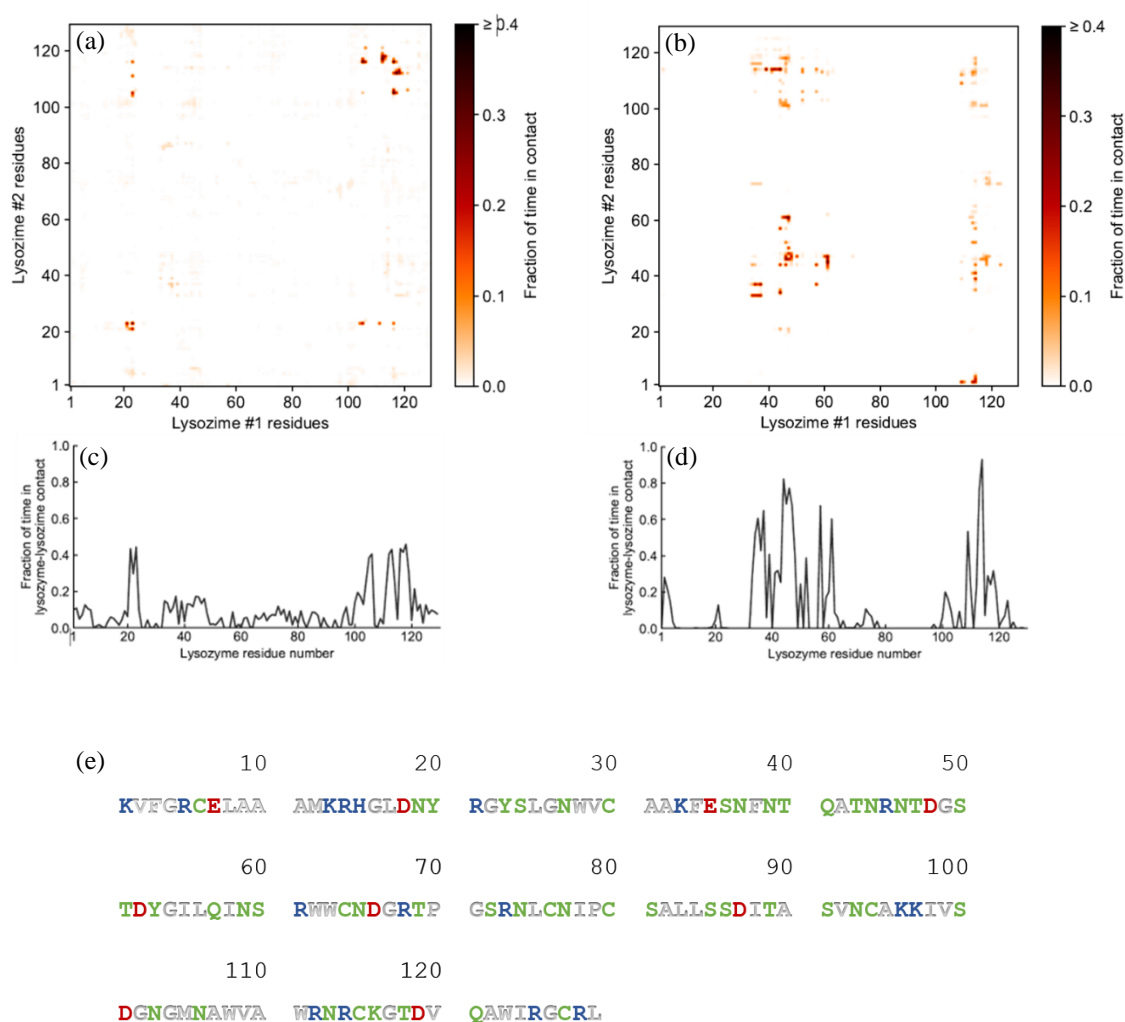

Figure 4.7. Lys-Lys interactions mediated by $[N_{1112(OH)}][C_4F_9SO_3]$. Heat maps of interaction between residues in the absence (**a**) and presence (**b**) of FIL, and corresponding duration of contacts (**c** and **d**). (**e**) Sequence for Lys (PDB ID: 1DPX). Residues are represented as polar (green), apolar (white), cationic (blue), or anionic (red).
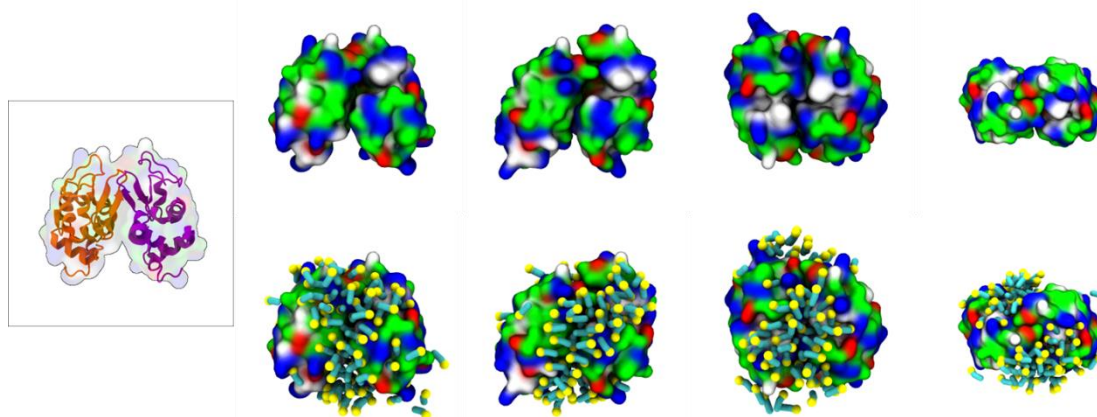
Figure 4.8. MD simulations of interaction between two Lys molecules and [N$_{1112(OH)}$][C$_4$F$_9$SO$_3$]. Atomistic structure of Lys-Lys (PDB ID:1DPX) (*left*); CG structures of Lys-Lys (*top*) and respective [C$_4$F$_9$SO$_3$]$^-$ micelle interactions. Protein surface residues are represented as polar (green), apolar (white), cationic (blue), or anionic (red).

configurations, with different protein orientations (Figure 4.8) and permanencies. These most common clusters were present for 24, 23, 10 and 7% of the simulation. Independently of how the proteins were oriented towards each other, FIL micelles were always present at the interface, mediating the aggregation. Anion micelle occupancy is represented in Figure 4.9, which corresponds to the interface of Lys-Lys interactions for at least 40% of the simulation (it is an interface common to more than one of the main clusters, hence the high occupancy). Interestingly, the contacts profile between [C$_4$F$_9$SO$_3$]$^-$ and Lys residues was not affected by dimerization (Figure 4.10), reinforcing the idea that the FIL interacts preferentially with specific residues on the protein surface, and is in turn responsible for mediating Lys-Lys aggregation.
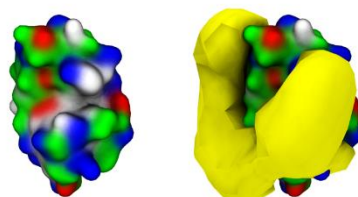
Figure 4.9. [C$_4$F$_9$SO$_3$]$^-$ micelle occupancy in Lys-Lys interface (only one Lys molecule represented for the sake of clarity).
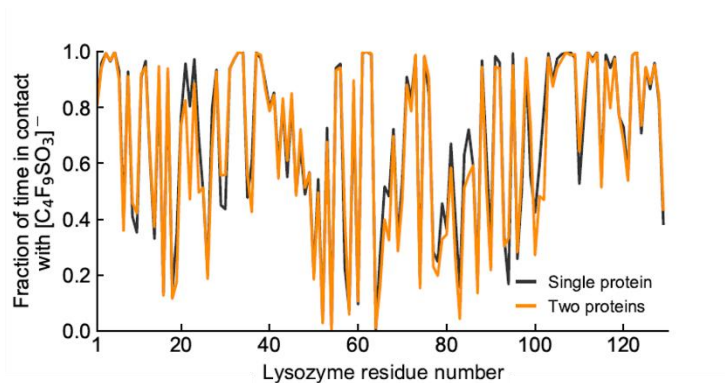
Figure 4.10. Duration of contacts between Lys residues and $[C_4F_9SO_3]^-$.

4.3 Fluorescence Microscopy

Fluorescence microscopy was used in an attempt to co-localize Lys within FIL micelles, using different fluorophores. Since tagging the FIL itself would likely lead to significant changes to its properties, we decided to use Nile Red (NR), an environment sensitive probe, to visualize the micelles. NR only fluoresces in hydrophobic environments, such as the core of micelles. NR was prepared in growing concentrations of $[C_2C_1Im][C_4F_9SO_3]$, from 0 to 10% *v/v*, and sample absorbance was measured at 552 nm. As can be seen in Figure 4.11, NR absorbance increased with FIL concentration, which has previously been described for conventional surfactants [24]. When more FIL is available, and consequently more micelles, a higher concentration of NR in the sample is able to absorb light at the characteristic wavelength. Observing these samples under the fluorescence microscope using the Tx2 filter confirmed these results (see Figure 4.12).
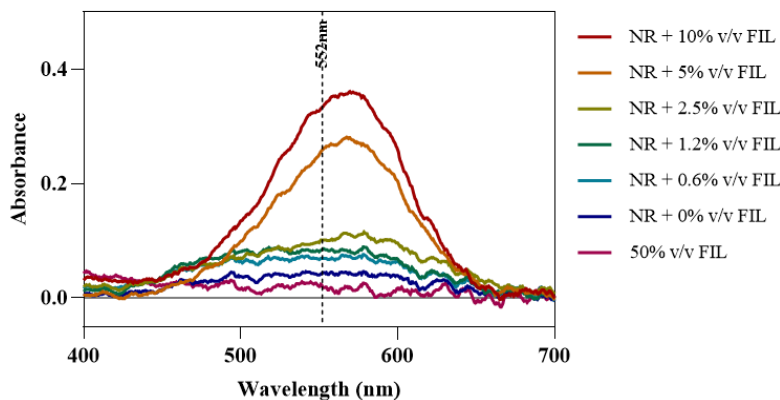
Figure 4.11. Nile Red absorbance spectra in the presence of increasing concentrations of $[C_2C_1Im][C_4F_9SO_3]$. Vertical line marks NR λ_{exc} (552 nm).

Although some fluorescence is detected in the absence of FIL, this may be expected due to the presence of trace amounts of DMSO. In the NR-FIL samples, we can observe a clear correlation between FIL concentration and the number and size of micelles. There are fewer (and smaller) micelles at 0.6% v/v $[C_2C_1Im][C_4F_9SO_3]$, which become larger and more frequent as FIL concentration increases.
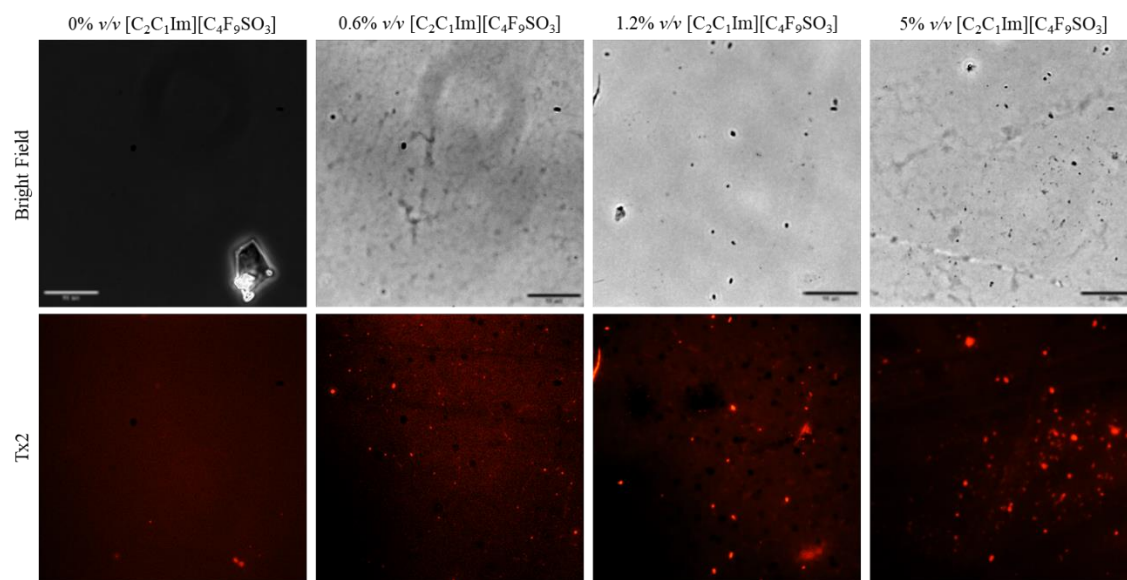

Figure 4.12. Fluorescence microscopy of Nile Red micelles at 0, 0.6, 1.2 and 5% v/v $[C_2C_1Im][C_4F_9SO_3]$. Scale bar corresponds to 10 µm.

Once FIL micelles have been visualized, lysozyme was tagged with NHS-Rhodamine (Rho) to shed some light on its behaviour at different $[C_2C_1Im][C_4F_9SO_3]$ concentrations. The absorbance of tagged Lys-Rho was measured (see Figure 4.13) to confirm the efficiency of the labelling reaction and ensure that the FIL did not absorb at the same wavelength. Fluorescence microscopy of these samples (Figure 4.14) detected non-specific Lys-Rho aggregates in the absence of FIL. At 1.2% v/v $[C_2C_1Im][C_4F_9SO_3]$, small individual particles can be observed, with some fluorescent background. This indicates that Lys-Rho has been encapsulated by the FIL (higher intensity), but not all the protein is contained within micelles, which explains the background signal. When FIL concentration is increased to 10% v/v, more particles appear, likely encapsulating Lys-Rho that was in excess at lower FIL concentrations. Counting the fluorescent particles from both samples revealed very similar size distributions, as presented in Figure 4.15. In total, fourteen images were analysed for 1.2% v/v FIL, with a total number of particles (n) of 1428, and nine images for 10% v/v FIL, where n = 3655. The increase in FIL led to the formation (and consequent detection) of 2.5x

more particles containing Lys-Rho. The most frequent particle size was in the 200 – 300 nm range, which accounted for 45 and 56% of total particles in the presence of 1.2 and 10% v/v $[C_2C_1Im][C_4F_9SO_3]$, respectively.
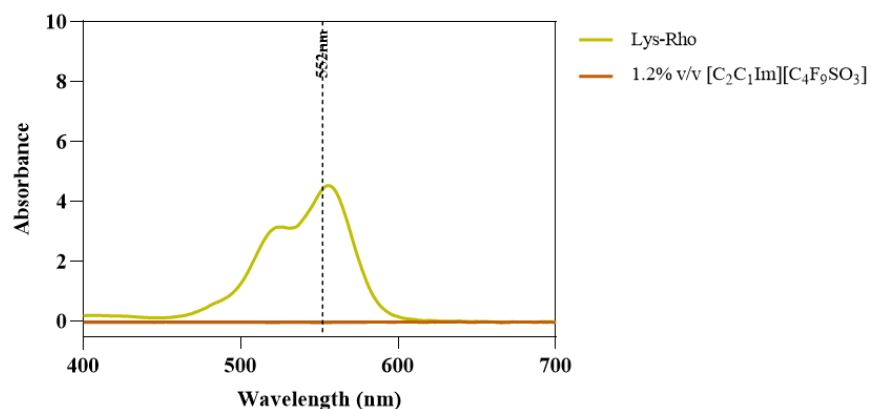
Figure 4.13. Lys-Rho absorbance spectra compared to 1.2% v/v $[C_2C_1Im][C_4F_9SO_3]$. Vertical line marks Rho λ_{exc} (552 nm).
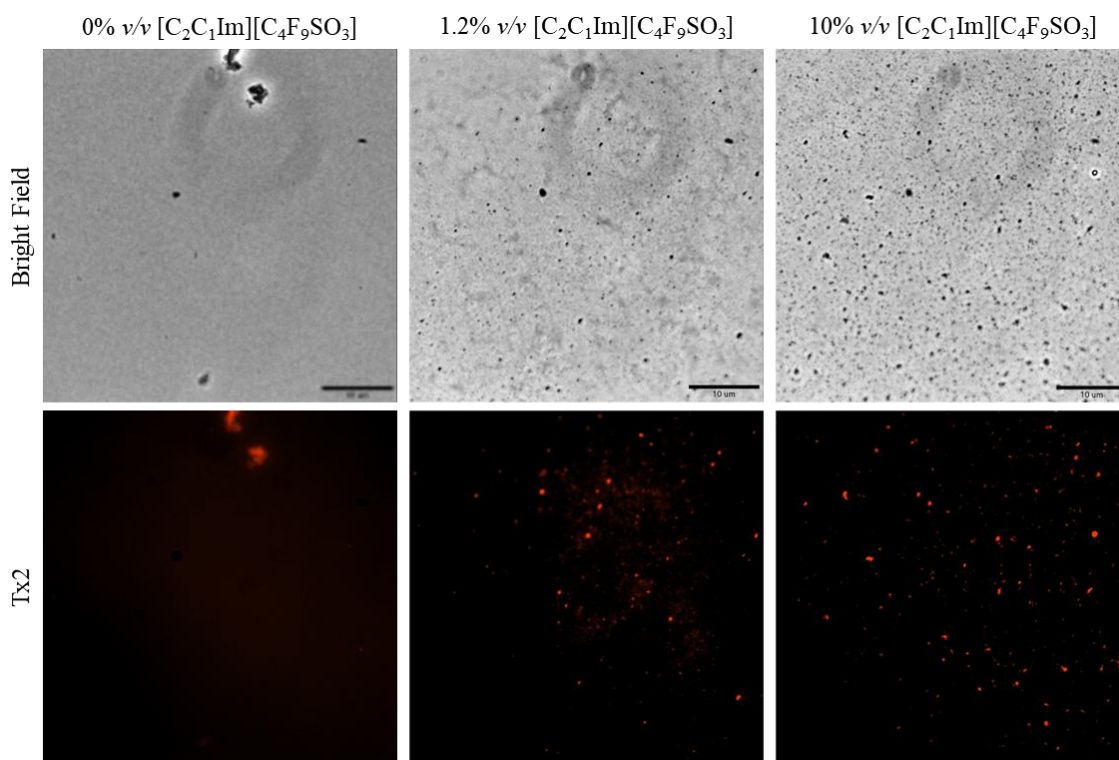
Figure 4.14. Fluorescence microscopy of Lys-Rho in the presence of 0, 1.2 and 10% v/v $[C_2C_1Im][C_4F_9SO_3]$. Scale bar corresponds to 10 μm.
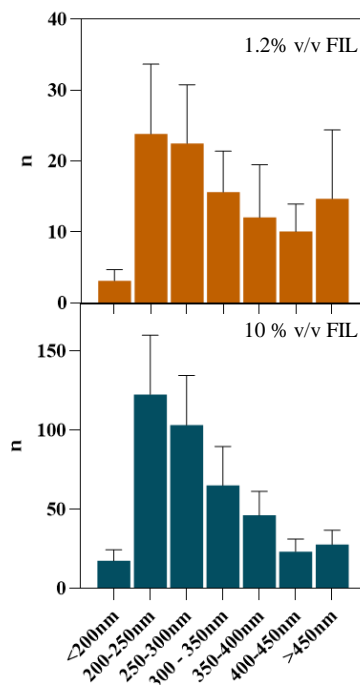
Figure 4.15. Size distribution of Lys-Rho in the presence of 1.2 and 10% *v/v* [C$_2$C$_1$Im][C$_4$F$_9$SO$_3$].

Lastly, lysozyme was tagged with NHS-Fluorescein (Lys-Fluo) instead of NHS-Rhodamine to allow for co-localization with NR, using the [N$_{1112(OH)}$][C$_4$F$_9$SO$_3$] FIL. Absorbance of all samples was measured once again to validate the experimental design (Figure 4.16). All samples containing Lys-Fluo absorbed light at 494nm, and only the samples prepared with NR showed absorbance at 552 nm. Fluorescence microscopy images were acquired using two different emission filters, Tx2 and FITC, which correspond to the NR and fluorescein wavelengths, respectively. As expected, FIL micelles were
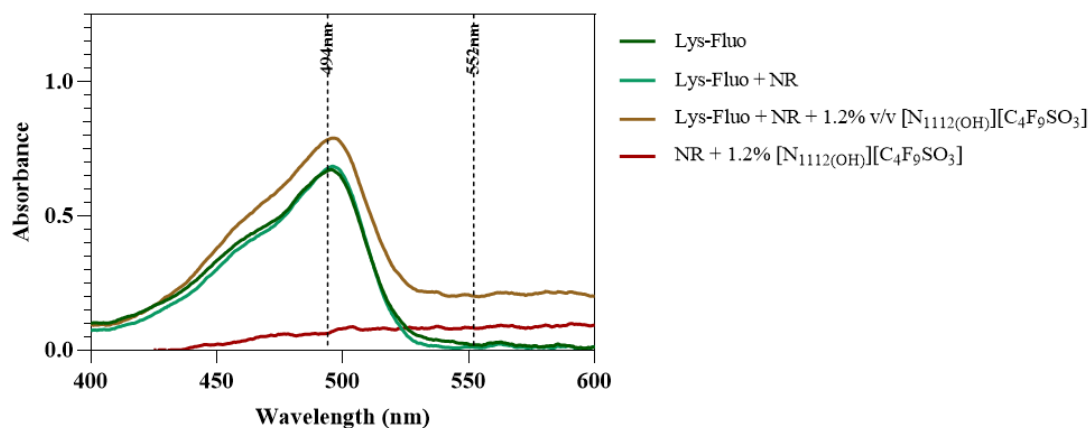
Figure 4.16. Absorbance spectra of Lys-Fluo + NR samples, in the presence of 0 and 1.2% *v/v* [N$_{1112(OH)}$][C$_4$F$_9$SO$_3$]. Vertical lines mark Fluo and NR λ$_{exc}$ (494 and 554 nm, respectively).

detected using the Tx2 filter, due to NR fluorescence in hydrophobic environments (Figure 4.17). Lys-Fluo particles were also identified under the FITC filter, with a similar appearance to what was previously described for Lys-Rho. Overlaying both fluorescence images allowed us to confirm the co-localization of both the FIL micelles and protein, indicating that Lys is
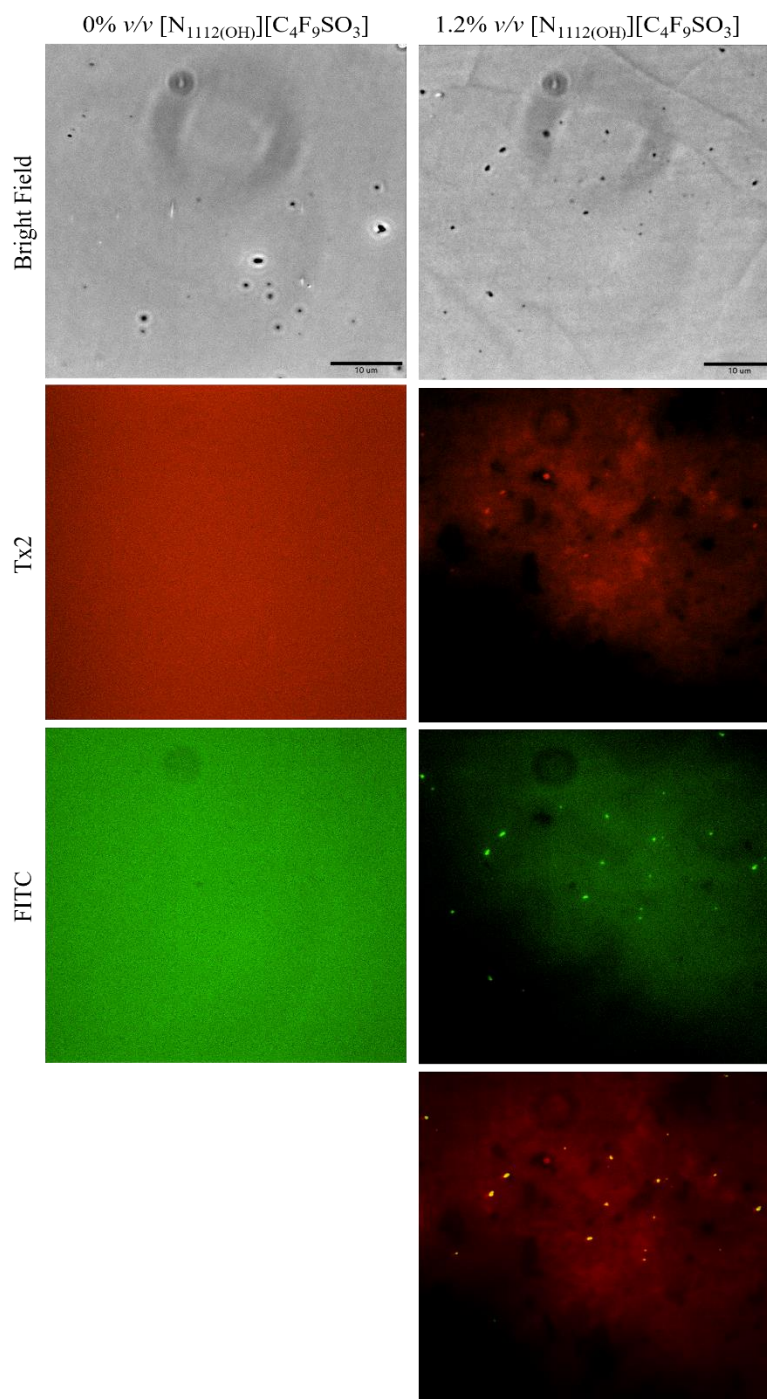
Figure 4.17. Fluorescence microscopy of Lys-Fluo + NR samples, in the presence of 1.2% *v/v* [N$_{1112(OH)}$][C$_4$F$_9$SO$_3$]. Scale bar represents 10 μm.

encapsulated by $[N_{1112(OH)}][C_4F_9SO_3]$. Although the overlayed images are not a perfect match in terms of the exact number of particles, this can be due to the presence of NR-micelles without protein, or micelles containing Lys-Fluo but not NR, which means that sample concentrations should be optimized.

5. Conclusions

The work presented herein further explores the interaction between FILs and model proteins Lys and BSA. IL characterization by SAXS revealed that although both surfactant FILs are known to self-assemble into nanostructures, these were not detected at the studied concentrations. Only [C_2C_1Im][$C_4F_9SO_3$] scattered X-rays, but at such high concentrations (8x CAC) that it did not hinder the use of this technique. In the presence of FILs, Lys was shown to maintain its globular folded structure, although some flexibility may have been introduced. Furthermore, at 1.8% v/v FIL, all Lys structural parameters had increased on average 24%. This behaviour contrasts with that of BSA. BSA particles grew smaller in the presence of FILs, with an average decrease of 19% for the same concentrations. This confirms the conclusions from our previous work [8], where thermostability and circular dichroism data indicated that BSA became more stable and compact with the addition of FILs.

CG-MD simulations were performed for systems containing Lys and [$N_{1112(OH)}$][$C_4F_9SO_3$] in order to better understand local molecular interactions. These showed [$C_4F_9SO_3$]$^-$ micelles assembling at the surface of the protein, interacting preferentially with cationic and apolar residues and occupying the binding cleft. However, since experimental data showed that Lys maintained (and even increased) its hydrolytic activity in the presence of FILs [7], we conclude that this interaction does not preclude the enzymatic reaction from being carried out. When two Lys molecules were present in the simulation box, FIL was shown to mediate their aggregation, being present at the interface of all configurations that were detected. Independently of the number of Lys molecules present, [$C_4F_9SO_3$]$^-$ always interacted with the same residues, mediating protein aggregation.

Fluorescence microscopy studies led to interesting new insights into FIL micelle formation. NR fluorescence, which is only detected in hydrophobic environments, was dependent on FIL concentrations, and the particles increased not only in number but also in size with higher FIL concentrations. In the presence of Lys-Rho, however, micelle size did not increase with FIL concentration. This suggests that micelle size is defined by the protein and not by the FIL available in solution. Tagging Lys with Fluo instead of Rho allowed for co-localization of the protein within FIL-NR micelles, confirming Lys encapsulation, as previously suggested [7].

The data presented in this chapter allowed us to not only confirm the previously reported effects of FILs on model proteins, but also to gain new insight into the formation of protein-FIL micelles.

6. References

1. Schröder, C. Proteins in Ionic Liquids: Current Status of Experiments and Simulations. *Top. Curr. Chem.* **2017**, *375*, doi:10.1007/s41061-017-0110-2.

2. Harada, L.; Pereira, J.; Campos, W.; Silva, E.; Moutinho, C.; Vila, M.; Oliveira Jr., J.; Teixeira, J.; Balcão, V.; Tubino, M.; et al. Insights into Protein-Ionic Liquid Interactions Aiming at Macromolecule Delivery Systems. *J. Braz. Chem. Soc.* **2018**, *29*, 1983–1998, doi:10.21577/0103-5053.20180141.

3. Molodenskiy, D.; Shirshin, E.; Tikhonova, T.; Gruzinov, A.; Peters, G.; Spinozzi, F. Thermally induced conformational changes and protein-protein interactions of bovine serum albumin in aqueous solution under different pH and ionic strengths as revealed by SAXS measurements. *Phys. Chem. Chem. Phys.* **2017**, *19*, 17143–17155, doi:10.1039/c6cp08809k.

4. Pillai, V.V.S.; Benedetto, A. Ionic liquids in protein amyloidogenesis: a brief screenshot of the state-of-the-art. *Biophys. Rev.* **2018**, *10*, 847–852, doi:10.1007/s12551-018-0425-4.

5. Sindhu, A.; Kumar, S.; Venkatesu, P. Contemporary Advancement of Cholinium-Based Ionic Liquids for Protein Stability and Long-Term Storage: Past, Present, and Future Outlook. *ACS Sustain. Chem. Eng.* **2022**, *10*, 4323–4344, doi:10.1021/acssuschemeng.1c08595.

6. Bui-Le, L.; Clarke, C.J.; Bröhl, A.; Brogan, A.P.S.; Arpino, J.A.J.; Polizzi, K.M.; Hallett, J.P. Revealing the complexity of ionic liquid–protein interactions through a multi-technique investigation. *Commun. Chem.* **2020**, *3*, 1–9, doi:10.1038/s42004-020-0302-5.

7. Alves, M.; Vieira, N.S.M.; Rebelo, L.P.N.; Araújo, J.M.M.; Pereiro, A.B.; Archer, M. Fluorinated ionic liquids for protein drug delivery systems: Investigating their impact on the structure and function of lysozyme. *Int. J. Pharm.* **2017**, *526*, 309–320, doi:10.1016/j.ijpharm.2017.05.002.

8. Alves, M.M.S.; Araújo, J.M.M.; Martins, I.C.; Pereiro, A.B.; Archer, M. Insights into the interaction of Bovine Serum Albumin with Surface-Active Ionic Liquids in aqueous solution. *J. Mol. Liq.* **2021**, *322*, 114537, doi:10.1016/j.molliq.2020.114537.

9. Pereiro, A.B.; Araújo, J.M.M.; Teixeira, F.S.; Marrucho, I.M.; Piñeiro, M.M.; Rebelo, L.P.N. Aggregation behavior and total miscibility of fluorinated ionic liquids in water. *Langmuir* **2015**, *31*, 1283–1295, doi:10.1021/la503961h.

10. Blanchet, C.E.; Spilotros, A.; Schwemmer, F.; Graewert, M.A.; Kikhney, A.; Jeffries, C.M.; Franke, D.; Mark, D.; Zengerle, R.; Cipriani, F.; et al. Versatile sample environments and automation for biological solution X-ray scattering experiments at the P12 beamline (PETRA III, DESY). *J. Appl. Crystallogr.* **2015**, *48*, 431–443, doi:10.1107/S160057671500254X.

11. Franke, D.; Petoukhov, M. V; Konarev, P. V; Panjkovich, A.; Tuukkanen, A.; Mertens, H.D.T.; Kikhney, A.G.; Hajizadeh, N.R.; Franklin, J.M.; Jeffries, C.M.; et al. ATSAS 2.8: a comprehensive data analysis suite for small-angle scattering from macromolecular solutions. *J. Appl. Crystallogr.* **2017**, *50*, 1212–1225, doi:10.1107/S1600576717007786.

12. Konarev, P. V; Volkov, V. V; Sokolova, A. V; Koch, M.H.J.; Svergun, D.I. PRIMUS: a Windows PC-based system for small-angle scattering data analysis. *J. Appl. Crystallogr.* **2003**, *36*, 1277–1282, doi:10.1107/S0021889803012779.

13. Souza, P.C.T.; Alessandri, R.; Barnoud, J.; Thallmair, S.; Faustino, I.; Grünewald, F.; Patmanidis, I.; Abdizadeh, H.; Bruininks, B.M.H.; Wassenaar, T.A.; et al. Martini 3: a general purpose force field for coarse-grained molecular dynamics. *Nat. Methods* **2021**, *18*, 382–388, doi:10.1038/s41592-021-01098-3.

14. Abraham, M.J.; Murtola, T.; Schulz, R.; Páll, S.; Smith, J.C.; Hess, B.; Lindahl, E. GROMACS: High performance molecular simulations through multi-level parallelism from laptops to supercomputers. *SoftwareX* **2015**, *1–2*, 19–25, doi:https://doi.org/10.1016/j.softx.2015.06.001.

15. martinize2 Available online: https://github.com/marrink-lab/vermouth-martinize.

16. Berendsen, H.J.C.C.; Postma, J.P.M.M.; van Gunsteren, W.F.; DiNola, A.; Haak, J.R. Molecular dynamics with coupling to an external bath. *J. Chem. Phys.* **1984**, *81*, 3684–3690, doi:10.1063/1.448118.

17. Bussi, G.; Donadio, D.; Parrinello, M. Canonical sampling through velocity rescaling. *J. Chem. Phys.* **2007**, *126*, doi:10.1063/1.2408420.

18. Parrinello, M.; Rahman, A. Polymorphic transitions in single crystals: A new molecular dynamics method. *J. Appl. Phys.* **1981**, *52*, 7182–7190, doi:10.1063/1.328693.

19. Humphrey, W.; Dalke, A.; Schulten, K. VMD: Visual molecular dynamics. *J. Mol. Graph.* **1996**, *14*, 33–38, doi:https://doi.org/10.1016/0263-7855(96)00018-5.

20. Harris, C.R.; Millman, K.J.; van der Walt, S.J.; Gommers, R.; Virtanen, P.; Cournapeau, D.; Wieser, E.; Taylor, J.; Berg, S.; Smith, N.J.; et al. Array programming with NumPy. *Nature* **2020**, *585*, 357–362, doi:10.1038/s41586-020-2649-2.

21. Gowers, R.J.; Linke, M.; Barnoud, J.; Reddy, T.; Melo, M.N.; Seyler, S.L.; Domanski, J.J.; Dotson, D.L.; Buchoux, S.; Kenney, I.M.; et al. MDAnalysis: A Python Package for the Rapid Analysis of Molecular Dynamics Simulations.; 2016.

22. Daura, X.; Gademann, K.; Jaun, B.; Seebach, D.; Van Gunsteren, W.F.; Mark, A.E. Peptide folding: When simulation meets experiment. *Angew. Chemie - Int. Ed.* **1999**, *38*, 236–240, doi:10.1002/(sici)1521-3773(19990115)38:1/2<236::aid-anie236>3.0.co;2-m.

23. Greenspan, P.; Fowler, S.D. Spectrofluorometric studies of the lipid probe, nile red. *J. Lipid Res.* **1985**, *26*, 781–789.

24. Kurniasih, I.N.; Liang, H.; Mohr, P.C.; Khot, G.; Rabe, J.P.; Mohr, A. Nile red dye in aqueous surfactant and micellar solution. *Langmuir* **2015**, *31*, 2639–2648, doi:10.1021/la504378m.

25. Berthaud, A.; Manzi, J.; Pérez, J.; Mangenot, S. Modeling detergent organization around aquaporin-0 using small-angle X-ray scattering. *J. Am. Chem. Soc.* **2012**, *134*, 10080–10088, doi:10.1021/ja301667n.

CHAPTER V

Impact of Fluorinated Ionic Liquids on Human Phenylalanine Hydroxylase – a potential Drug Delivery System

MMS Alves contribution to the work described in this chapter: MMS Alves, carried out the experiments, analysed the data and wrote the manuscript.

This chapter contains published data:

1. Abstract

Phenylketonuria (PKU) is an autosomal recessive disease caused by deficient activity of human phenylalanine hydroxylase (hPAH), which can lead to neurologic impairments in untreated patients. Although some therapies are already available for PKU, these are not without drawbacks. Enzyme-replacement therapy through the delivery of functional hPAH could be a promising strategy. In this work, biophysical methods were used to evaluate the potential of $[N_{1112(OH)}][C_4F_9SO_3]$, a biocompatible fluorinated ionic liquid (FIL), as a delivery system of hPAH. The results herein presented show that $[N_{1112(OH)}][C_4F_9SO_3]$ spontaneously forms micelles in a solution that can encapsulate hPAH. This FIL has no significant effect on the secondary structure of hPAH and is able to increase its enzymatic activity, despite the negative impact on protein thermostability. The influence of $[N_{1112(OH)}][C_4F_9SO_3]$ on the complex oligomerization equilibrium of hPAH was also assessed.

2. Introduction

Ionic Liquids (ILs) are salts comprised of an organic cation and inorganic anion, which present melting points close to 373.15 K. These molten salts present several physicochemical properties, such as viscosity, hydrophobicity, density, solubility, toxicity, and biodegradability, which can be easily tailored by modifying the functional group, anion, or cation [1]. Their versatility and tuneability allow targeted chemical structure design for the desired application. Thus, ILs show significant potential in the pharmaceutical field as enhancers of drug solubility, permeation, and stability, and as reaction media for organic and enzyme stabilization reactions, separations, and extractions [2–4]. ILs are also able to improve the stability and activity of proteins and enzymes [5,6]. Protein stability in ILs depends on the IL's structure and composition, protein surface composition and charge, specific anion/cation effects, and the aqueous environment [6,7]. The structural diversity present in both ILs and proteins suggests multiple and complex solvent–protein interactions [7].

IL surface activity can be increased by lengthening the alkyl chain, yielding surface-active ionic liquids (SAILs) [8,9]. SAILs are environmentally friendly surfactants [10], whose hydrophobicity can be tailored by adjusting the length of the alkyl chain, the type of head group, and the counterion. Therefore, the resulting aggregates, such as micelles, can be finely tuned to have the desired structure and dynamics. Because of their ability to enhance drug permeability across biomembranes and to substitute conventional surfactants in drug carriers, SAILs are very desirable to the pharmaceutical industry for protein formulation and delivery [11–13]. Furthermore, SAILs can substitute surfactants in protein preparations with commercial applications such as in cosmetics, detergents, and biochemical reactions [14].

Fluorinated ionic liquids (FILs) are SAILs whose alkyl chain contains a fluorous tag comprised of four or more carbon atoms that self-assemble into distinct structures depending on their concentration in solution [15]. These FILs have been shown to be biocompatible and non-toxic in four human cell lines [16] and in aquatic species with different levels of organization [17]. Moreover, the effect of these FILs on model proteins—lysozyme and bovine serum albumin (BSA)—has been evaluated [18,19]. Further studies are needed with therapeutic proteins to gain insights into their interactions with FILs and assess the potential use of these FILs as protein drug carriers.

In this work, we have selected human phenylalanine hydroxylase (hPAH), a potentially therapeutic enzyme with a molecular mass around 210 kDa and a more complex structural and functional mechanism than the previously studied proteins [18,19]. hPAH is a member of the aromatic amino acid hydroxylase family and catalyses the conversion of L-Phenylalanine (L-Phe) into L-Tyrosine (L-Tyr) in the liver using tetrahydrobiopterin (BH_4) and dioxygen as cofactors. Interestingly, besides being a substrate, L-Phe is also an allosteric regulator of hPAH. hPAH assembles as a tetramer (dimer of dimers) where each 52 kDa subunit contains three functional and structural domains: (1) the N-terminal regulatory domain; (2) the central catalytic domain, which contains the binding sites for substrate, iron, and cofactors (active site); and (3) the C-terminal oligomerization domain, which mediates the interaction between the two dimers [20–22]. Presently, ~1200 different mutations in the gene coding for hPAH (*PAH*) have been Identified that can affect protein expression, folding, catalysis, or regulation and lead to phenylketonuria (PKU). PKU is characterized by an increase in the concentration of circulating L-Phe (hyperphenylalaninemia), leading, in the central nervous system, to high levels of L-Phe and low concentrations of L-Tyr and L-Trp, the precursors of amine neurotransmitters.[23] Due to L-Phe neurotoxicity and neurotransmitters depletion, untreated patients may present severe psycho-motor delays [24]. The current treatments for PKU include lifelong dietary restrictions of L-Phe sources (dietetic approach) and pharmacological therapies such as supplementation with BH_4 (acting as a pharmacological chaperone) and enzyme substitution therapy with a pegylated form of the non-human enzyme phenylalanine ammonia lyase (PEG-PAL) [21,22,25]. Nevertheless, disadvantages have been described for all the available therapies [23]. The diet is problematic, unpalatable, and needs to be maintained through life, and thus non-compliance during adolescence and adulthood is a common cause of progressive neurodegeneration. Cofactor supplementation is limited to patients carrying BH_4-responsive genotypes, usually associated with mild *PAH* missense mutations, and immunogenic events have been described in patients undergoing PEG-PAL therapy. Delivery of functional hPAH (enzyme reposition therapy) to patients suffering from PKU would be an alternative and "universal" strategy to treat this disease, covering the full spectrum of *PAH* genotypes and avoiding the immunogenicity associated with the administration of a non-human enzyme.

Herein, we studied the interaction between hPAH and a biocompatible, choline-based SAIL, $[N_{1112(OH)}][C_4F_9SO_3]$, so proof of concept can be established to further develop a novel drug delivery system. Biophysical techniques have been used to assess the impact of this surfactant's IL on the activity, stability, and structure of hPAH, such as nano differential

scanning fluorimetry (nanoDSF), limited proteolysis, circular dichroism (CD), and small-angle X-ray scattering (SAXS). Furthermore, transmission electron microscopy (TEM) and dynamic light scattering (DLS) were used to evaluate protein encapsulation. This work aims to determine whether hPAH remains active, maintaining the necessary preactivation by the substrate after encapsulation by non-toxic, biocompatible $[N_{1112(OH)}][C_4F_9SO_3]$, supporting its use for biomedical applications.

3. Experimental procedures

3.1 hPAH Production

Recombinant full-length hPAH was produced in *Escherichia coli* Top10 cells transformed with pTrcHis-hPAH expression construct. hPAH is produced as a fusion protein with an N-terminal His_6-tag and a 26 amino acid linker.[26] Bacterial cells were grown in Luria–Bertani broth supplemented with 50 µg·mL^{-1} ampicillin, at 310.15 K and 220 rpm with continuous shaking. When OD_{600} was between 0.4 and 0.6, expression was induced by the addition of 1 mM isopropylthio-β-D-galactoside and 0.2 mM ferrous ammonium sulphate (Fe^{2+}). After 3 h at 310.15 K, cells were harvested (3000× *g*, 20 min, 277.15 K), and pellets were resuspended in Lysis Buffer (50 mM sodium phosphate pH 7.8, 300 mM NaCl, 10% glycerol) supplemented with 1 mM phenylmethylsulfonyl fluoride, DNaseI, and 1 mg·mL^{-1} lysozyme. Cells were then disrupted by sonication (Branson Sonifier 450D, Fisher Scientific, Waltham, MA, USA) in three cycles of 60 s at 50% amplitude, and the soluble fraction was recovered after centrifugation (13,000× *g*, 40 min, 277.15 K). The first purification step consisted of immobilized metal affinity chromatography. Ni-NTA resin (Qiagen GmbH, Hilden, Germany) was pre-equilibrated in lysis buffer supplemented with 10 mM imidazole, added to the cell lysate, and stirred for 1 h at 277.15 K. The resin was loaded onto a column and washed with increasing concentrations of imidazole (from 20 to 75 mM), and hPAH was
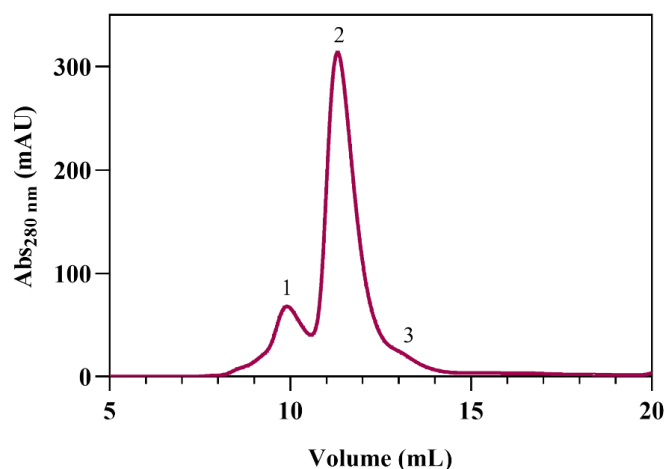

Figure 5.1. Size exclusion chromatography (SEC) profile of human phenylalanine hydroxylase (hPAH). Peak 1 corresponds to octameric form, peak 2 to tetramer (~220 kDa), and peak 3 to dimer. Apparent molecular masses were estimated using standard molecular masses as reference (not shown). Protein sample collected from peak 2 was used for the assays described in this manuscript.

eluted at 250 mM imidazole [27]. Size-exclusion chromatography (SEC) was performed using a Superdex 200 Increase 10/300 column (GE Healthcare, Chicago, IL, USA) in 20 mM HEPES pH 7.0, 200 mM NaCl (SEC buffer), at 277.15 K (see Figure 5.1). Isolated tetramers were flash-frozen and kept at 193.15 K until needed. All further assays were performed using SEC buffer unless otherwise stated.

3.2 Enzymatic Assays

The formation of L-Tyr by hPAH was measured as previously described[28] using a final reaction volume of 200 µL. The reaction mix to follow the activity of hPAH in its preactivated condition was set up using 5 µg His_6-hPAH, 1 mM L-Phe, 0.1 mg·mL^{-1} catalase, and 0–2% *v/v* cholinium perfluorobutanesulfonate, $[N_{1112(OH)}][C_4F_9SO_3]$ (>97% mass fraction purity; Figure 5.2) supplied by IoLiTec GmbH, Heilbronn, Germany, and incubated for 4 min at 298.15 K. A total of 100 µM Fe^{2+} was added and further incubated for 1 min at 298.15 K. The reaction was initiated with 75 µM BH_4 and stopped after 1 min with the addition of 200 µL of cold 2% *v/v* acetic acid/ethanol solution. The reaction to study non-activated hPAH activity was set up similarly, but the substrate L-Phe (1 mM) was added simultaneously with BH_4. The amount of L-Tyr produced was quantified by HPLC using a Symmetry C18 (5 µm) column (Waters Corporation, Milford, MA, USA), a 10% ethanol mobile phase pumped at 1 mL·min^{-1}, and fluorimetric detection (λ_{exc} = 274 nm and λ_{em} = 304 nm). Adequate controls were always performed to exclude the presence of possible interferents. Specific activities are presented as the mean ± standard deviation (SD) of triplicate experiments and expressed in nmol of L-Tyr produced during 1 min per mg of hPAH (nmol L-Tyr·min^{-1}·mg^{-1}).
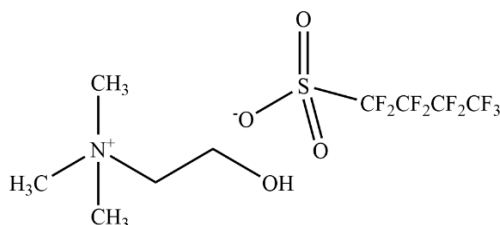

Figure 5.2. Chemical structure of cholinium perfluorobutanesulfonate, $[N_{1112(OH)}][C_4F_9SO_3]$.

3.3 Nano Differential Scanning Fluorimetry

Experiments of nanoDSF were performed on a Prometheus NT.48 instrument (NanoTemper Technologies GmbH, München, Germany). Protein intrinsic fluorescence was recorded at wavelengths (λ) of 330 and 350 nm as the temperature increased from 293.15 to 363.15 K at a rate of 1 K·min^{-1}. Samples of 0.25 mg·mL^{-1} hPAH with increasing concentrations of FIL (from 0 to 2% *v/v*) and 1 mM L-Phe were loaded into Prometheus Capillaries (NanoTemper Technologies GmbH, München, Germany). Melting temperatures (T_m) were calculated from the minimum of the first derivative. The T_m values in the presence of [N$_{1112(OH)}$][C$_4$F$_9$SO$_3$] were compared to those obtained in the absence of FIL to calculate ΔT_m. In addition, to monitor the effect of L-Phe on the stability of the regulatory and catalytic domains, T_m values in the presence of 1 mM L-Phe were compared with those obtained in its absence (ΔT_mL-Phe) for each condition.

3.4 Limited Proteolysis

hPAH was incubated for 10 min at 298.15 K in the absence or presence of 0.6% *v/v* [N$_{1112(OH)}$][C$_4$F$_9$SO$_3$] and/or L-Phe 1 mM. Trypsin was added at 1:200 mass ratio trypsin:hPAH at 298.15 K in SEC Buffer. At each time point, an aliquot was collected, and leupeptin (trypsin:leupeptin mass ratio of 1:1.5) was added to stop the reaction, followed by the addition of 4x loading buffer and sample denaturation at 368.15 K for 5 min. SDS-PAGE was used to assess the proteolytic profile. Samples were loaded into 4–12% Bis-Tris precast gels (Thermo Fisher Scientific, Waltham, MA, USA) and ran with 1× NuPAGE MES Running Buffer (Thermo Fisher Scientific, Waltham, MA, USA) at 190 V. Relative density of the bands was quantified with ImageJ 1.53e (NIH, Bethesda, MD, USA)[29] and fitted to a two-phase exponential decay equation using GraphPad Prism 8 (GraphPad Software Inc, San Diego, CA, USA).

3.5 Circular Dichroism

A JASCO J-815 spectropolarimeter (JASCO Inc., Tokyo, Japan) was used to record CD spectra at 293.15 K with a quartz cuvette of 0.1 cm path length. Samples were prepared in 20 mM Tris HCl, 50 mM KCl, pH 7.5, to avoid interference from HEPES buffer with

measurements in the far-UV. Samples of hPAH at final concentration of 0.2 mg·mL^{-1} were incubated with 0 to 2% *v/v* of [N$_{1112(OH)}$][C$_4$F$_9$SO$_3$] for at least 10 min at room temperature. CD spectra were acquired from 190 to 260 nm at scan speeds of 50 nm·min^{-1} with 5 accumulations and a response time of 1 s. Spectral deconvolution was carried out with Dichroweb, using the K2D algorithm [30–32].

3.6 Blue Native Polyacrylamide Gel Electrophoresis

Samples containing hPAH and 0–1.2% *v/v* [N$_{1112(OH)}$][C$_4$F$_9$SO$_3$] were prepared and analyzed using a blue native polyacrylamide gel electrophoresis-based system (BN-PAGE) from Thermo Fisher Scientific (Waltham, MA, USA). The samples were loaded onto a NativePAGE 4–16% Bis-Tris gel with molecular weight marker NativeMark Unstained Protein Standard (Thermo Fisher Scientific, Waltham, MA, USA), and the electrophoresis was run according to manufacturer's guidelines. Relative band density was analysed using ImageJ software 1.53e (NIH, Bethesda, MD, USA) [29].

3.7 Small Angle X-ray Scattering

SAXS data were collected at beamline P12 operated by EMBL Hamburg at the PETRA III storage ring (DESY, Hamburg, Germany) [33]. Measurements were performed under constant flow in batch mode using a protein concentration of 0.9 mg·mL^{-1} in SEC Buffer, containing 0–1.2% *v/v* [N$_{1112(OH)}$][C$_4$F$_9$SO$_3$] and in the absence and presence of L-Phe (final concentration of 1 mM). Images were recorded using a Pilatus-6M detector at a sample to detector distance of 3.0 m and $\lambda = 0.12$ nm, covering the range of momentum transfer $0.01 < s < 7$ nm^{-1} ($s = 4\pi\sin\theta/\lambda$, where 2θ is the scattering angle). Data were processed and analysed with the ATSAS program suite, version 3.0.3.1 (Hamburg, Germany) [34], using PRIMUS [35] for further subtraction and averaging as required and for radius of gyration (R_g) and other SAXS invariant estimations. The program OLIGOMER was used for equilibrium analysis of volume fractions of components in solution, with computed scattering intensities of components (PDB ID: 5FII and 2PAH) calculated in FFMAKER [35].

3.8 Dynamic Light Scattering

DLS measurements were performed on a Zetasizer Nano Series ZEN3600 (Malvern Instruments, Malvern, UK) apparatus equipped with a 633 nm laser using a non-invasive back-scattering technique (173°) for detection. A 10% *v/v* stock solution of $[N_{1112(OH)}][C_4F_9SO_3]$ in MilliQ water was prepared and filtered prior to use (Millex PVDF filters, 0.22 μm), and hPAH was diluted to final concentration of 0.2 $mg \cdot mL^{-1}$. Samples were equilibrated for 30 min at room temperature prior to measuring. A 30 μL aliquot of each sample was loaded into a Hellma Quartz Cell QS 3.00 mm and measured 3 times. Cell temperature was kept constant at 298.15 K.

3.9 Transmission Electron Microscopy

Solutions containing 0.2 $mg \cdot mL^{-1}$ hPAH and 1.2% *v/v* $[N_{1112(OH)}][C_4F_9SO_3]$ were pipetted on a 200 mesh copper grid (3 mm diameter) and left to air dry. Excess sample was then removed using filter paper. The grids were imaged at MicroLab-IST (Lisbon, Portugal) in a Hitachi 8100 model with LaB6 filament at a working voltage of 200 kV.

3.10 Statistical Analysis

Experimental data were analysed with GraphPad Prism 8.0 (GraphPad Software, San Diego, CA, USA) using one-way ANOVA followed by Dunnet test when appropriate. The differences were considered significant when $p < 0.005$.

4. Results and Discussion

4.1 Stability and Function of hPAH

The activity of hPAH, which measures the conversion of L-Phe into L-Tyr after BH_4 addition, was 6095 ± 372 nmol Tyr·min^{-1}·mg^{-1} upon previous incubation with L-Phe and 1317 ± 117 nmol L-Tyr·min^{-1}·mg^{-1} without L-Phe, corresponding to an increase of 4.6*x* upon L-Phe preactivation (Table 5.1). As L-Phe is both an allosteric activator and substrate of hPAH, the kinetic behavior of the enzyme depends on the order of addition of the reaction components, where pre-incubation with L-Phe yields higher rates of L-Tyr production [22,36].

Table 5.1. Catalytic activity of non-activated and preactivated hPAH in the absence and presence of increasing concentrations of $[N_{1112(OH)}][C_4F_9SO_3]$.

$[N_{1112(OH)}][C_4F_9SO_3]$ (% *v/v*)	hPAH Activity (nmol Tyr·min^{-1}·mg^{-1})		L-Phe Activation Ratio
	L-Phe Preactivation (1 mM L-Phe)	No L-Phe Preactivation	
0	6095 ± 372	1317 ± 117	4.6
0.3	6643 ± 14	1643 ± 28 *	4
0.6	6966 ± 60 *	2075 ± 131 *	3.4
1.2	6861 ± 339 *	2178 ± 43 *	3.2
2	6104 ± 298	2011 ± 176 *	3

Data are shown as mean ± SD of triplicate assays. (*) Significant statistical differences.

The presence of $[N_{1112(OH)}][C_4F_9SO_3]$ at different concentrations, above and below its critical aggregation concentration (*CAC*) of 0.6% *v/v* [15], shows a growing positive impact in the enzymatic activity of hPAH (see Figure 5.3 and Table 5.1), followed by a slight decrease at 2% FIL. The addition of this FIL at 0.6–1.2% *v/v* increased the activity rates of hPAH preactivated with L-Phe up to 13–14%, in contrast to 58–65% for the non-activated enzyme. This pronounced effect suggests that $[N_{1112(OH)}][C_4F_9SO_3]$ may preactivate hPAH to some extent in the absence of L-Phe, thus contributing to higher activity rates. As the

concentration of $[N_{1112(OH)}][C_4F_9SO_3]$ increases, the L-Phe activation ratio decreases, mainly due to the higher hPAH activity in the basal state (non-preactivated).
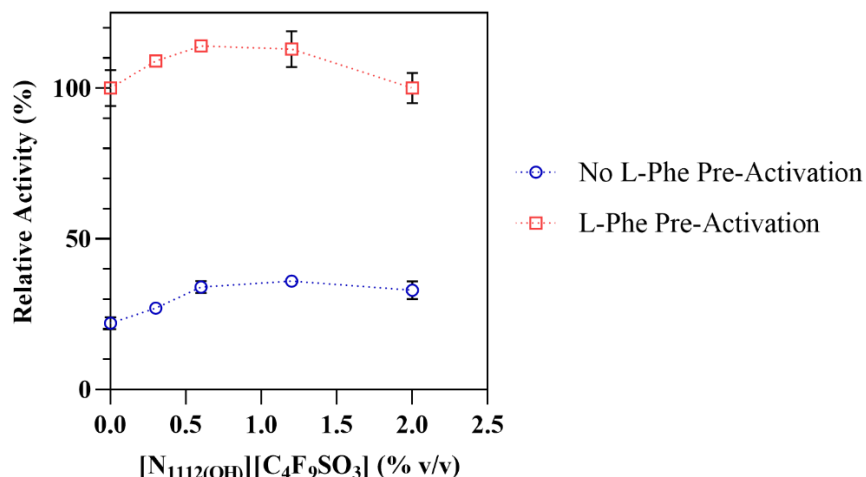
Figure 5.3. Relative activities of hPAH as a function of $[N_{1112(OH)}][C_4F_9SO_3]$ concentrations. Relative enzymatic activity of non-activated and L-Phe activated hPAH. The activity of the hPAH in the absence of $[N_{1112(OH)}][C_4F_9SO_3]$ in the preactivated assay (1 mM L-Phe) was considered as 100%. Data are shown as mean ± SD of triplicate assays.

The thermal denaturation profile of hPAH, as monitored by nanoDSF, displays two transitions around 320 and 329 K, known to correspond to its regulatory (T_{m1}) and catalytic (T_{m2}) domains, respectively (see Figure 5.4 and Table 5.2). Pre-incubation with 1 mM L-Phe shifts these transitions to higher temperatures (T_{m1} ~328 K, T_{m2} ~331 K), thus showing a stabilizing effect (ΔT_mL-Phe: 7.5 and 2 K, respectively), in agreement with previous reports [21,22].
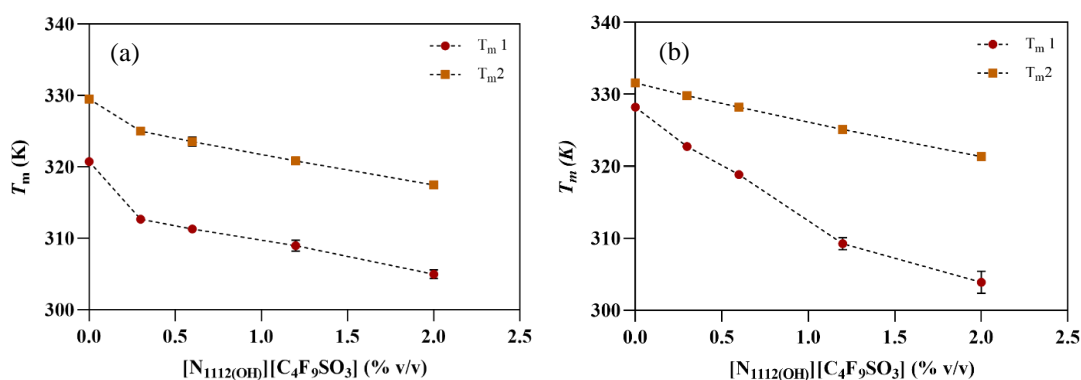
Figure 5.4. Thermostability of hPAH in the absence and presence of increasing concentrations of $[N_{1112(OH)}][C_4F_9SO_3]$. T_m values obtained from nanoDSF for hPAH (a) in the absence and (b) presence of 1 mM L-Phe. Data are shown as mean ± SD of triplicate assays.

The addition of $[N_{1112(OH)}][C_4F_9SO_3]$ to the protein has a detrimental effect on the thermostability of hPAH, which is more significant on the regulatory domain (ΔT_{m1} from −8.1 to −15.8 K) than on the catalytic domain (ΔT_{m2} from −4.53 to −12.04 K), as can be seen in Figure 5.3. The presence of L-Phe (1 mM) helps to smooth the protein's thermal destabilization of the regulatory domain by the FIL up to 0.6% (see Figure 5.5), after which ΔT_{m1} increases to −18.99 and −24.34 K. The presence of L-Phe also smooths the decrease in T_{m2} in the presence of FIL, as ΔT_{m2} from −1.75 to −10.23 K were determined. However, when compared to the response of hPAH to L-Phe in the absence of FIL (ΔT_{m1}L-Phe 7.5 K and ΔT_{m2}L-Phe 2 K), higher ΔT_{m1}L-Phe and ΔT_{m2}L-Phe were observed for FIL concentrations of 0.3 and 0.6% (10.06 and 7.51 K) and 0.3–2% (4.82–3.85 K), respectively.

Table 5.2. Variation of hPAH melting temperatures (T_m) measured by nanoDSF.

$[N_{1112(OH)}][C_4F_9SO_3]$ (% v/v)	ΔT_m (-L-Phe)		ΔT_m (+L-Phe)		ΔT_mL-Phe	
	ΔT_{m1}	ΔT_{m2}	ΔT_{m1}	ΔT_{m2}	ΔT_{m1} L-Phe	ΔT_{m2} L-Phe
0	-	-	-	-	7.5	2
0.3	-8.1	-4.5	-5.5	-1.8	10.1	4.8
0.6	-9.4	-6	-9.4	-3.3	7.5	4.7
1.2	-11.8	-8.7	-19	-6.5	0.25	4.3
2	-15.8	-12	-24.3	-10.2	-1.1	3.8

ΔT_m–T_m variation in the presence of $[N_{1112(OH)}][C_4F_9SO_3]$ compared to those in its absence;
ΔT_mL-Phe–T_m variation in the presence versus absence of 1 mM L-Phe.

In the absence of L-Phe, $[N_{1112(OH)}][C_4F_9SO_3]$ destabilizes hPAH with a more significant effect on the regulatory domain. This destabilization may leave the catalytic domain more accessible to the substrate, leading to an increase in the activity rate of non-activated hPAH when compared to the control hPAH (0% FIL). The presence of FIL allows the protein to respond to the presence of L-Phe either at the functional and structural level, probably by an effect on the catalytic domain. Indeed, in the presence of different concentrations of FIL, the enzyme activity is 13–14% higher than the control value (6095 nmol Tyr·min^{-1}·mg^{-1}), correlating with the increase in the ΔT_{m2}L-Phe observed for the tested concentrations.
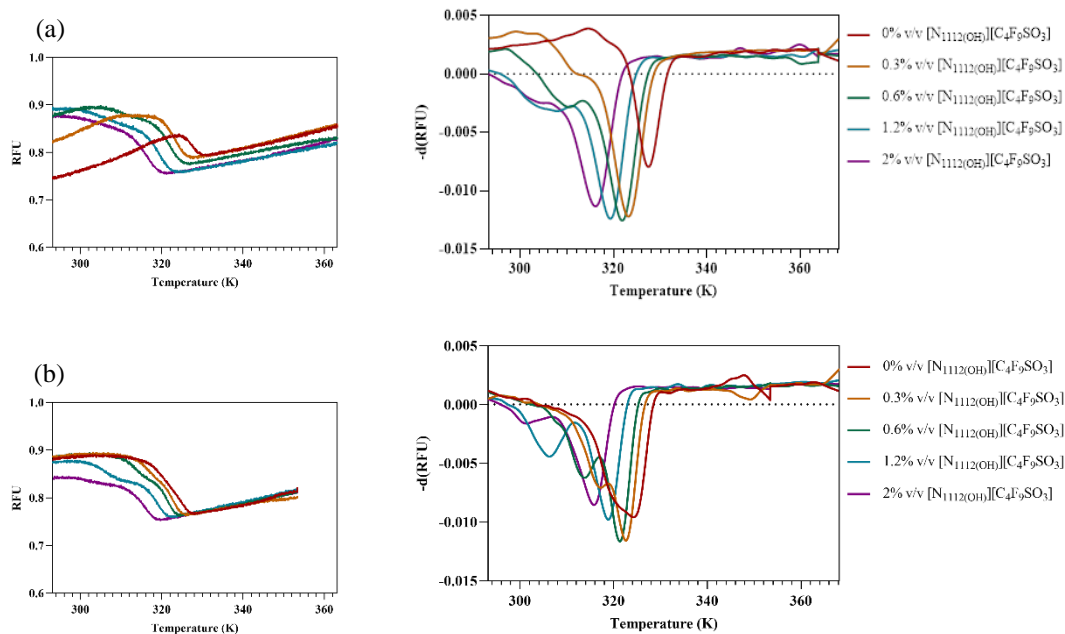
Figure 5.5. Nano Differential Scanning Fluorimetry spectra *(left)* and first derivative *(right)* for hPAH + 0 – 2% *v/v* [$N_{1112(OH)}$][$C_4F_9SO_3$] in the **(a)** absence or **(b)** presence of 1 mM L-Phe. Data represent the mean of three independent experiments, and error bars are not shown for clarity.
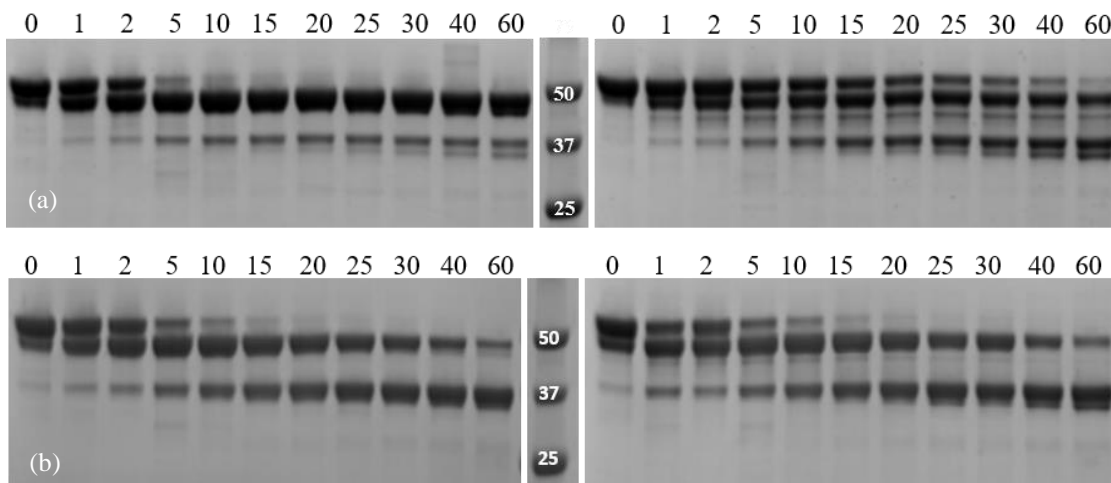
Figure 5.6. SDS-PAGE analysis of hPAH limited proteolysis. Trypsin was added at 1:200 mass ratio trypsin:hPAH and aliquots were withdrawn at different time points (0 to 60 min). (a) hPAH *(left)* and hPAH + 0.6% *v/v* [$N_{1112(OH)}$][$C_4F_9SO_3$] *(right)*. (b) hPAH + 1 mM L-Phe *(left)* and hPAH + 1 mM L-Phe + 0.6% *v/v* [$N_{1112(OH)}$][$C_4F_9SO_3$]. Each lane corresponds to a time point of the assay, as indicated above the gels (min).

hPAH limited proteolysis by trypsin was followed in the presence of 0.6% *v/v* FIL, since hPAH in the preactivated state showed higher enzymatic activity at this concentration (see Figure 5.5). The resulting SDS-PAGE (Figure 5.6) and corresponding proteolysis graph (Figure 5.7) demonstrate that the presence of $[N_{1112(OH)}][C_4F_9SO_3]$ resulted in a 6x slower digestion rate. It has been described that decreased proteolytic rates can be due to higher protein compactness or to a lesser mobile protein conformation [22]. In addition, in the specific case of hPAH, higher resistance to proteolysis has also been associated with the movement of the regulatory domain, protecting the C-terminal region of this domain from trypsin digestion and leaving the catalytic domain more accessible to the substrate (high-activity state) [37], which seems to be the case when taking into consideration the activity and thermostability data. In addition, limited access of trypsin to the protein target sequences due to the presence of FIL may be excluded since the addition of L-Phe to the assay leads to a ~5x faster digestion rate (see Table 5.3). Under these conditions (1 mM L-Phe; 0.6% *v/v* of $[N_{1112(OH)}][C_4F_9SO_3]$), the hPAH proteolytic profile approaches the profile obtained for hPAH without L-Phe and $[N_{1112(OH)}][C_4F_9SO_3]$, correlating with the similar T_{m1} and T_{m2} obtained for these conditions, namely 320.77 ± 0.02 and 329.53 ± 0.03 K (absence of L-Phe and $[N_{1112(OH)}][C_4F_9SO_3]$) and 318.85 ± 0.07 and 328.23 ± 0.02 K (1mM L-Phe: 0.6% *v/v* $[N_{1112(OH)}][C_4F_9SO_3]$). These data may indicate similar conformational states.
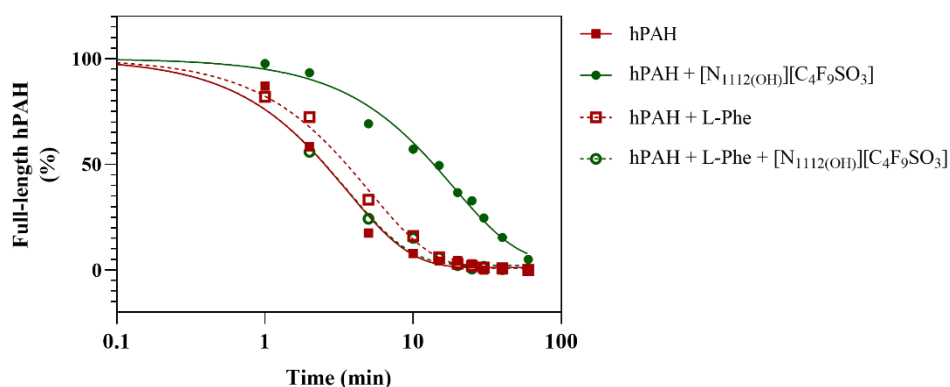
Figure 5.7. Limited proteolysis of hPAH by trypsin. Degradation of full-length hPAH by trypsin, in the absence and presence of $[N_{1112(OH)}][C_4F_9SO_3]$ and/or L-Phe.

Table 5.3. Effect of L-Phe on the proteolytic stability of hPAH in the presence and absence of $[N_{1112(OH)}][C_4F_9SO_3]$ and L-Phe.

$[N_{1112(OH)}][C_4F_9SO_3]$ (% *v/v*)	K_{obs} (min^{-1})	
	No L-Phe	1 mM L-Phe
0	0.279	0.197
0.6	0.053	0.281

Proteolytic rates (k_{obs}) were obtained from limited trypsin proteolysis.

4.2 Effect of FIL on hPAH Structure

CD spectrum of hPAH presents two broad minima at 208 and 222 nm (see Figure 5.8), indicating *α*-helices and *β*-sheets in its secondary structure [21]. The estimated 39% *α*-helical content for hPAH (see Table 5.4) is in good agreement with previous reports [38]. Upon FIL addition, hPAH maintains its characteristic spectra with small variations in molar ellipticity, indicating that $[N_{1112(OH)}][C_4F_9SO_3]$ does not affect the protein's secondary structure.

Figure 5.8. Far-UV CD spectra of hPAH in the absence/presence of $[N_{1112(OH)}][C_4F_9SO_3]$ from 0.3 to 2% *v/v*.

Table 5.4. Estimation of secondary structure content of hPAH at different concentrations of $[N_{1112(OH)}][C_4F_9SO_3]$.

$[N_{1112(OH)}][C_4F_9SO_3]$ (% v/v)	α-Helix	β-Sheet	*Random Coil*
0	0.39	0.09	0.52
0.3	0.4	0.14	0.46
0.6	0.38	0.08	0.54
1.2	0.4	0.11	0.49
2	0.38	0.07	0.55

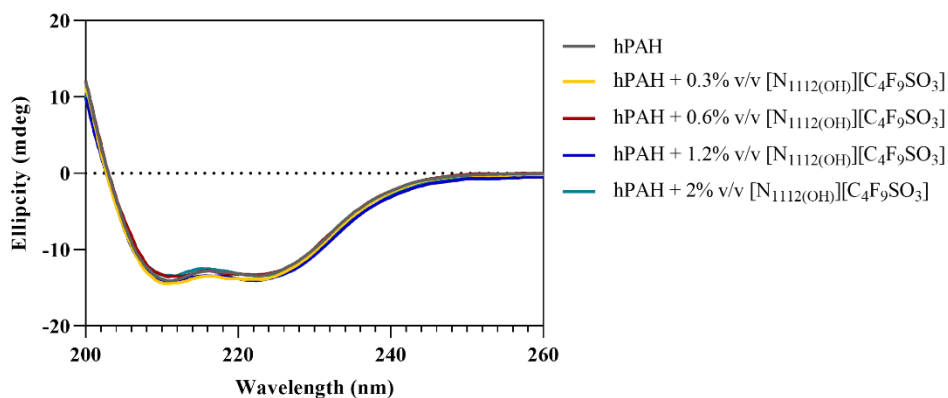Therefore, the effects observed on the hPAH activity, thermostability, and proteolytic rate are not due to protein denaturation but may result from subtle changes in the tertiary structure of the protein in the presence of FIL. To analyse the impact of $[N_{1112(OH)}][C_4F_9SO_3]$ on the quaternary structure of hPAH, blue native electrophoresis was performed (see Figure 5.9a), as it allows differentiation between the various oligomeric states of hPAH. Tetramers are the predominant form, with some octamers present to a lesser extent (even for the control assay; see Figure 5.9a, *lane 2*) as expected [36]. The addition of higher concentrations of FIL (1.2%) leads to a slight increase in monomers, resulting from the dissociation of octamers and tetramers (see Figure 5.9b). In the presence of L-Phe (c), a higher level of octamers was found. However, the octameric form of hPAH is maintained, as are the other oligomeric forms. Thus, $[N_{1112(OH)}][C_4F_9SO_3]$ (at 0.3 and 0.6% v/v) does not influence the oligomeric state of non-activated and L-Phe activated hPAH, nor does it promote the formation of aggregates with/without L-Phe.

SAXS data were collected in order to assess possible $[N_{1112(OH)}][C_4F_9SO_3]$ induced conformational changes in hPAH. The scattering curves are clearly different in the absence and presence of L-Phe, with the latter showing a broad peak at 0.12 Å^{-1} characteristic of a core–shell-like structure (Figure 5.10a). This reflects the L-Phe induced assembly of hPAH into a tetrameric and/or octameric structure. In the absence of L-Phe, this peak is absent, suggesting the sample is a polydisperse mixture of different assembly states (e.g., octamers, tetramers, and monomers). In the presence of FIL, the shift between hPAH's resting (absence of L-Phe) and active state characteristic of domain assembly/rearrangement is maintained, confirming that $[N_{1112(OH)}][C_4F_9SO_3]$ does not interfere with the mechanism of hPAH allosteric activation by L-Phe [22,28].
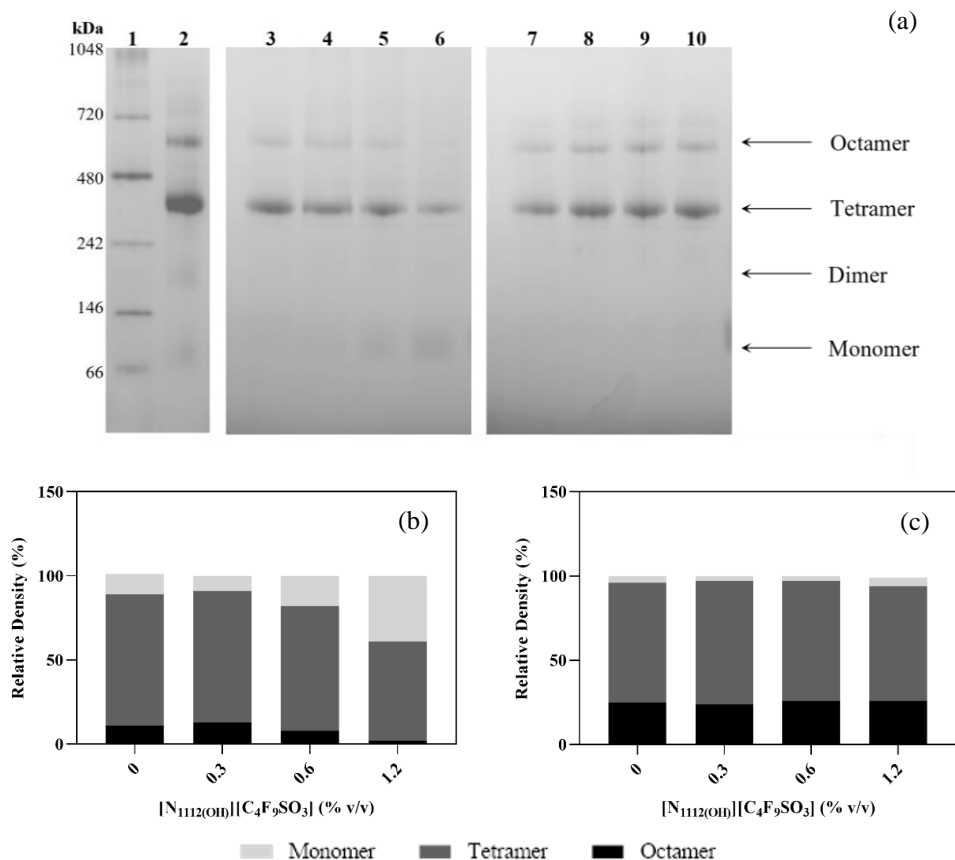
Figure 5.9. Oligomerization states of hPAH. (**a**) Blue native electrophoresis. Gel 1 (reference): Lane 1–NativeMark; Lane 2—hPAH; Gel 2 (no L-Phe): Lane 3—hPAH, Lane 4—hPAH + 0.3% FIL; Lane 5—hPAH + 0.6% FIL; Lane 6—hPAH + 1.2% FIL; Gel 3 (L-Phe): Lane 7—hPAH + L-Phe, Lane 8—hPAH + L-Phe + 0.3% FIL; Lane 9—hPAH + L-Phe + 0.6% FIL; Lane 10—hPAH + L-Phe + 1.2% FIL. Relative quantification of (**b**) hPAH + FIL and of (**c**) hPAH + L-Phe + FIL calculated using ImageJ software, considering, respectively, Lanes 3 and 7 as controls.

In the absence of L-Phe, evidence of non-specific aggregate formation is observed at low angles, which increases with higher concentrations of FIL. In the presence of L-Phe, however, this behaviour is only observed at FIL concentrations above 0.6% *v/v*. Furthermore, an oligomerization analysis (see Figure 5.10b) of the scattering data, using the high-resolution domain structures of hPAH (PDB ID: 5FII, 2PAH) to define association/dissociation components, also suggests the presence of larger species, even before the addition of FIL. This effect has been reported in previous SAXS data collection of hPAH, where the protein tends to equilibrate between different oligomeric states [28,36]. SEC coupled to SAXS (SEC-SAXS) can usually overcome this; however, the interaction between ionic liquids and column matrices precluded the use of the SEC-SAXS mode in this case [39]. The oligomeric equilibrium analysis suggests that the SAXS data in the absence
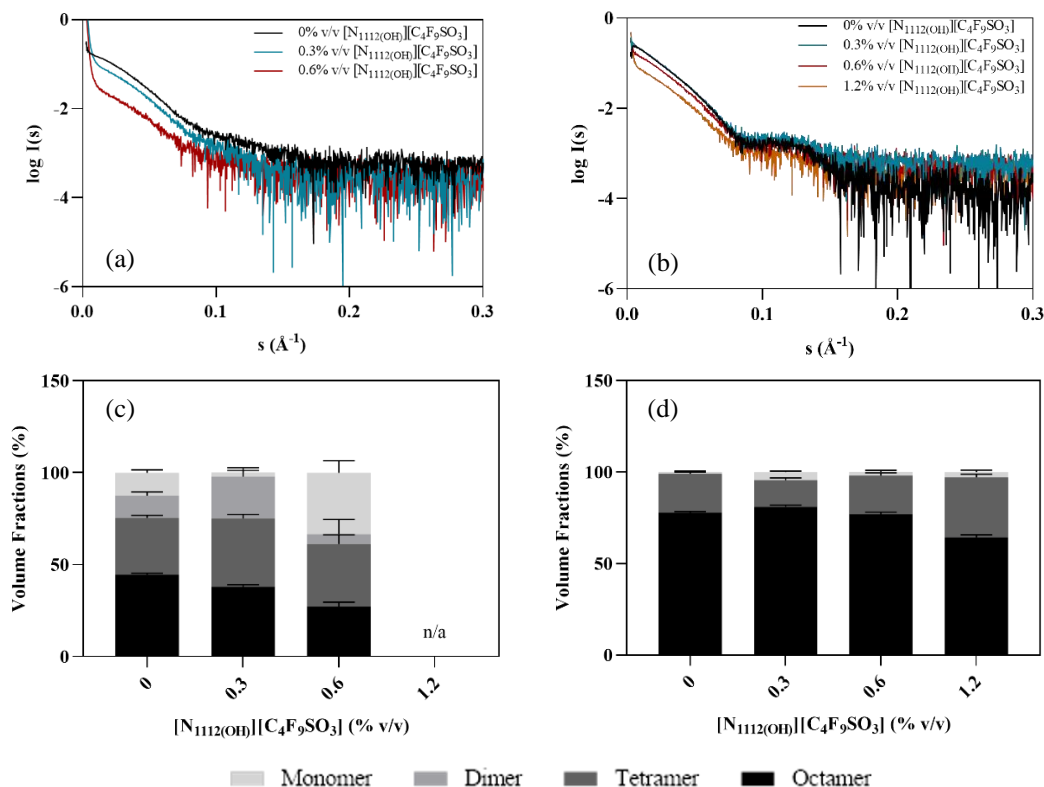
Figure 5.10. Effect of [N$_{1112(OH)}$][C$_4$F$_9$SO$_3$] on the SAXS profile of hPAH. (**a**) Experimental scattering curves of hPAH + FIL; (**b**) experimental scattering curves of hPAH + L-Phe + FIL; (**c**) volume fractions of oligomers in hPAH + FIL samples; (**d**) volume fractions of oligomers in hPAH + L-Phe + FIL samples.

of L-Phe are best fit by a mixture of octameric, tetrameric, dimeric, and monomeric hPAH (Figure 5.10c,d). The concentration of dimeric hPAH is maintained, while the volume fraction of octameric hPAH decreases with increasing concentrations of [N$_{1112(OH)}$][C$_4$F$_9$SO$_3$] accompanied by an increase in the monomer. For hPAH incubated with L-Phe, the octameric species is dominant, and the dimer is not selected. Interestingly, the ratio of oligomeric species is maintained across the FIL concentration series. These results are in agreement with the blue native electrophoresis described above, confirming that the addition of FIL at the tested concentrations does not influence the oligomerization of hPAH + L-Phe, while for the non-activated protein, a different oligomeric profile was only observed with 0.6% [N$_{1112(OH)}$][C$_4$F$_9$SO$_3$]. Structural parameters such as radius of gyration (R_g), Porod volume (V_P), and approximated average molecular mass (MM), described in Table 5.5, are in agreement with published hPAH batch (i.e., non-SEC) measurements describing a mixture of oligomeric states [28]. These parameters tend to decrease with increasing FIL

concentrations, indicating higher protein compactness on average or the dissociation of larger assemblies into tetrameric/dimeric and monomeric forms. For non-activated hPAH + 0.6% *v/v* FIL, for instance, the calculated MM is 77 kDa, which corresponds to the expected MM of monomeric hPAH [40], the most prevalent species in the sample (Figure 5.10c). Taking into consideration that octamers were the most prevalent forms for the preactivated hPAH in the presence of IL (Figure 5.10d) and that a decrease in all structural parameters was observed, the data seem to indicate higher protein compactness for those species as the $[N_{1112(OH)}][C_4F_9SO_3]$ concentration increases.

Table 5.5. SAXS structural parameters of hPAH in the presence and absence of $[N_{1112(OH)}][C_4F_9SO_3]$ and L-Phe.

$[N_{1112(OH)}][C_4F_9SO_3]$ (% *v/v*)	No L-Phe				1 mM L-Phe			
	R_g (Å)	V_P (Å^3)	D_{max} (Å)	MM (kDa)	R_g (Å)	V_P (Å^3)	D_{max} (Å)	MM (kDa)
0	53.4 ± 1.1	459,446	168	287	61.7 ± 5.3	741,198	187	463
0.3	50.4 ± 1.2	354,904	137	221	56.7 ± 2.9	617,827	164	386
0.6	46.3 ± 1.8	122,885	117	77	58.7 ± 3.6	556,597	158	348
1.2	-	-	-	-	58.9 ± 4.3	476,911	143	298

Radii of gyration (R_g) were estimated from the Guinier approximation. Excluded particle volumes (V_P) were estimated from the Porod approximation. Maximum particle dimensions (D_{max}) were obtained from the pair-distribution function. Molecular mass (MM) values were derived from the Porod volume as MM = VP/1.6.

4.2 hPAH Encapsulation by FIL

In order to assess encapsulation of hPAH by $[N_{1112(OH)}][C_4F_9SO_3]$, both DLS and TEM were used to characterize and visualize micelles in solution. The DLS spectra showed a characteristic peak of hPAH at ~14 nm (see Figure 5.11a) [41], while the spectrum of 1.2% *v/v* $[N_{1112(OH)}][C_4F_9SO_3]$ (without hPAH) did not exhibit any aggregates in this range (see Figure 5.11b), with a bimodal distribution at higher diameter ranges (around 60 and 300 nm). The addition of 0.3% *v/v* FIL led to a decrease in the intensity of the protein peak, although it remains in the solution. At FIL concentrations above *CAC* (0.6–1.8% *v/v*), the protein peak completely disappears, and a single peak appears due to the strong interaction/association of FIL with hPAH, suggesting protein encapsulation. For example, hPAH + 1.2% $[N_{1112(OH)}][C_4F_9SO_3]$ exhibits only one broad peak with a mean size of ~600 nm (see Figure 5.11b). These results show a shift towards higher hydrodynamic diameters for

$[N_{1112(OH)}][C_4F_9SO_3]$ concentrations > 0.6% *v/v*, suggesting encapsulation of hPAH for FIL concentrations above *CAC*. Similar behaviour has already been reported for lysozyme.[18]
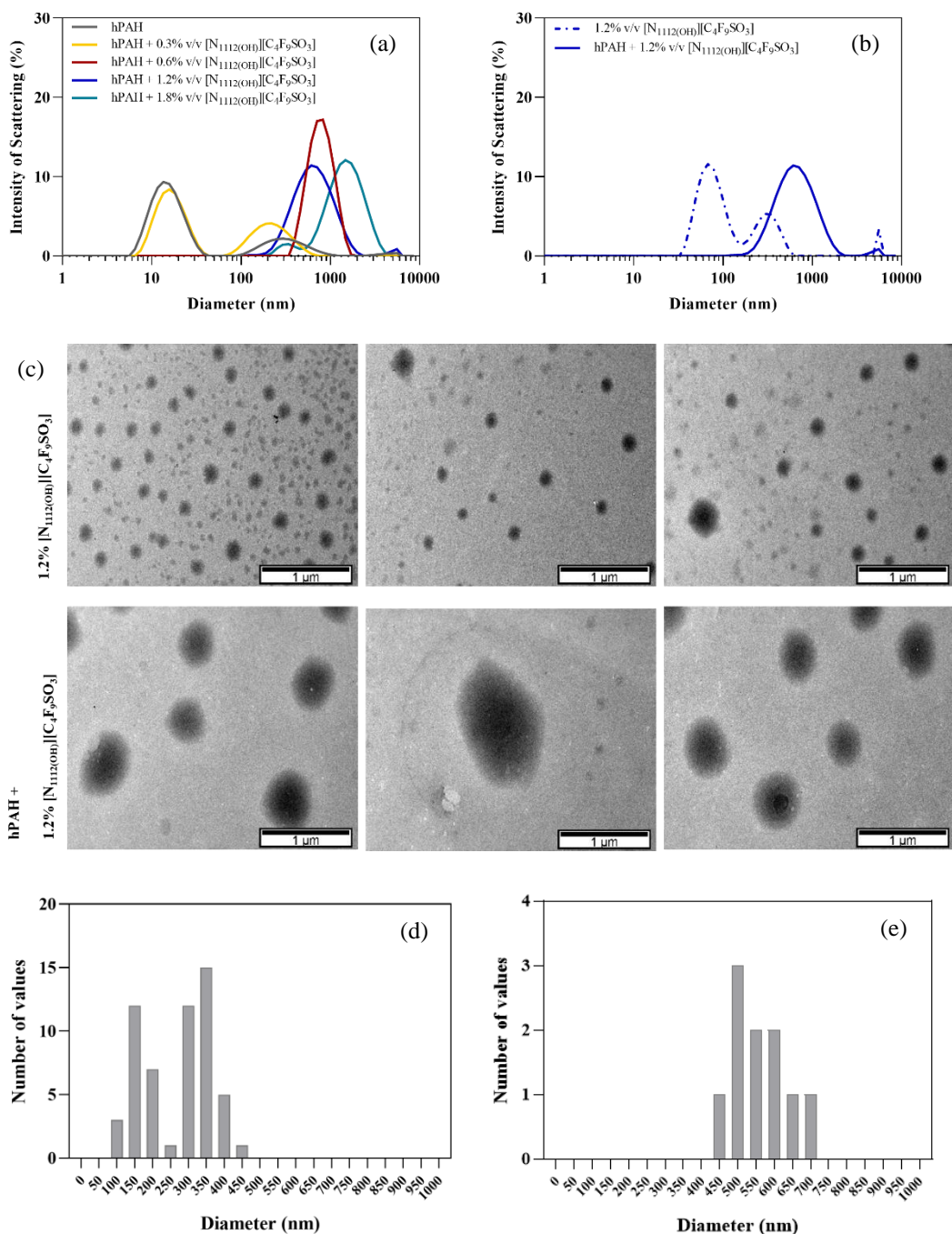
Figure 5.11. Encapsulation of hPAH by $[N_{1112(OH)}][C_4F_9SO_3]$. DLS spectra of hPAH upon: (**a**) the addition of increasing concentrations of FIL; and (**b**) comparison between 1.2% *v/v* FIL Blank with hPAH + 1.2% *v/v* FIL. (**c**) TEM analysis of 1.2% *v/v* FIL (top) and hPAH + 1.2% *v/v* FIL (bottom). Size distribution (Feret diameter) of particles present in TEM images: (**d**) 1.2% *v/v* FIL and (**e**) hPAH + 1.2% FIL *v/v*, quantified using ImageJ software.

TEM images were collected in the presence of 1.2% *v/v* [N$_{1112(OH)}$][C$_4$F$_9$SO$_3$], which corresponds to 2x *CAC*, to maximize the probability of protein encapsulation (see Figure 5.11c). Control samples (FIL, no hPAH) revealed the formation of heterogeneous micelles, which also displayed a bimodal distribution of particle sizes of approximately 150 and 350 nm (see Figure 5.11d). This behavior and size distribution was previously observed for similar FILs [18]. In the presence of hPAH, there was a clear increase in particle size to 500–600 nm (see Figure 5.11e). The sizes measured using the TEM micrographs are in accordance with the diameters obtained by DLS. Therefore, we conclude that, in the presence of hPAH, FIL aggregates become larger and more homogenous due to protein encapsulation. This encapsulation evidence observed by DLS and TEM is corroborated by SAXS. This experimental technique shows some evidence of those aggregates (e.g., upturns in the data at low angles). However, the D_{max} of those large aggregates cannot be extracted because bigger particles provide scattering intensities that are mostly intercepted by the beamstop. Furthermore, hPAH alone shows a DLS peak that matches with the SAXS (D_{max} ~17 nm), confirming the DLS data.

5. Conclusions

This study showed that the addition of [N$_{1112(OH)}$][C$_4$F$_9$SO$_3$] at 0.6–1.2% *v/v* to hPAH increased the enzymatic activity in the absence or presence of L-Phe, despite decreasing protein thermostability (nanoDSF). The presence of FIL seems to confer hPAH some protection against trypsin digestion, so we postulate that [N$_{1112(OH)}$][C$_4$F$_9$SO$_3$] may induce structural rearrangements on the N-terminal regulatory domain of hPAH, resulting in a more exposed catalytic domain, with higher basal activity (absence of L-Phe) but lower T_m. Moreover, [N$_{1112(OH)}$][C$_4$F$_9$SO$_3$] does not affect hPAH's secondary structure (CD) nor its oligomerization states when the protein is pre-incubated with L-Phe; however, in the absence of L-Phe and at 1.2%, it favours the dissociation of octamers/tetramers into monomers (BN-PAGE). [N$_{1112(OH)}$][C$_4$F$_9$SO$_3$] does not contribute to the aggregation of hPAH (BN-PAGE and SAXS). These are promising results as aggregates may lead to loss of function and immunogenic reactions, so this phenomenon should be prevented during protein formulation. In addition, incubation of hPAH with [N$_{1112(OH)}$][C$_4$F$_9$SO$_3$] at concentrations ≥ 0.6% leads to the formation of larger molecular mass species ~1 μm (DLS), and the addition of hPAH to FIL self-assembled particles at 1.2% *v/v* also increases their sizes to similar values (TEM), thus suggesting protein encapsulation. Indeed, [N$_{1112(OH)}$][C$_4$F$_9$SO$_3$] has high surface activity and has been previously shown to be able to form micelles and encapsulate lysozyme.[15,18] The results herein presented show that this FIL is still able to encapsulate a larger and more complex protein while still retaining its structure and function. Although [N$_{1112(OH)}$][C$_4$F$_9$SO$_3$] has been found to be non-toxic in four human cell lines[16] and its eco-toxicity has also been assessed,[17] studies on subjects such as the immunogenicity and delivery of this potential drug delivery system are needed to better understand hPAH-[N$_{1112(OH)}$][C$_4$F$_9$SO$_3$] interactions.

6. References

1. Adawiyah, N.; Moniruzzaman, M.; Hawatulaila, S.; Goto, M. Ionic liquids as a potential tool for drug delivery systems. *Medchemcomm* **2016**, *7*, 1881–1897, doi:10.1039/c6md00358c.

2. Pedro, S.N.; Freire, C.S.R.; Silvestre, A.J.D.; Freire, M.G. The role of ionic liquids in the pharmaceutical field: An overview of relevant applications. *Int. J. Mol. Sci.* **2020**, *21*, 1–50, doi:10.3390/ijms21218298.

3. Santos de Almeida, T.; Júlio, A.; Saraiva, N.; Fernandes, A.S.; Araújo, M.E.M.; Baby, A.R.; Rosado, C.; Mota, J.P. Choline- versus imidazole-based ionic liquids as functional ingredients in topical delivery systems: cytotoxicity, solubility, and skin permeation studies. *Drug Dev. Ind. Pharm.* **2017**, *43*, 1858–1865, doi:10.1080/03639045.2017.1349788.

4. Amaral, M.; Pereiro, A.B.; Gaspar, M.M.; Reis, C.P. Recent advances in ionic liquids and nanotechnology for drug delivery. *Nanomedicine* **2020**, *16*, 63–80, doi:10.2217/nnm-2020-0340.

5. Reslan, M.; Kayser, V. Ionic liquids as biocompatible stabilizers of proteins. *Biophys. Rev.* **2018**, *10*, 781–793, doi:10.1007/s12551-018-0407-6.

6. Egorova, K.S.; Gordeev, E.G.; Ananikov, V.P. Biological Activity of Ionic Liquids and Their Application in Pharmaceutics and Medicine. *Chem. Rev.* 2017, *117*, 7132–7189.

7. Bui-Le, L.; Clarke, C.J.; Bröhl, A.; Brogan, A.P.S.; Arpino, J.A.J.; Polizzi, K.M.; Hallett, J.P. Revealing the complexity of ionic liquid–protein interactions through a multi-technique investigation. *Commun. Chem.* **2020**, *3*, 1–9, doi:10.1038/s42004-020-0302-5.

8. Pal, A.; Yadav, A. Binding interactions of anesthetic drug with surface active ionic liquid. *J. Mol. Liq.* **2016**, *222*, 471–479, doi:10.1016/J.MOLLIQ.2016.07.076.

9. Zhou, L.; Tian, T.; Xiao, J.; Wang, T.; Yu, L. Aggregation behavior of pyrrolidinium-based surface active ionic liquids in H2O-EAN binary solvents. *J. Mol. Liq.* **2017**, *225*, 50–55, doi:10.1016/J.MOLLIQ.2016.10.142.

10. Ali, M.K.; Moshikur, R.M.; Wakabayashi, R.; Tahara, Y.; Moniruzzaman, M.; Kamiya, N.; Goto, M. Synthesis and characterization of choline–fatty-acid-based ionic liquids: A new biocompatible surfactant. *J. Colloid Interface Sci.* **2019**, *551*, 72–80, doi:10.1016/j.jcis.2019.04.095.

11. Harada, L.; Pereira, J.; Campos, W.; Silva, E.; Moutinho, C.; Vila, M.; Oliveira Jr., J.; Teixeira, J.; Balcão, V.; Tubino, M.; et al. Insights into Protein-Ionic Liquid Interactions Aiming at Macromolecule Delivery Systems. *J. Braz. Chem. Soc.* **2018**, *29*, 1983–1998, doi:10.21577/0103-5053.20180141.

12. Singh, O.; Singla, P.; Aswal, V.K.; Mahajan, R.K. Aggregation and Morphological Aptitude of Drug-Based Ionic Liquids in Aqueous Solution. *ACS Omega* **2017**, *2*, 3296–3307, doi:10.1021/acsomega.7b00578.

13. Singla, P.; Singh, O.; Chabba, S.; Mahajan, R.K. Pluronic-SAILs (surface active

ionic liquids) mixed micelles as efficient hydrophobic quercetin drug carriers. *J. Mol. Liq.* **2018**, *249*, 294–303, doi:10.1016/j.molliq.2017.11.044.

14. Bharmoria, P.; Kumar, A. Thermodynamic investigations of protein's behaviour with ionic liquids in aqueous medium studied by isothermal titration calorimetry. *Biochim. Biophys. Acta - Gen. Subj.* **2016**, *1860*, 1017–1025, doi:10.1016/J.BBAGEN.2015.08.022.

15. Pereiro, A.B.; Araújo, J.M.M.; Teixeira, F.S.; Marrucho, I.M.; Piñeiro, M.M.; Rebelo, L.P.N. Aggregation behavior and total miscibility of fluorinated ionic liquids in water. *Langmuir* **2015**, *31*, 1283–1295, doi:10.1021/la503961h.

16. Vieira, N.S.M.; Bastos, J.C.; Rebelo, L.P.N.; Matias, A.; Araújo, J.M.M.; Pereiro, A.B. Human cytotoxicity and octanol/water partition coefficients of fluorinated ionic liquids. *Chemosphere* **2019**, *216*, 576–586, doi:10.1016/j.chemosphere.2018.10.159.

17. Vieira, N.S.M.; Stolte, S.; Araújo, J.M.M.; Rebelo, L.P.N.; Pereiro, A.B.; Markiewicz, M. Acute Aquatic Toxicity and Biodegradability of Fluorinated Ionic Liquids. *ACS Sustain. Chem. Eng.* **2019**, *7*, 3733–3741, doi:10.1021/acssuschemeng.8b03653.

18. Alves, M.; Vieira, N.S.M.; Rebelo, L.P.N.; Araújo, J.M.M.; Pereiro, A.B.; Archer, M. Fluorinated ionic liquids for protein drug delivery systems: Investigating their impact on the structure and function of lysozyme. *Int. J. Pharm.* **2017**, *526*, 309–320, doi:10.1016/j.ijpharm.2017.05.002.

19. Alves, M.M.S.; Araújo, J.M.M.; Martins, I.C.; Pereiro, A.B.; Archer, M. Insights into the interaction of Bovine Serum Albumin with Surface-Active Ionic Liquids in aqueous solution. *J. Mol. Liq.* **2021**, *322*, 114537, doi:10.1016/j.molliq.2020.114537.

20. Pey, A.L.; Thórólfsson, M.; Teigen, K.; Ugarte, M.; Martínez, A. Thermodynamic characterization of the binding of tetrahydropterins to phenylalanine hydroxylase. *J. Am. Chem. Soc.* **2004**, *126*, 13670–13678, doi:10.1021/ja047713s.

21. Cerreto, M.; Cavaliere, P.; Carluccio, C.; Amato, F.; Zagari, A.; Daniele, A.; Salvatore, F. Natural phenylalanine hydroxylase variants that confer a mild phenotype affect the enzyme's conformational stability and oligomerization equilibrium. *Biochim. Biophys. Acta - Mol. Basis Dis.* **2011**, *1812*, 1435–1445, doi:10.1016/j.bbadis.2011.07.012.

22. Tomé, C.S.; Lopes, R.R.; Sousa, P.M.F.; Amaro, M.P.; Leandro, J.; Mertens, H.D.T.; Leandro, P.; Vicente, J.B. Structure of full-length wild-type human phenylalanine hydroxylase by small angle X-ray scattering reveals substrate-induced conformational stability. *Sci. Rep.* **2019**, *9*, 1–14, doi:10.1038/s41598-019-49944-x.

23. van Spronsen, F.J.; Blau, N.; Harding, C.; Burlina, A.; Longo, N.; Bosch, A.M. Phenylketonuria. *Nat. Rev. Dis. Prim.* **2021**, *7*, 1–19, doi:10.1038/s41572-021-00267-0.

24. Borges, A.C.; Broersen, K.; Leandro, P.; Fernandes, T.G. Engineering Organoids for in vitro Modeling of Phenylketonuria. **2022**, *14*, doi:10.3389/fnmol.2021.787242.

25. Flydal, M.I.; Martinez, A. Critical Review Phenylalanine Hydroxylase: Function, Structure, and Regulation. *IUBMB Life* **2013**, *65*, 341–349, doi:10.1002/iub.1150.

26. Leandro, P.; Rivera, I.; Lechner, M.C.; De Almeida, I.T.; Konecki, D. The V388M Mutation Results in a Kinetic Variant Form of Phenylalanine Hydroxylase. *Mol. Genet. Metab.* **2000**, *69*, 204–212, doi:10.1006/MGME.2000.2970.

27. Montalbano, F.; Leandro, J.; Farias, G.D.V.F.G.D.V.F.; Lino, P.R.; Guedes, R.C.; Vicente, J.B.; Leandro, P.; Gois, P.M.P.P. Phenylalanine iminoboronates as new phenylalanine hydroxylase modulators. *RSC Adv.* **2014**, *4*, 61022–61027, doi:10.1039/c4ra10306h.

28. Lopes, R.R.; Tomé, C.S.; Russo, R.; Paterna, R.; Leandro, J.; Candeias, N.R.; Gonçalves, L.M.D.; Teixeira, M.; Sousa, P.M.F.; Guedes, R.C.; et al. Modulation of human phenylalanine hydroxylase by 3-hydroxyquinolin-2(1h)-one derivatives. *Biomolecules* **2021**, *11*, 1–25, doi:10.3390/biom11030462.

29. Schneider, C.A.; Rasband, W.S.; Eliceiri, K.W. NIH Image to ImageJ: 25 years of image analysis. *Nat. Methods* **2012**, *9*, 671–675, doi:10.1038/nmeth.2089.

30. Andrade, M.A.A.; Chacón, P.; Merelo, J.J.J.; Morán, F. Evaluation of secondary structure of proteins from UV circular dichroism spectra using an unsupervised learning neural network. *Protein Eng. Des. Sel.* **1993**, *6*, 383–390, doi:10.1093/protein/6.4.383.

31. Whitmore, L.; Wallace, B.A. DICHROWEB, an online server for protein secondary structure analyses from circular dichroism spectroscopic data. *Nucleic Acids Res.* **2004**, *32*, W668–W673, doi:10.1093/nar/gkh371.

32. Whitmore, L.; Wallace, B.A. Protein secondary structure analyses from circular dichroism spectroscopy: Methods and reference databases. *Biopolymers* **2008**, *89*, 392–400, doi:10.1002/bip.20853.

33. Blanchet, C.E.; Spilotros, A.; Schwemmer, F.; Graewert, M.A.; Kikhney, A.; Jeffries, C.M.; Franke, D.; Mark, D.; Zengerle, R.; Cipriani, F.; et al. Versatile sample environments and automation for biological solution X-ray scattering experiments at the P12 beamline (PETRA III, DESY). *J. Appl. Crystallogr.* **2015**, *48*, 431–443, doi:10.1107/S160057671500254X.

34. Franke, D.; Petoukhov, M. V; Konarev, P. V; Panjkovich, A.; Tuukkanen, A.; Mertens, H.D.T.; Kikhney, A.G.; Hajizadeh, N.R.; Franklin, J.M.; Jeffries, C.M.; et al. ATSAS 2.8: a comprehensive data analysis suite for small-angle scattering from macromolecular solutions. *J. Appl. Crystallogr.* **2017**, *50*, 1212–1225, doi:10.1107/S1600576717007786.

35. Konarev, P. V; Volkov, V. V; Sokolova, A. V; Koch, M.H.J.; Svergun, D.I. PRIMUS: a Windows PC-based system for small-angle scattering data analysis. *J. Appl. Crystallogr.* **2003**, *36*, 1277–1282, doi:10.1107/S0021889803012779.

36. Arturo, E.C.; Gupta, K.; Hansen, M.R.; Borne, E.; Jaffe, E.K. Biophysical characterization of full-length human phenylalanine hydroxylase provides a deeper understanding of its quaternary structure equilibrium. *J. Biol. Chem.* **2019**, *294*, 10131–10145, doi:10.1074/jbc.RA119.008294.

37. Jaffe, E.K.; Stith, L.; Lawrence, S.H.; Andrake, M.; Dunbrack, R.L. A new model for allosteric regulation of phenylalanine hydroxylase: Implications for disease and therapeutics. *Arch. Biochem. Biophys.* **2013**, *530*, 73–82, doi:10.1016/j.abb.2012.12.017.

38. Miranda, F.F.; Teigen, K.; Thórólfsson, M.; Svebak, R.M.; Knappskog, P.M.; Flatmark, T.; Martínez, A. Phosphorylation and mutations of Ser16 in human phenylalanine hydroxylase: Kinetic and structural effects. *J. Biol. Chem.* **2002**, *277*, 40937–40943, doi:10.1074/jbc.M112197200.

39. Huang, Y.; Yao, S.; Song, H. Application of ionic liquids in liquid chromatography and electrodriven separation. *J. Chromatogr. Sci.* **2013**, *51*, 739–752, doi:10.1093/chromsci/bmt076.

40. Flydal, M.I.; Alcorlo-Pagés, M.; Johannessen, F.G.; Martínez-Caballero, S.; Skjærven, L.; Fernandez-Leiro, R.; Martinez, A.; Hermoso, J.A. Structure of full-length human phenylalanine hydroxylase in complex with tetrahydrobiopterin. *Proc. Natl. Acad. Sci. U. S. A.* **2019**, *166*, 11229–11234, doi:10.1073/pnas.1902639116.

41. Gersting, S.W.; Lagler, F.B.; Eichinger, A.; Kemter, K.F.; Danecka, M.K.; Messing, D.D.; Staudigl, M.; Domdey, K.A.; Zsifkovits, C.; Fingerhut, R.; et al. Pahenu1 is a mouse model for tetrahydrobiopterin-responsive phenylalanine hydroxylase deficiency and promotes analysis of the pharmacological chaperone mechanism in vivo. *Hum. Mol. Genet.* **2010**, *19*, 2039–2049, doi:10.1093/hmg/ddq085.

CHAPTER VI
General Discussion and Future Perspectives

1. General Discussion

In recent years, ionic liquids have garnered a lot of attention due to their physicochemical properties (hydrophobicity, hydrogen bonding ability, ion tunability) which make them suitable solvents for macromolecules [1]. This class of chemicals has been described as enhancers of protein and enzyme stabilization, that also demonstrate potential for increasing enzyme catalytic activity [1,2]. However, since both ILs and proteins are structurally diverse, their association can lead to a wide range of possible interactions, which depend on factors such as the protein itself, the concentration and structure of the IL, including the length and hydrophobicity of its alkyl side chain [2,3]. Although these protein-IL systems show great promise for the development of new biologics, their diversity and complexity mean that each complex must be studied using a thorough and multi-faceted approach.

In this work, the stability, activity, and structure of different proteins were assessed in the presence of different concentrations of surface-active FILs, in order to establish the foundation work for the development of drug delivery systems for therapeutic proteins.

Initially, as described in Chapter II, a battery of six FILs based on the perfluorobutanesulfonate ($[C_4F_9SO_3]^-$) and perfluorobutanepentanoate ($[C_4F_9CO_2]^-$) anions, as well as two non-surfactant ILs, were tested against model protein lysozyme. Lys was chosen as the first model protein for this study since it has already been well characterized, is widely available and there were already some reports on its interaction with conventional ILs [4–6]. All experiments were performed under the same conditions as far as possible, with fixed protein and IL concentrations. FILs were tested above and below their described *CAC*s [7]. The thermostability assay showed that Lys T_m decreased a maximum of 2% (8 K) in the presence of 1.2% *v/v* $[C_2C_1py][C_4F_9CO_2]$, which was deemed not significant. The activity assay, which follows the hydrolysis of *M. lysodeikticus* cell wall by Lys, revealed that the addition of the surfactant ILs resulted in a slight increase in enzymatic activity. Surprisingly, $[C_2C_1Im][C_4F_9SO_3]$ led to an increase of 20% in the hydrolytic rate of Lys. The analysis of protein secondary structure by CD detected no substantial alteration in the predicted values, although only $[N_{1112(OH)}]^+$ based FILs were able to be tested using this technique. The analysis of protein encapsulation was performed using two approaches, DLS and microscopy, which confirmed that Lys was encapsulated by FILs at concentrations between 1 and 1.2% *v/v*. The work performed in this chapter allowed us to conclude that

despite protein encapsulation by the surfactant FILs, neither the stability nor activity of Lys were affected, providing us with a solid starting point for the remaining work. Furthermore, the results obtained allowed us to narrow down the most promising FILs to the $[C_4F_9SO_3]^-$ family, which overall demonstrated the most desirable effects on the protein.

Once the positive effects of FILs on Lys had been established, we applied the same experimental design to a different model protein. In Chapter III, the interaction between BSA and FILs was analysed. In contrast to Lys, BSA has larger molecular mass and higher complexity, which posed new challenges and made it a very interesting system to study. For instance, three different assays were performed to evaluate the thermostability of BSA in the presence of FILs, to ensure that the results were not biased due to the presence of hydrophobic pockets in the protein structure or FIL interference with the technique. Interestingly, all three methods yielded highly reproducible results, indicating that, in the presence of 1.2% *v/v* FIL, BSA was stabilized with a T_m increase of approximately 30 K. Using CD, we also observed that upon the addition of $[N_{1112(OH)}][C_4F_9SO_3]$, BSA maintained its characteristic spectra. However, its molar ellipticity was slightly increased, indicating secondary structure stabilization and a more compact state. BSA-$[C_2C_1Im][C_4F_9SO_3]$ interaction (and possible encapsulation) was further analysed by ionic conductivity and ITC. These two techniques show that FIL micellization occurs independently of the presence of protein, while $[C_2C_1Im][C_4F_9SO_3]$ interacts with BSA at low concentrations promoting encapsulation and stabilization. The results obtained from this section of the work, together with those from Chapter II, demonstrated that neither Lys nor BSA showed any denaturation upon encapsulation by FILs, although BSA was clearly more stabilized, likely due to its more flexible structure. The comparison of both sets of results also highlights the need to characterize each protein-FIL system independently.

In order to better understand the interaction between these model proteins and FILs, techniques such as SAXS, CG-MD and fluorescence microscopy were applied. On one hand, SAXS data confirmed that BSA particles became more compact, on average by 19%, with increasing FIL concentrations, and that this compaction was not related to protein oligomerization state. On the other hand, Lys particles became larger, and all structural parameters had increased approximately 24% by 1.8% *v/v* FILs. Despite these opposite behaviours, both proteins maintained their globular structures, although some flexibility may have been introduced by the FILs. CG-MD simulations for Lys-$[N_{1112(OH)}][C_4F_9SO_3]$ showed that $[C_4F_9SO_3]^-$ micelles assemble at the surface of the protein, interacting with cationic and

apolar residues and occupying the binding cleft. When two Lys molecules were present along with FIL in the simulations, FIL micelles were always at the interface that mediated their dimerization. This behaviour suggests that since protein aggregation is apparently mediated by FIL micelles and considering that the FILs tend to interact with preferential residues, protein-FIL aggregate size will be limited by the number of proteins with available surface to form networks with the FIL (and consequently other proteins). Unfortunately, we were unable to confirm this hypothesis using BSA, since CG-MD was only used to simulate Lys as systems containing BSA consistently tended towards protein denaturation despite the elastic network restrictions applied. However, fluorescence microscopy assays also seem to point towards the possibility that micelle size is limited by the protein, as micelles containing only environmental probe NR became larger at higher FIL concentrations, in contrast to micelles containing Lys-Rho, which retained their size of 200-300 nm upon addition of $[C_2C_1Im][C_4F_9SO_3]$. These assays also corroborated previous reports of Lys encapsulation by FILs.

Finally, in Chapter V, similar methodologies were applied to hPAH, a potentially therapeutic enzyme. hPAH is responsible for the conversion of L-Phe into L-Tyr and forms a 210 kDa tetramer. Mutations in the gene coding for *PAH* can lead to phenylketonuria that has no definitive treatment yet. Enzyme reposition therapy of hPAH to PKU patients could be a universal strategy to treat this disease. However, since hPAH is a highly complex and environmentally sensitive protein, it needs to be stabilized to ensure its successful delivery. Preliminary DSF and activity assays showed $[N_{1112(OH)}][C_4F_9SO_3]$ as the most promising FIL for studies with hPAH. Although at first glance the addition of $[N_{1112(OH)}][C_4F_9SO_3]$ to hPAH revealed a detrimental effect on protein thermostability, which was more significant on the regulatory domain, this destabilization seemed to leave the catalytic domain more accessible to the substrate, leading to an increase in hPAH activity rate. Furthermore, CD shows that hPAH secondary structure is not affected by the presence of FIL. Interestingly, $[N_{1112(OH)}][C_4F_9SO_3]$ protects hPAH against limited proteolysis by trypsin (digestion rate 6*x* slower than the control), probably by inducing higher protein compactness or less conformation flexibility/mobility. These results suggest that the FIL effect on hPAH may result from subtle changes on its tertiary structure. In order to assess possible conformational changes in hPAH caused by $[N_{1112(OH)}][C_4F_9SO_3]$, SAXS was employed, confirming that the FIL does not interfere with the mechanism of hPAH allosteric activation by L-Phe. Similar to BSA, SAXS structural parameters also tended to decrease with higher FIL concentrations, indicating higher protein compactness or dissociation of larger

assemblies. Using DLS, we established that hPAH protein peak disappeared at concentrations above 0.3% *v/v* [N$_{1112(OH)}$][C$_4$F$_9$SO$_3$], and TEM revealed that in the presence of hPAH, FIL aggregates became larger and more homogeneous, both of which suggest protein encapsulation. Interestingly, fluorescence microscopy assays for Lys also indicated that the presence of protein defined and stabilized micelle size, although Lys-Rho + 1.2% *v/v* [C$_2$C$_1$Im][C$_4$F$_9$SO] particles were significantly smaller, likely due to Lys being a smaller enzyme than hPAH (14 vs 210 kDa). The work presented in this chapter demonstrates that [N$_{1112(OH)}$][C$_4$F$_9$SO$_3$] is still able to encapsulate a larger and more complex protein such as hPAH, while retaining its structure and function.

The work developed throughout this PhD work provided new insights into the impact of FILs on proteins. Starting with model proteins, we found that lysozyme was encapsulated by [C$_2$C$_1$Im][C$_4$F$_9$SO$_3$], while retaining its structure and stability and even increasing hydrolytic rate. We also postulated that Lys-FIL micelles are homogeneous in size and that this size is limited by the protein and not by the concentration of FIL in solution. Although BSA displayed opposite behaviour to Lys in many aspects, with the protein becoming more compact and significantly more stable, retaining its secondary structure upon encapsulation. These results allowed us to confidently carry out studies with a therapeutic protein. hPAH is the most complex protein studied herein, since it is a 210 kDa homotetramer, with an allosteric regulation mechanism that must be conserved in order to retain function. The addition of [N$_{1112(OH)}$][C$_4$F$_9$SO$_3$] caused some instability to hPAH, especially to the regulatory domain, but this instability actually led to an increase in the hydrolytic activity of the enzyme, and its secondary structure was conserved with no signs of protein denaturation, suggesting that the changes responsible for the loss of stability must be due to some tertiary structure rearrangements. These results, together with the fact that hPAH is likely encapsulated by [N$_{1112(OH)}$][C$_4$F$_9$SO$_3$], indicate that this would be an interesting system to study for transdermal delivery.

2. Future Perspectives

As mentioned in Section 8 of Chapter I, SAILs have recently been shown to deliver molecules transdermally through the disruption of the SC. In order to study this hypothesis for our system, a permeation study using Franz diffusion cells as reported by Pinto *et al.* [8] could be performed in the future (see Appendix I). Briefly, this assay consists of growing human epidermal keratinocyte primary cells on polycarbonate filters, allowing them to stratify until a reconstructed human epidermis (RHE) is formed. The inserts are then placed into Franz diffusion cells, where the receptor chamber is filled with medium, and the compound under testing, in this case protein + FIL, is added to the donor chamber. Aliquots are withdrawn periodically at established intervals from the receptor chamber and replaced with the same volume of fresh medium to ensure that the bottom of the insert always remains hydrated. This experiment would allow us to evaluate if the protein and FIL permeated through the RHE. The samples collected from the receptor chamber would be quantified for protein (spectrophotometrically or performing SDS-PAGE), and FIL (if present) could be detected and quantified by HPLC, using the method that was established for this purpose (see Appendix 2). Although a previous work reported the FILs studied herein as nontoxic in four human cell lines [9], $[N_{1112(OH)}][C_4F_9SO_3]$ was not studied in HaCaT (cultured human keratinocytes). Preliminary cell viability assays (see Appendix 3) where $[N_{1112(OH)}][C_4F_9SO_3]$ was studied in a concentration range from 0.7 to 100 mM revealed that this FIL impacts both cell membrane integrity and cell metabolism, especially for the HaCaT cell line, where IC_{50} was determined to be 9.6 ± 2.2 mM (< *CAC*). Therefore, it would also be important to evaluate possible damage to the RHE, through histological analysis of the tissue, and eventually even perform skin irritation tests. Depending on the results of these experiments, then the next steps into establishing a drug delivery system would consist of immunogenicity assays and eventually transdermal delivery tests in mice.

As a concluding remark, the work presented in this PhD thesis has made significant contributions to the understanding of interactions between different proteins and FILs. The methodologies and knowledge can now be applied not only to study similar systems, but also to hopefully develop novel drug delivery systems for the topical or transdermal delivery of therapeutic proteins.

3. References

1.   Curreri, A.M.; Mitragotri, S.; Tanner, E.E.L. Recent Advances in Ionic Liquids in Biomedicine. *Adv. Sci.* **2021**, *8*, 1–18, doi:10.1002/advs.202004819.

2.   Reslan, M.; Kayser, V. Ionic liquids as biocompatible stabilizers of proteins. *Biophys. Rev.* **2018**, *10*, 781–793, doi:10.1007/s12551-018-0407-6.

3.   Bui-Le, L.; Clarke, C.J.; Bröhl, A.; Brogan, A.P.S.; Arpino, J.A.J.; Polizzi, K.M.; Hallett, J.P. Revealing the complexity of ionic liquid–protein interactions through a multi-technique investigation. *Commun. Chem.* **2020**, *3*, 1–9, doi:10.1038/s42004-020-0302-5.

4.   Du, K.; Sun, J.; Song, X.; Chen, H.; Feng, W.; Ji, P. Investigation of Ionic LIquid [bmin][CF3SO3] with Lysozyme. *ACS Sustain. Chem. Eng.* **2014**, *2*, 1420–1428.

5.   Weaver, K.D.; Vrikkis, R.M.; Van Vorst, M.P.; Trullinger, J.; Vijayaraghavan, R.; Foureau, D.M.; McKillop, I.H.; MacFarlane, D.R.; Krueger, J.K.; Elliott, G.D. Structure and function of proteins in hydrated choline dihydrogen phosphate ionic liquid. *Phys. Chem. Chem. Phys.* **2012**, *14*, 790–801, doi:10.1039/C1CP22965F.

6.   Kowacz, M.; Marchel, M.; Juknaite, L.; Esperança, J.M.S.S.; Romao, M.J.; Carvalho, A.L.; Rebelo, L.P.N. Ionic-liquid-functionalized mineral particles for protein crystallization. *Cryst. Growth Des.* **2015**, *15*, 2994–3003, doi:10.1021/acs.cgd.5b00403.

7.   Pereiro, A.B.; Araújo, J.M.M.; Teixeira, F.S.; Marrucho, I.M.; Piñeiro, M.M.; Rebelo, L.P.N. Aggregation behavior and total miscibility of fluorinated ionic liquids in water. *Langmuir* **2015**, *31*, 1283–1295, doi:10.1021/la503961h.

8.   Pinto, F.; Fonseca, L.P.; Souza, S.; Oliva, A.; de Barros, D.P.C. Topical distribution and efficiency of nanostructured lipid carriers on a 3D reconstructed human epidermis model. *J. Drug Deliv. Sci. Technol.* **2020**, *57*, 101616, doi:10.1016/j.jddst.2020.101616.

9.   Vieira, N.S.M.; Bastos, J.C.; Rebelo, L.P.N.; Matias, A.; Araújo, J.M.M.; Pereiro, A.B. Human cytotoxicity and octanol/water partition coefficients of fluorinated ionic liquids. *Chemosphere* **2019**, *216*, 576–586, doi:10.1016/j.chemosphere.2018.10.159.

APPENDICES

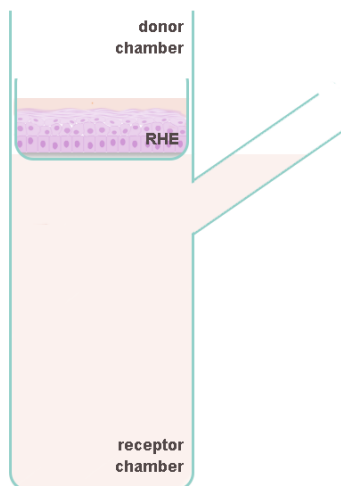**Figure S1.** Scheme representing a permeation assay using a Franz diffusion cell with reconstructed human epidermis (RHE).

Table S1. HPLC methods established for the identification and quantification of $[N_{1112(OH)}]^+$, $[C_2C_1Im]^+$ and $[C_4F_9SO_3]^-$.

	Column	Solvent A	Solvent B	Method	Flow (mL.min^{-1})	Injection Volume (µL)
$[N_{1112(OH)}]^+$	Synergi 4U Polar + pre-column	0.1% HFBA pH 6.4	MeOH	5% Solvent B	1.0	50
$[C_2C_1Im]^+$	Synergi 4U Polar + pre-column	5 mM KH_2PO_4 pH 3.5	ACN	10% Solvent B	1.0	30
$[C_4F_9SO_3]^-$	Acquity UPLC HSS C18 1.8um	5 mM $NH_4CH_3CO_2$ + 10% ACN	5 mM $NH_4CH_3CO_2$ in MeOH/ACN	70% Solvent B	0.3	5
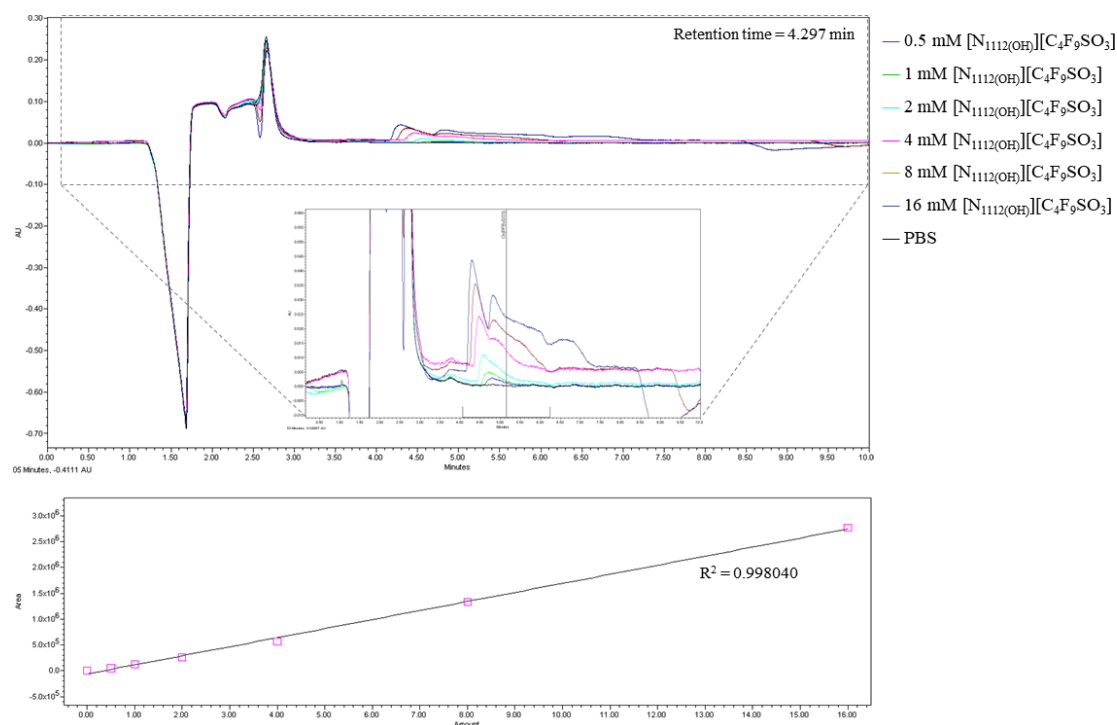
Figure S2. HPLC Chromatogram (*top*) and resulting calibration curve (*bottom*) for the identification and quantification of $[N_{1112(OH)}]^+$.
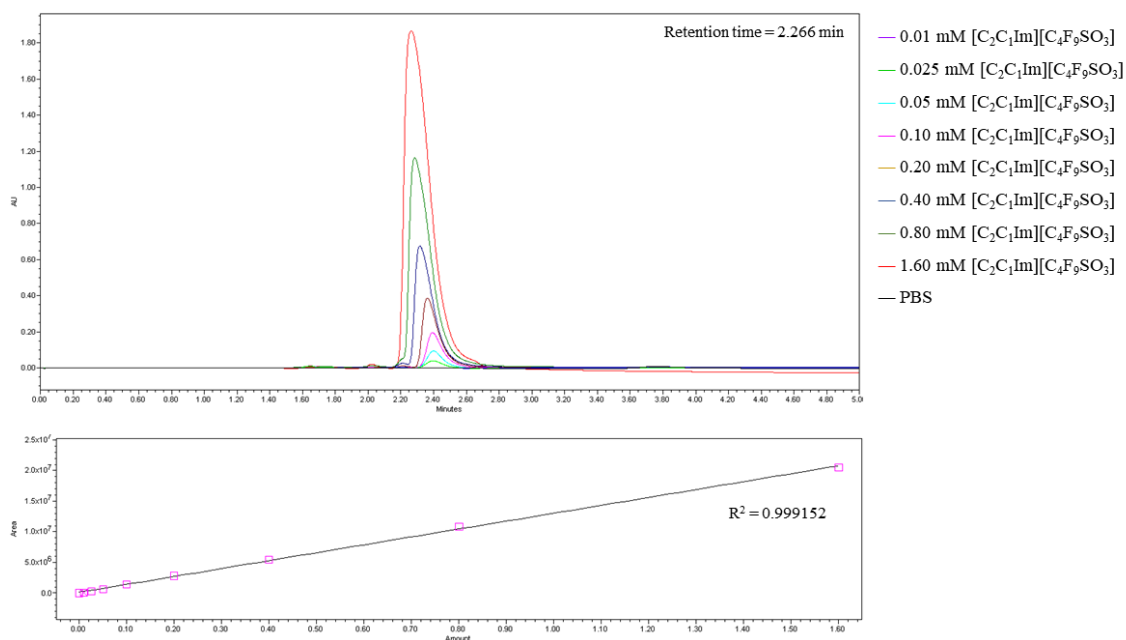
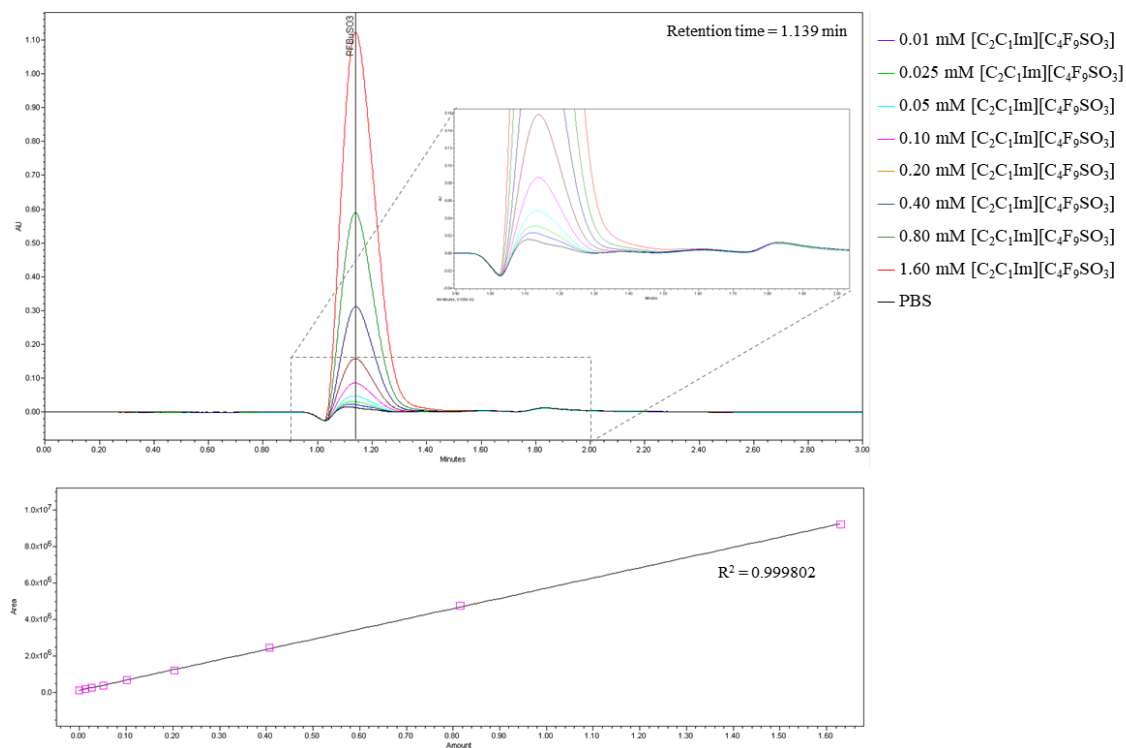**Figure S3.** HPLC Chromatogram (top) and resulting calibration curve (bottom) for the identification and quantification of $[C_2C_1Im]^+$.

Figure S4. HPLC Chromatogram (*top*) and resulting calibration curve (*bottom*) for the identification and quantification of $[C_4F_9SO_3]^-$.

Appendix III

Supplementary Method – Cell Viability Assays

FIL cytotoxicity was assessed using endpoint Alamar Blue (resazurin, 7-Hydroxy-3H-phenoxazin-3-one-10-oxide) and propidium iodide (PI) dye exclusion as metabolic and membrane integrity assays, respectively [1–4]. Briefly, three different cell lines (HEK 293T – human embryonic kidney; Hep G2 – human hepatocellular carcinoma; and HaCaT – human keratinocyte) were seeded in 96-well tissue culture plates at cell density of 2 x 10^4 cells/well, in RPMI 1640 culture medium supplemented with 10% fetal bovine serum, 100 units of penicillin G (sodium salt) and 100 μg of streptomycin sulfate and 2mM L-glutamine. The cells were exposed to $[N_{1112(OH)}][C_4F_9SO_3]$ (100 – 0.7 mM), 1 mg/mL of SDS (positive control) or culture medium (negative control), and incubated at 37 ºC and 5% CO_2 in a humidified atmosphere. After 24 h of exposition, the medium was replaced with 0.3 mM PI in culture medium, and fluorescence measurements were taken (λ_{exc} = 485 nm; λ_{em} = 590 nm). The Alamar Blue assay was then performed, replacing the medium with medium containing 5.0 mM resazurin. After 3 h of incubation, the fluorescence was measured (λ_{exc} = 530 nm; λ_{em} = 590 nm).

The relative cell viability for the resazurin assay was calculated according to the following equation:

$$Relative\ Cell\ Viability\ (\%) = \frac{Fluorescence_{sample}}{Fluorescence_{negative\ control}} \times 100$$

The PI uptake ratio was determined as follows:

$$PI\ uptake\ ratio = \frac{Fluorescence_{sample}}{Fluorescence_{negative\ control}}$$

IC50s were determined by non-linear regression using GraphPad PRISM software.
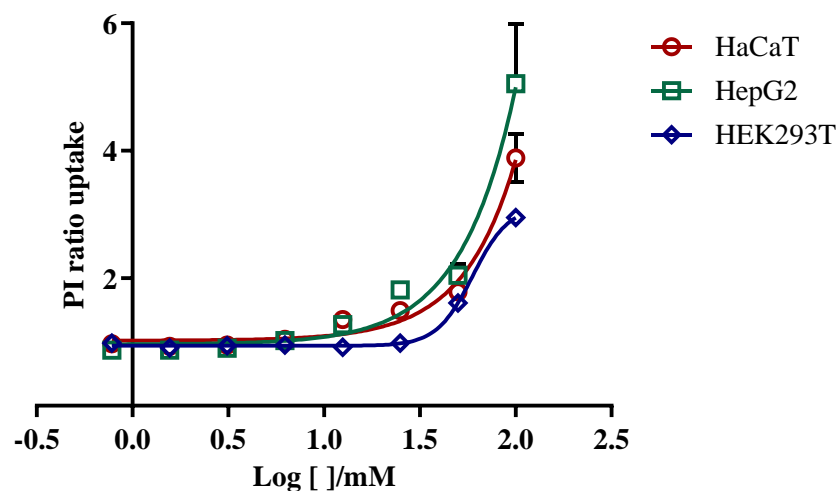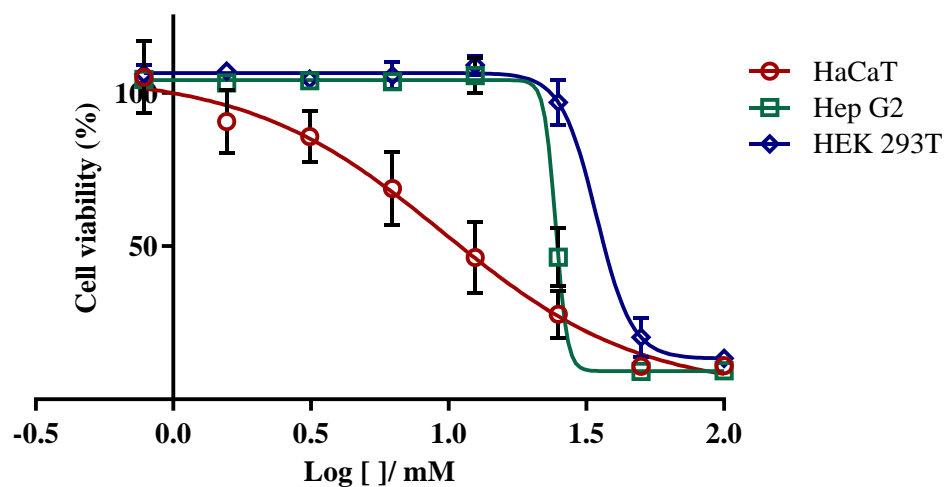
Figure S5. PI uptake for HaCaT, HepG2 and HEK 293T cell lines, after 24 h exposure to 0.7 – 100 mM $[N_{1112(OH)}][C_4F_9SO_3]$.

	HaCaT	Hep G2	HEK 293T
IC50 (mM)	9.6 ± 2.2	30.8 ± 7.3	34.4 ± 1.7

Figure S6. Relative cell viability of HaCaT, HepG2 and HEK 293T cell lines measured by resazurin reduction after 24 h exposure to 0.7 – 100 mM $[N_{1112(OH)}][C_4F_9SO_3]$ (*top*) and respective IC50 (*bottom*). (mean +- SD, n = 10)

References

1.   Ansar Ahmed, S.; Gogal, R.M.; Walsh, J.E. A new rapid and simple non-radioactive assay to monitor and determine the proliferation of lymphocytes: an alternative to [3H]thymidine incorporation assay. *J. Immunol. Methods* **1994**, *170*, 211–224, doi:https://doi.org/10.1016/0022-1759(94)90396-4.

2.   Nociari, M.M.; Shalev, A.; Benias, P.; Russo, C. A novel one-step, highly sensitive fluorometric assay to evaluate cell-mediated cytotoxicity. *J. Immunol. Methods* **1998**, *213*, 157–167, doi:https://doi.org/10.1016/S0022-1759(98)00028-3.

3.   Dengler, W.A.; Schulte, J.; Berger, D.P.; Mertelsmann, R.; Fiebig, H.H. Development of a propidium iodide fluorescence assay for proliferation and cytotoxicity assays. *Anticancer. Drugs* **1995**, *6*, 522–532, doi:10.1097/00001813-199508000-00005.

4.   Mehanna, C.; Baudouin, C.; Brignole-Baudouin, F. Spectrofluorometry assays for oxidative stress and apoptosis, with cell viability on the same microplates: A multiparametric analysis and quality control. *Toxicol. Vitr.* **2011**, *25*, 1089–1096, doi:https://doi.org/10.1016/j.tiv.2011.03.007.